Multi-Baseline Interferometric Synthetic Aperture Radar Applications and Error Analysis

by

Song Liang Chua

B. S. E., Electrical Engineering (2006)

University of Michigan, Ann Arbor

Submitted to the Department of Electrical Engineering and Computer Science
in partial fulfillment of the requirements for the degree of

Master of Science in Electrical Engineering and Computer Science

at the

MASSACHUSETTS INSTITUTE OF TECHNOLOGY

August 2007
[September 2007]

Author .....
Department of Electrical Engineering and Computer Science
August 10, 2007

Certified by .....
Jin Au Kong
Professor of Electrical Engineering
Thesis Supervisor

Certified by .....
Bae-Ian Wu
Research Scientist
Thesis Supervisor

Accepted by .....
Arthur C. Smith
Chairman, Department Committee on Graduate Students

Multi-Baseline Interferometric Synthetic Aperture Radar Applications and Error Analysis

by

Song Liang Chua

Submitted to the Department of Electrical Engineering and Computer Science
on August 10, 2007, in partial fulfillment of the
requirements for the degree of
Master of Science in Electrical Engineering and Computer Science

Abstract

In this thesis, we deal primarily with the multi-baseline SAR configuration utilizing three satellites. Two applications of InSAR, multi-baseline height retrieval and multi-baseline compensation of CCD's slope biasing effects, are first examined in details. An optimal baseline-weighted height averaging technique is introduced. Phase averaging, a novel height retrieval technique, combines the multi-baseline phase data into one, such that only one set of heights is retrieved from the three-satellite configuration. This approach outperforms single baseline height retrieval and allows application of the conventional two-satellite height retrieval process on the multi-baseline data, without need for excessive modifications. Slope biasing effects, inherent in multilook coherence estimator, make it difficult to identify if low or medium coherence values are results of an actual scene change or an undulating terrain. This ambiguity can be best resolved by accounting for the topographic phase variations via prior knowledge of the original height profile, whose precise retrieval requires a multi-baseline satellite configuration. The three-satellite setup is then related to a realistic cartwheel configuration, where the resulting errors in the height retrieval and CCD process, due to the constant cartwheel rotation, are analyzed. It is found that baseline-weighted averaging becomes a necessary step for the correct and automated retrieval of heights while change detection works equally well when considering a realistic cartwheel setup, even though its performance becomes dependent on the cartwheel's start position. Lastly, errors in satellite positions are introduced and their impacts on height retrieval and CCD are studied. In CCD, it is shown that the effects of satellite position errors is minimal since in this case, only the local terrain profile rather than the absolute terrain matters. However, in height retrieval, small errors in the positions propagate into unacceptably large misalignments. Attempts to account for these errors without prior knowledge of any ground truths are also made, making use of cost minimization functions.

Thesis Supervisor: Jin Au Kong
Title: Professor of Electrical Engineering

Thesis Supervisor: Bae-Ian Wu
Title: Research Scientist

Acknowledgments

I would sincerely like to thank the following people:

My thesis advisor, Prof. Jin Au Kong for his wisdom, tutelage, and ability to explain difficult concepts;

My thesis co-advisor, Dr. Bae-Ian Wu for his guidance, patience and insights;

University of Michigan:
Prof. Mahta Moghaddam for her inspiration in electromagnetics, Prof. Jamie Phillips for introducing me to the world of research, Prof. Anthony Grbic for his constant encouragement, Prof. Winful for introducing me to electromagnetics, and Prof. Meerkov for his many words of wisdom;

Center for Electromagnetic Theory and Applications:
Baile Zhang for his advice on almost everything, Michael Yeung for our many fruitful collaborations, and the following colleagues for discussions on all aspects of electromagnetics: Dr. Tomasz Grzegorczyk, Brandon Kemp, Dr. Hongsheng Chen, Dr. James Chen, Beijia Zhang, Kei Suwa, Zhen Li, Huang Hui, and Xiangxiang Chen;

Marilyn Pierce for her understanding and help in my pursue of a degree in MIT;

Mr. Hara for giving me the opportunity to embark on the Mitsubishi InSAR project;

Defence Science and Technology Agency for providing me with an excellent education in the United States;

Friends in Cambridge:
Grace Wang for her support, Kenneth Lee and Hsin Min for their advice regarding my future job options, and the following friends who have made a pleasant difference in my MIT experience: Shiyun, Wui Siew, Shyue Ping, Zhiyong, Henry, Shireen, Christopher, Fabian, Lu Bin, Jiamin, Kong Jie, Trina, Nai Jia, Trevor, Amy, Chiao Lun, Najib, Lynette and Kenneth;

Xingfang Su for her love, understanding, support and concern;

My parents, Tong Guan and Sharon, who have always emphasized the importance of education to me and for being my role models in life; My sister, Kellie, for her motivation and advice, and the Chuas for their encouragements.

This thesis is dedicated to my parents, sister, and Xingfang

Contents

List of Figures

List of Tables

Chapter 1

Introduction

1.1 Introduction to SAR Interferometry

Conventional synthetic aperture radar (SAR) systems provide a two-dimensional map of the radar reflectivity of an illuminated scene, with one axis along the flight track ("along-track direction") and the other defined as the range from the SAR to the target ("across-track direction"). The interpretation of such a SAR image is partly distorted since the three-dimensional world is collapsed to two dimensions [1]. SAR Interferometry (InSAR) enables the measurement of the third dimension.

Whereas conventional SAR uses a single antenna, InSAR requires two antennas separated by a baseline. Graham [2] first demonstrated InSAR by using two vertically separated antennas to simultaneously receive backscattered signals from the scene. Signals from both antennas are recorded and processed to yield two complex SAR images of the same scene. Phases measured in each image are differenced on a pixel-by-pixel basis to obtain the geometrical information about the scene [3]. With knowledge of the interferometer geometry, this phase difference can then be converted into an altitude for each of the image point. It is this addition of a third measurement to the along and cross track location of every pixel that allows a reconstruction of the three-dimensional locations of the targets.

InSAR systems can be airborne or spaceborne, and are typically employed to retrieve the three-dimensional height information, otherwise known as the Digital Elevation Model (DEM). Other applications of InSAR include measuring the radial velocity of moving scatterers, tracking subtle terrain motions, and detecting slight changes in scene content. The latter is commonly referred to as Coherent Change Detection (CCD). As well, since SAR systems provide their own illumination in the microwave frequencies regime, they can image in daylight or at night, and in nearly all weather conditions.

InSAR requires at least two antennas to form an interferometric baseline, with the wrapped phase difference data being stored in a two-dimensional map, called the

interferogram. For the rest of the thesis, we shall assume that we are dealing with a spaceborne InSAR system and that each antenna is attached to a satellite. As such, reference to an antenna is equivalent to that of a satellite. A major part of our studies considers a three-satellite setup instead of the conventional two-satellite configuration.

1.2 Problem of Interest

In this thesis, we deal primarily with the multi-baseline SAR configuration utilizing three satellites. Two applications of InSAR, multi-baseline height retrieval and multi-baseline compensation of CCD's slope biasing effects, are first examined in details. The three-satellite setup is then related to a realistic cartwheel configuration, where the resultant errors introduced to the height retrieval and CCD process, due to the constant cartwheel rotation, are analyzed. As well, errors in satellites' positions are introduced and their impacts on height retrieval and CCD are studied.

For the rest of Chapter 1, the simulation test model used for terrain height retrieval and coherent change detection is presented. This is followed by an overview of the height retrieval and CCD process.

Introduction of a third satellite to the conventional two-satellite InSAR provides us with three interferograms instead of one. In Chapter 2, we look into ways on making use of these additional data to improve the height retrieval process. In particular, the *height averaging* and *phase averaging* techniques applied on a non-collinear three-satellite setup will be discussed. Phase averaging, which involves combining the three interferograms into one, is a novel contribution of the thesis and shall be addressed in greater details. These include discussing various implementations of the phase averaging method and presenting simulation results of the retrieved height. Apart from attaining the DEM, InSAR is also widely used to detect temporal changes of the illuminated scenes, by observing them at different times [10, 11, 12]. Retrieving a CCD map by applying multilook coherence estimator [4] ignores the true topography and is therefore, slope dependent [13]. For the rest of Chapter 2, we shall look into ways of overcoming the slope biasing effects on CCD. In particular, we shall examine the performance of a multi-baseline approach in compensating for these effects.

In chapter 3, we related our three-satellite configuration to a more realistic setup by considering an interferometric cartwheel [6, 7], with the eventual hope of accounting for the errors introduced to the height retrieval and CCD process. A circular cartwheel is setup such that the three satellites are in constant motion even within a snapshot of the interferogram. However, only a set of the height retrieval parameters, corresponding to the satellite positions at the beginning of the shot, are assumed to be known. In that case, the interferogram may be perceived as imperfect for height inversion and CCD. Nonetheless, it was found that a self-compensating mechanism exists within such a setup itself so that we are still able to retrieve the terrain heights

correctly, upon application of a *weighted averaging* scheme. On the other hand, CCD is found to be less affected by the cartwheel's rotation but its performance is dependent on the relative positions of the satellites in the cartwheel. Cartwheel's impact on both height retrieval and CCD shall be addressed in this chapter.

Lastly, we account for the satellite positioning errors in Chapter 4 and attempt to retrieve the true satellites positions without knowledge of any ground truths, which would otherwise propagates into unacceptably large misalignments in the retrieved terrain profiles. This was achieved with cost minimization functions in a noiseless environment. As well, impacts of satellite positioning errors on CCD applications are studied.

This thesis concludes with a summary of the main findings.

1.3 The Test Model

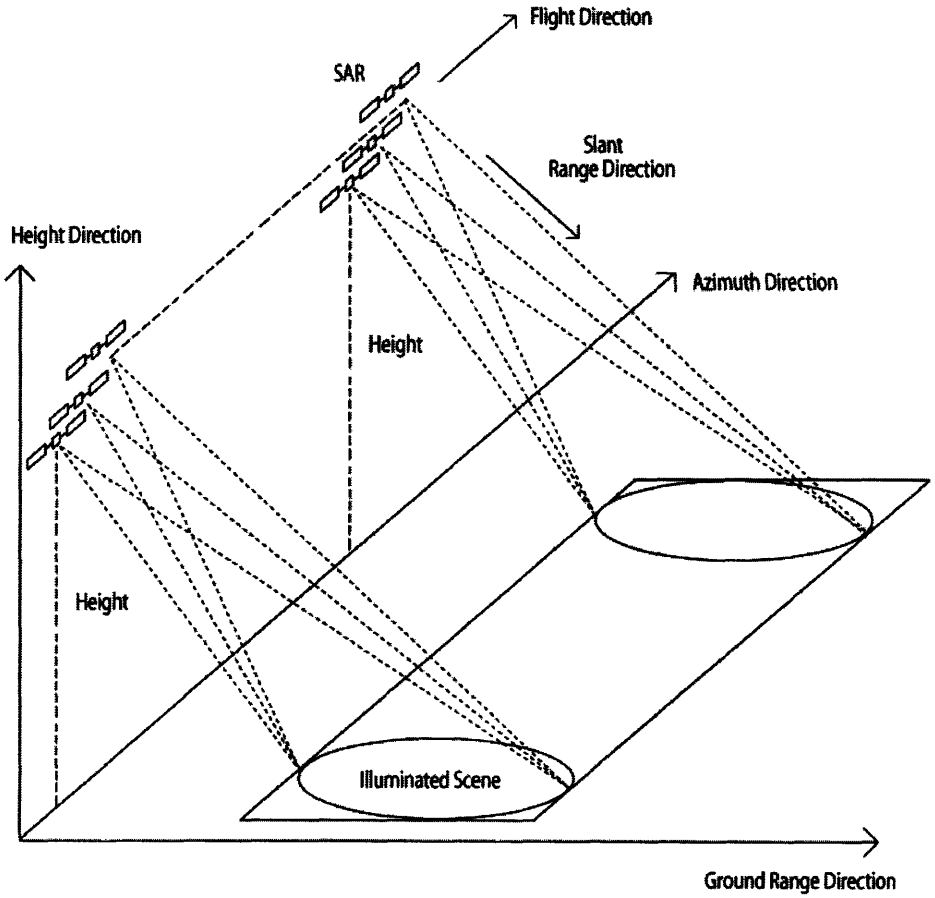

Figure 1-1: Three-dimensional coordinate system of a three-satellite InSAR setup.

Figure 1-1 shows a three-dimensional three-satellite SAR system. Each antenna is attached to a satellite and assumed to be active (i.e. both transmitting and receiving

signals). The satellite system is taken to be in stable orbit around earth, emitting signals over specified terrain of interest. The microwave signals transmitted by the antennas impinge on the terrain below, and backscattering effects allow a significant portion of the signal energy to get reflected back to the relatively slow moving SAR system. Since height retrieval is a post processing step done after data collection, we may consider the three satellites as coexisting in a *single-pass* orbit, or a single satellite passing over the same scene in consecutive passes (*repeat-pass*). One major concern in the latter is *temporal decorrelation* [14], which follows from physical changes in the scene over the time lapse between observations, and leads to deterioration of the DEM's quality. As we shall see in section 1.5, measurement of temporal decorrelation is in fact the primary focus in CCD. In the rest of this thesis, we shall assume a single-pass orbit due to its resemblance to the interferometric cartwheel.

In the three-dimensional coordinate system in figure 1-1, the single-pass SAR system advances in the azimuth direction, with its antennas side-looking in the range direction. Due to the extremely short time interval required to capture a scene, the satellites' heights above the ground is assumed to be constant. However, this no longer holds true when an interferometric cartwheel is considered, as we shall see in Chapter 3. As well, the Earth's curvature and its spin is ignored, allowing a flat earth assumption.

1.3.1 Two-Dimensional Three-Satellite Setup

In figure 1-2, we define a two-dimensional coordinate system typically used for side-looking InSAR. The diagram is a cut in the azimuth direction and contains the ground range and height directions (x-z coordinates). After applying pixel co-registration[1], we may assume the three satellites to simultaneously lie on this plane cut. B_{ij} is the length of the baseline formed between SAR i and SAR j, with $\{i,j\} = \{1,2,3\}, i \neq j$, while ρ_i is the absolute one-way slant range from satellite i to the ground pixels. A baseline elevation angle, α_{ij}, corresponding to each B_{ij} is defined as the angle between the baseline and the horizontal. θ is the look angle and H is the height of SAR 1 above ground. The illuminated scene is at a distance x away from SAR 1's nadir while Δz represents the height information that we are interested in.

In the conventional two-satellite InSAR where only SAR 1 and SAR 2 exist, the above setup simplifies as follows:

$$B_{23} = \alpha_{23} = \rho_3 = 0 \tag{1.1}$$

$$B_{12} = B_{13} \qquad \alpha_{12} = \alpha_{13} \tag{1.2}$$

Hence, we can think of the three-satellite case as a combination of three distinct sets of the two-satellite setup. This approach enables us to retrieve three sets of height

[1]See section 1.4.1

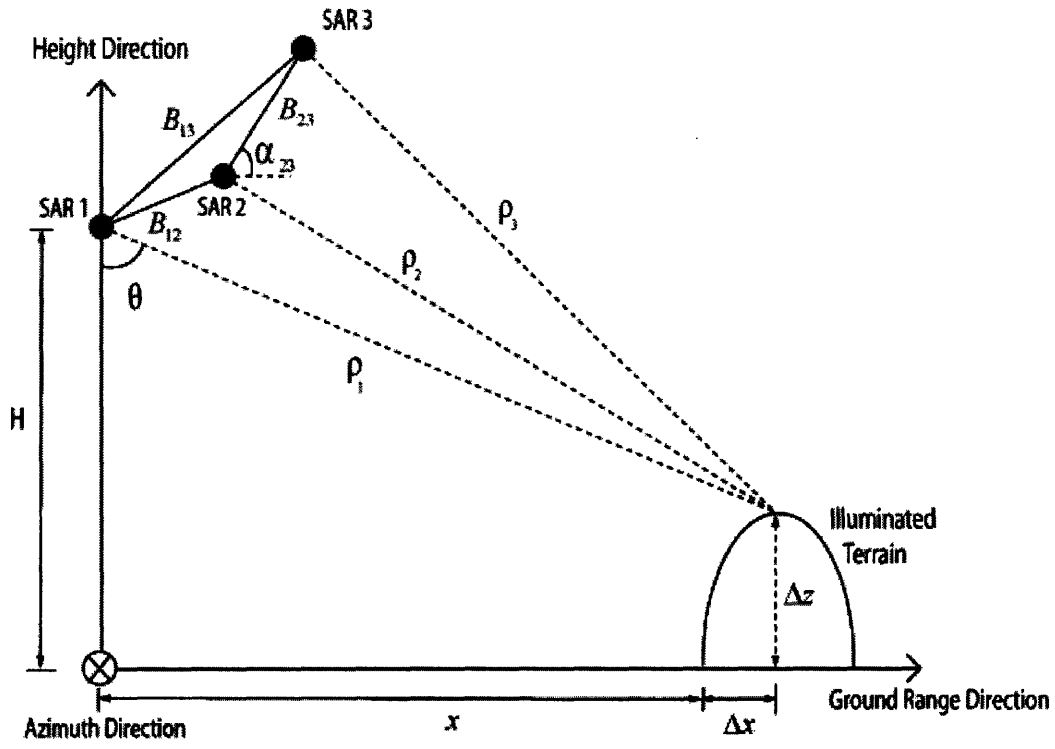

Figure 1-2: Two-dimensional coordinate system of a three-satellite InSAR setup.

information, which may be further post-processed (i.e. height averaging).

Let's consider a pair of satellite and their SAR images, i.e. SAR 1 and SAR 2 in figure 1-2. Each pixel in the SAR image corresponds to a point on the ground and contains a complex valued signal, $A_1 e^{j\phi_1}$ and $A_2 e^{j\phi_2}$. We can obtain a coherence value between the two images using the correlation coefficient, in its simplest form:

$$A_{12} e^{j\phi_{12}} = \left(A_1 e^{j\phi_1}\right) . \left(A_2 e^{j\phi_2}\right)^* \tag{1.3}$$

where $A_{12} = A_1 A_2$ and $\phi_{12} = \phi_1 - \phi_2$. While its phase data is essential in retrieving the DEM, its magnitude is a measure of the signal's reliability and is typically used for assigning the weighting values in the weighted phase unwrapping method.

One way to avoid attaining unreliable data (i.e. $A_{12} = 0$) is to ensure that the baseline length between any pairs of satellites used for height retrieval is less than the critical baseline length [14, 15, 16], in eq. 1.4:

$$B_{critical} = \frac{\lambda \rho}{2 R_x \cos^2 \theta} \tag{1.4}$$

λ is the wavelength of the transmit signal, ρ is the one-way slant range from the SAR to the center of a ground pixel, R_x is the ground range resolution, and θ is the look angle. Eq. 1.4 is satisfied when the change in look angle between SAR 1 and SAR 2 is sufficient to cause total decorrelation in backscattering from every ground pixel

[14].

We shall assume that all pixels have magnitudes of one in our simulations and use a residue weighted scheme[2] for phase unwrapping instead. This allows us to only deal with the interferometric phase data for height retrieval. However, this simplification can no longer be made when dealing with CCD.

The interferometric path length, δ, is defined as the one-way slant range difference between the satellites and the ground targets.

$$\delta_{12} = \rho_1 - \rho_2 \tag{1.5}$$

For an interferogram, Φ_{12}, formed from SAR 1 and SAR 2, the interferometric phase difference represented by each of its pixel is obtained through the following relationship [8]:

$$\Phi_{12} = \frac{4\pi}{\lambda}\delta = \frac{4\pi}{\lambda}(\rho_1 - \rho_2) \tag{1.6}$$

Eq. 1.6 is only true in the ideal case. In reality, the interferogram contains wrapped phase data and is corrupted by noise[3].

1.3.2 Test Terrain Model

Unless otherwise specified, the test terrain used in simulations is shown in Figure 1-3. It is a valley with an absolute height of $200m$. The mathematical representation of the terrain is:

$$\Delta z = 50\sin(\frac{X}{220} + 550) + 50\sin(\frac{Y}{220} + 550); \tag{1.7}$$

where Δz is the terrain height, X and Y are the distances from SAR 1's nadir in the ground range and azimuth direction respectively.

1.3.3 Simulation Parameters – Three or Two Satellites

With reference to figure 1-2 for a three-satellite non-collinear case, the system parameters required for simulations are defined in table 1.1. If considering a collinear setup instead, the only modification needed is that $\alpha_{12} = \alpha_{13} = 35°$ and $B_{13} = 200m$.

Since the three-satellite case can be related to the two-satellite case as explained in section 1.3.1, it is sometimes useful to examine the conventional two-satellite (i.e. SAR 1 and SAR 2) setup too. The systems parameters for such a setup is shown in table 1.2.

[2]See section 1.4.4
[3]See section 1.3.4

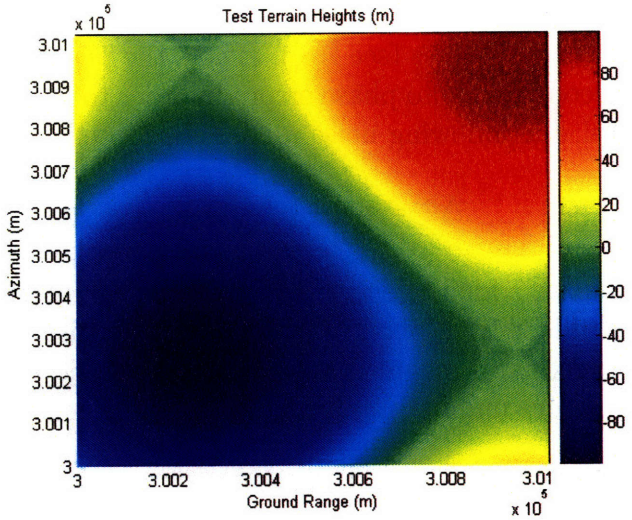

Figure 1-3: Two-dimensional plot of the test terrain.

Parameter	**Parameter Value**
Baseline length, B_{12}	$150m$
Baseline length, B_{13}	$250m$
Baseline elevation angle, α_{12}	$35°$
Baseline elevation angle, α_{13}	$45°$
Azimuth resolution, Δy	$4m$
Ground range resolution, Δx	$4m$
No. of pixels	256×256
Height of SAR 1, H	$5 \times 10^5 m$
Distance from nadir, X, Y	$3 \times 10^5 m$
Wavelength, λ	$0.3m$

Table 1.1: Simulation parameters for three-satellite non-collinear setup.

Parameter	**Parameter Value**
Baseline length, B_{12}	$200m$
Baseline elevation angle, α_{12}	$35°$
Azimuth resolution, Δy	$4m$
Ground range resolution, Δx	$4m$
No. of pixels	256×256
Height of SAR 1, H	$5 \times 10^5 m$
Distance from nadir, X, Y	$3 \times 10^5 m$
Wavelength, λ	$0.3m$

Table 1.2: Simulation parameters for two-satellite setup.

1.3.4 Noise Model

Thermal noise, in particular speckles (see [18]), affects the phase measurements. Pixels misregistration also contributes to phase error. In order to account for these noises in our simulation model, the following noise model is adopted:

$$\Delta\Phi = n\frac{\pi}{180}\{-1, 1\} \tag{1.8}$$

$\Delta\Phi$ is the white phase noise added to every pixel in the ideal interferogram of eq. 1.6. These errors are independent from pixel to pixel. n is the noise level in *degrees* and is used to specify the maximum magnitude of distortion made to the interferogram. $\{-1, 1\}$ represents a random number uniformly distributed between -1 and 1.

The above noise model is chosen mainly due to its simplicity. However, not all phase noises are white. For instance, [17] explained that besides the unavoidable white noise term, the interferometric phase data include an addictive term due to atmospheric inhomogeneities. Nonetheless, it may be argued that because of noise's random nature, the various noise models should have similar impacts on our height retrieval methods.

1.3.5 Root Mean Square Error

In order to evaluate the performances of our implementations in this thesis, the root mean square (RMS) error is computed. In particular, if we are retrieving heights, then, the RMS *height* error will be evaluated. For an interferogram of size a by b, the RMS height error is computed as:

$$r.m.s\ \ height\ \ error = \sqrt{\frac{1}{ab}\sum_{i=1}^{a}\sum_{j=1}^{b}[(h_{ij}^{noise} - h_{ij}^{original})^2]} \tag{1.9}$$

where h_{ij}^{noise} is the noise-affected height retrieved at the (i^{th}, j^{th}) pixel and $h_{ij}^{original}$ is the true terrain height at the (i^{th}, j^{th}) pixel.

Since noise is random, a more accurate measure of performances would be the mean RMS height error defined in eq. 1.10.

$$mean\ \ r.m.s\ \ height\ \ error = \frac{1}{N}\sum_{i=1}^{N}(r.m.s\ \ height\ \ error)_i \tag{1.10}$$

where N is the number of simulation trials. In this thesis, N is set to 20. The RMS error is also the standard deviation away from the true value as a result of noise's distortion. In the ideal case, mean RMS height error is zero.

Wong [8] has shown that the RMS height error, noise level and baseline length are

related as follows:

$$mean\ r.m.s\ height\ error \propto \frac{n}{B} \tag{1.11}$$

The above relationship suffices for a two-satellite or three-satellite collinear setup, provided that the baseline length is less than the critical baseline length of eq. 1.4. In the three-satellite non-collinear setup,the perpendicular baseline [17] shall instead be considered such that

$$mean\ r.m.s\ height\ error \propto \frac{n}{B_\perp} \tag{1.12}$$

$B_\perp$ is the projected baseline length in the direction perpendicular to the look direction, as shown in figure 1-4. Here, the rays from each satellites to a single target point are approximated to be almost parallel since $\rho \gg B$.

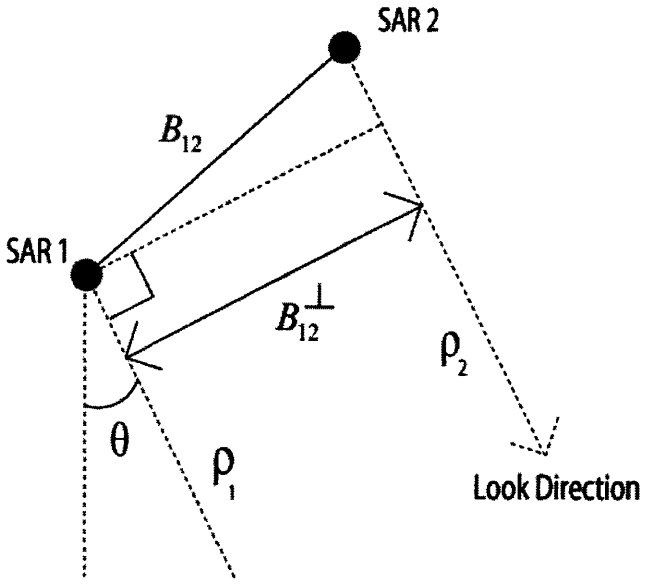

Figure 1-4: Perpendicular baseline length.

1.4 Height Retrieval Process

In this section, the various post-processing steps used in our simulator for height retrieval are presented. Assumptions made are highlighted as well. Figure 1-5 shows an overview of the process.

1.4.1 Image Co-registration

Prior to determining the pixel-to-pixel phase differences of the interferogram, the two complex SAR images has to be co-registered such that they are spatially aligned. This is a non-trivial process due to skewed radar trajectories and differing look angles [3]. In fact, misregistration in the range direction is more severe than in the azimuth

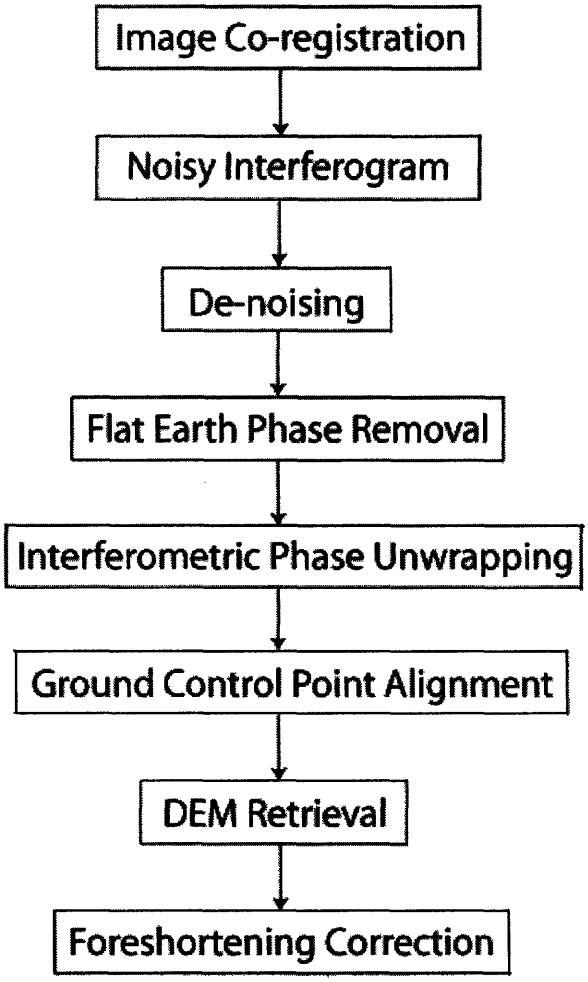

Figure 1-5: Flow chart of the implemented height retrieval process.

direction since the phase centers of the antennas are usually well-aligned along-track [16].

In general, co-registration requires the resampling of one of the images in both the azimuth and range directions. Since we are more interested in studying the height retrieval and CCD applications of InSAR, as well as analyzing the errors introduced by a cartwheel setup, we shall assume that each interferogram pixel is already aligned spatially. Any additional such errors would be factored into the noise model of section 1.3.4.

1.4.2 Interferometric Phase Denoising

Since two-dimensional phase unwrapping of the interferogram is a noise sensitive process, the presence of noise in measured interferograms directly affect the quality of the retrieved DEM. Denoising is a process that remove noise from the measured in-

terferograms prior to phase unwrapping.

Braunisch *et al.* [19] presented two methods of denoising: *complex interferogram averaging* and *wavelet denoising with soft-thresholding.* The former uses a 3×3 moving-average filter where each pixel in the measured interferogram is replaced by the complex average of the pixels over a localized window. An implementation of this method is explained in [9]. In implementing the wavelet denoising with soft-thresholding [20], we made used of the Daubechies orthogonal wavelet filters to perform a two-dimensional discrete wavelet transform (2D-DWT) decomposition, with the coarsest scaling at level four. Although the details of this denoising approach will not be elaborated further, it should be noted that thresholding here is automated. In figure 1-6, we compare the above two denoising methods to the case where no denoising is applied, in a two-satellite setup.

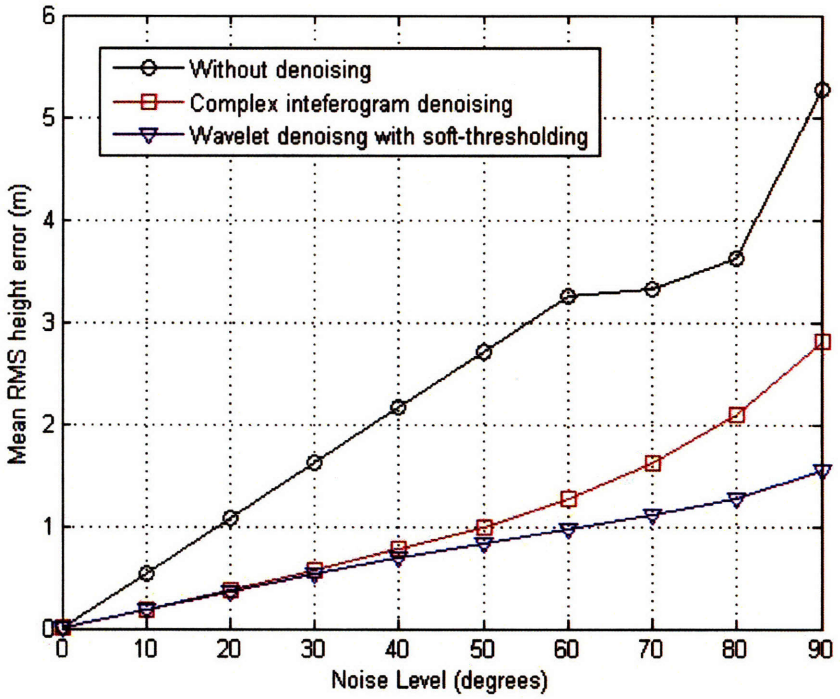

Figure 1-6: Comparison of the effects of interferometric phase denoising on height retrieval, using a two-satellite setup.

	Mean RMS height error (m)		
Noise Level (°)	**No Denoising**	**Complex Averaging**	**Wavelet Denoising**
0	9.29×10^{-8}	0.0116	3.28×10^{-4}

Table 1.3: Mean RMS height error at noise level = 0°, after application of interferometric phase denoising.

From figure 1-6, it is obvious that the mean RMS height error is reduced after application of denoising. In particular, in line with the conclusions of [19], wavelet denoising outperforms complex interferogram averaging. However, it is noted in table 1.3 that at 0° noise level, application of both denoising schemes result in higher error than with no denoising. This is an unique case where we can perceive denoising as a disruptive process applied to an already ideal interferogram. In practice, noise is always present.

Furthermore, it was observed in [19] that applications of both denoising methods to the wrapped interferogram render the iteration in weighted least-squares phase unwrapping obsolete. This immediate convergence of phase unwrapping greatly reduces the computation complexity of the height retrieval process. We shall, for the rest of this thesis, always apply wavelet denoising with soft-thresholding to the measured interferograms prior to phase unwrapping.

1.4.3 Flat Earth Phase Removal

The terrain height information is related to the absolute interferometric phase defined in eq. 1.6 whereas the complex-valued interferogram is measured modulo 2π (*wrapped phase*). As such, *phase unwrapping* is required to retrieve the absolute phase data.

Fringes are locations on the interferogram where 2π discontinuities occur. Existence of a large number of fringes, resulting from large phase variations, may degrade the performances of several phase unwrapping tools [21]. "Flat earth" phase removal is used to reduce these phase variations. The idea is to flatten the phase by removing a reference phase that characterizes the gross trend of the interferogram [22]. The flattened phase (eq. 1.16) is then unwrapped and the reference phase added back to yield an unwrapped and unflattened interferogram.

Since the satellites' locations are known, we compute the reference phase by assuming a flat terrain in the illuminated scene. A wrapping operator, $W\{.\}$ is defined such that

$$W\{x + 2\pi n\} = x \tag{1.13}$$

where n is an integer and $-\pi \leq x < \pi$. Then, from eq. 1.6, the measured interferogram (wrapped) is

$$\phi_{12} = W\{\Phi_{12}\} = W\{\phi_{12} + 2\pi n\} \tag{1.14}$$

Applying flat earth removal to reduce phase variations, eq. 1.6 becomes

$$\begin{aligned} \Phi_{12}^{flat} &= \frac{4\pi}{\lambda}\left((\rho_1 - \rho_1^{flat}) - (\rho_2 - \rho_2^{flat})\right) \\ &= \frac{4\pi}{\lambda}\left((\rho_1 - \rho_2) - (\rho_1^{flat} - \rho_2^{flat})\right) \\ &= \Phi_{12} - \Psi_{12} \end{aligned} \tag{1.15}$$

where ρ_1^{flat} and ρ_2^{flat} are the one-way slant range from SAR 1 and SAR 2 respectively to the assumed flat terrain, and Ψ_{12} is the absolute flat earth phase removal term. Note that ρ_1^{flat}, ρ_2^{flat} and hence, Ψ_{12} are known quantities. Since we are dealing with wrapped measured data, eq. 1.15 is implemented as follows:

$$\begin{aligned} W\{\Phi_{12}^{flat}\} &= W\{\Phi_{12} - \Psi_{12}\} \\ &= W\{\phi_{12} + 2\pi n_1 - \psi_{12} - 2\pi n_2\} \\ &= W\{\phi_{12} - \psi_{12}\} \end{aligned} \tag{1.16}$$

Eq. 1.16 shows that a wrapped version of the absolute flat earth phase removal term, ψ_{12}, is subtracted from the interferogram, before wrapping is carried out once more to attain $W\{\Phi_{12}^{flat}\}$. This output is then unwrapped to retrieve Φ_{12}^{flat} and *added* to Ψ_{12} to attain the desired unwrapped data, Φ_{12}.

1.4.4 Interferometric Phase Unwrapping

The measure phase differences are wrapped according to eq. 1.13 into the range $[-\pi, \pi)$. Phase unwrapping is a process of recovering the lost integral number of cycles, and must be carried out before terrain heights can be retrieved. Without the presence of noise, fringes in the interferogram can be easily located and multiples of 2π added to produce an unwrapped data. However, noise-corrupted real-world data necessitate the development of more sophisticated phase unwrapping algorithms.

Phase unwrapping can be generalized into two methods: local and global. Local methods unwrap a pixel depending only on its nearest neighboring pixels whereas global methods consider the entire set of pixels to be unwrapped. *Weighted least-squares* unwrapping is a global approach that attempts to minimize the difference between the wrapped derivatives of the measured data and the derivatives of the solution. It is implemented by employing a rapid, iterative method based on fast cosine transforms and preconditioned conjugate gradients to solve the least squares partial differential equations [24, 25]. *Residue-cut* unwrapping, on the other hand, is a local method where the solution is derived from integrating the fringes. It identifies the residue (phase inconsistencies) in the interferogram and "balances" them by forming branch cuts [26]. Other local methods include the region growing phase unwrapping [27, 28, 29]. All these different approaches aim to reconstruct the absolute phase data, starting from an interferogram distorted by noise, shadowing and layover effects.

Each of the above mentioned methods has its pros and cons. The strength of the least-squares approach is that the phase values are unwrapped everywhere in the image. However, errors leading to an underestimate of the recovered phase slopes follow from the assumption that the unwrapped phase field is continuous everywhere. The residue-cut method does not suffer from this problem since branch cuts can be formed so that integrations are avoided at sites of inherent phase discontinuities, without having to enforce continuity. This method, however, does not always yield a complete solution. Zebker and Lu [30] suggested a hybrid method by using the residues of the

residue-cut method as weights of the weighted least-squared method. They demonstrated that this hybrid method perform the best in terms of unwrapping accuracy when compared to the original residue-cut, least-squares or coherence-weighted least-squares methods, while ensuring complete coverage. A similar conclusion is arrived in [9].

We shall adopt this hybrid method for two-dimensional phase unwrapping in our implementation and simply referred to it as the weighted least-squares method. Since the algorithm works best with binary-valued weights [31], we assign a weight of zero to pixels where residues exist and one otherwise.

1.4.5 Ground Control Point Alignment

Interferometric phase unwrapping process as described in section 1.4.4 only recover the phase data to within a constant of the desired absolute phase. A known reference height in the scene, commonly referred to as a ground control point (GCP), is needed to evaluate this constant. In our simulations, we assumed that the GCP lies at the $(1, 1)$ pixel of the interferogram.

1.4.6 DEM Retrieval

Upon recovery of the absolute phase data from the interferogram, we are now able to retrieve the terrain heights (DEM) by using the geometry of the SAR setup [8]. For the purpose of the following formulation, we shall again consider a two-satellite setup of SAR 1 and SAR 2, with close reference to figure 1-2. Firstly, recognize that the unwrapped phase, Φ_{12} is directly proportional to the one-way slant range difference of the satellites, as in eq. 1.6, such that

$$\delta_{12} = \frac{\lambda}{4\pi}\Phi_{12} \tag{1.17}$$

Using cosine rule on the setup's geometry, the following relationship between the look angle, θ, and δ can be established:

$$\theta_{12} = \alpha_{12} + \sin^{-1}\left(\frac{\delta_{12}}{B_{12}} + \frac{B_{12}}{2\rho_1} - \frac{\delta_{12}^2}{2B_{12}\rho_1}\right) \tag{1.18}$$

Then, the height, Δz, is obtain by

$$\Delta z_{12} = H - \rho_1 \cos\theta_{12} \tag{1.19}$$

Eq. 1.19 is applied on a pixel-by-pixel basis so that if we have a two-dimensional interferogram, then, a three-dimensional DEM is obtained. Also, while the above illustrates a two-satellite case using SAR 1 and SAR 2, the same approach works on all pairs of satellites in the setup of figure 1-2, by using the appropriate Φ and its corresponding parameters B, θ, α, ρ and H.

1.4.7 Foreshortening Correction

SAR systems measure data in the azimuth and slant range directions while in the DEM, the heights are plotted against the azimuth and ground range directions. In the former, it becomes possible that a taller object further away in ground distance from the SAR's nadir, to have a smaller slant range than a shorter object nearer nadir. An illusion is created such that, in terms of slant range distances, the taller object appears nearer to the SAR than it really is. This phenomenon is known as the *layover effects* [32].

Foreshortening is a process that adjusts the position of each pixel along the range direction to compensate for the fact that range pixels are not necessarily in order as far as the ground dimension is concerned. An approximated correction term that is dependent on the retrieved height [8] is added to the ground-projected slant range distance of every pixel so that we are able to attain the $(X + \Delta x)$ ground distance of figure 1-2. In this way, all pixels are shifted in the image and equal pixel spacing is achieved by interpolation at the ground range resolution of the SAR configuration.

In our analysis, we shall assume that foreshortening correction are applied perfectly so that we can only be concerned with the performance of height inversion due to the multi-baseline configuration, and not how well foreshortening corrections are accounted for. Nonetheless, any possible such errors can be factored crudely into our noise model.

Next, an overview of InSAR change detection techniques is discussed.

1.5 Change Detection of Imaged Scenes

Change detection involves interrogating a scene with a SAR system at two different times, ranging from hours to weeks. The resultant two SAR images, commonly referred to as the *reference* and *test* data [36], are used to determine where targets have entered or left the imaged scenes between the two data acquisitions. Even subtle differences, not visible to the naked eyes, can be detected. Applications of SAR systems to identifying scene changes include the detection of vehicle movement [39], mines deployment, urban development and geographical changes [40].

Two approaches to detecting changes are identified in [10]. The first set of techniques detect changes based on differences in the magnitudes of the signal intensities in the two images, by taking their ratios. The second set of techniques, also known as *coherent change detection* (CCD), accounts for the temporal decorrelation of speckle, which can be achieved through the magnitudes of the complex cross correlation of the SAR image pair. The two methods measure different properties of a scene. While the coherent detection approach indicates whether the positions of the image scatterers have been altered or totally changed, it provides no indication on the magnitudes

of change in radar backscatter. On the other hand, the backscatter-power ratio technique measures the magnitudes of the radar backscatter change, and thus, the dielectric properties of the scenes so that change detection in soil moisture content or surface roughness is possible.

In [37], the authors recognized the need to consider both the above change statistics in order to properly characterize the scene changes and to reduce the false-alarm rates. Fusion of both statistic is accomplished by forming a log-likelihood ratio. In this thesis, we shall only be concerned with physical changes of the scene content and the ability to discriminate between the reference and test data using coherent change detection techniques.

The initial implementation to be analyzed here utilizes a single satellite antenna in a nearly-exact repeating orbit, that forms the interferometer baseline by relating radar signals on repeat passes over the same site. Our analysis will eventually involve making use of two or more physical antennas (i.e. interferometric cartwheel configuration) illuminating the ground simultaneously. Despite the antennas illuminating the same scene at different times, received signals will remain highly correlated if the ground is completely undisturbed [14].

1.5.1 Coherent Change Detection

Similar to eq. 1.3, a more general form of the correlation coefficient [4, 13] between a pair of SAR images is

$$\rho = |\rho| e^{j\phi} = \frac{E\{S_1 S_2^*\}}{\sqrt{E\{|S_1|^2\} E\{|S_2|^2\}}} \tag{1.20}$$

where S_1 and S_2 are the complex values of the two SAR images, $E\{.\}$ is the ensemble average, * is the complex conjugate and ϕ is the interferometric phase containing topography information. The amplitude of eq. 1.20, $|\rho|$, called coherence, determines the precision of the retrieved DEM and accounts for coherence losses when the SAR images are acquired at different times. These losses include that due to physical scene changes, which is our primary interest in this chapter. In section 1.5.2, three decorrelation factors contributing to coherence loss shall be discussed.

Assuming that S_1, S_2 and $S_1 S_2^*$ are homogenous and ergodic in mean, eq. 1.20 may be estimated locally, by ensemble averaging $M \times N$ neighboring pixels in the complex data

$$|\rho| = \frac{\left| \sum_{m=1}^{M} \sum_{n=1}^{N} S_1(m,n) S_2^*(m,n) \right|}{\sqrt{\sum_{m=1}^{M} \sum_{n=1}^{N} |S_1(m,n)|^2 \sum_{m=1}^{M} \sum_{n=1}^{N} |S_2(m,n)|^2}} \tag{1.21}$$

where m and n are the spatial coordinates and $0 \leq |\rho| \leq 1$. This is known as the multilook coherence estimator [4] and is commonly used to detect changed regions of a scene. In our implementation, constant amplitudes of the SAR data are assumed [29] and square windows (i.e. $M = N$) of size 3×3 are used. Larger sized windows, though better adapted to reducing the statistical scattering of the measurement, have a greater trade-off in terms of the loss of spatial resolution and details.

According to [38], the above method can be classified as a pixel-based approach of detecting changes. Another class would be the feature-based approach which is still in the preliminary design stage and is capable of reducing misregistration problems of SAR data. It should be highlighted that a first attempt in combining the two approaches has already been made [38] and the results are promising. Since accounting for co-registration is not our focus in this thesis, this approach shall not be elaborated further.

1.5.2 Decorrelation in Interferometric SAR Data

It was mentioned that if the illuminated scene is completed undisturbed, then the coherence value, $|\rho|$, of the two SAR images of the same scene taken at different times would be high. However, this is not always true since coherence losses are not solely dependent on changes in the relative positions of the scene's scatterers. Inexact satellite repeat track leading to varying observation geometry of each SAR image is another cause of coherence loss. In [14], three independent sources of decorrelation has been identified: decorrelation due to the nonidentical sensors viewing directions, $\rho_{spatial}$, decorrelation due to actual changes of the targets, $\rho_{temporal}$, and lastly, scene decorrelation due to thermal noises of the receivers, $\rho_{thermal}$. An expression for the total correlation was arrived as:

$$\rho_{total} = \rho_{spatial+temporal+thermal} = \rho_{spatial} \cdot \rho_{temporal} \cdot \rho_{thermal} \tag{1.22}$$

Ideally, we would want ρ_{total} to be entirely dependent on $\rho_{temporal}$ in CCD applications such that $\rho_{spatial}$ and $\rho_{thermal}$ equal one. This way, we may infer the physical properties of the scene without being confused by instrumental effects. However, $\rho_{spatial} = 1$ can only be achieved via an exact satellite repeat track, which is impractical to attain. Hence, this non-zero baseline between the two satellite passes is a major contributor to coherence losses and we seek to account for it in our coherence data. In eq. 1.4, $B_{critical}$ is the maximum separation between the satellite passes before $\rho_{spatial}$ becomes zero. In that case, total decorrelation in the backscattering signals occurs, i.e. $\rho_{total} = 0$, rendering the phase data useless for height retrieval. As well, it is no longer possible to retrieve the value of $\rho_{temporal}$.

Having introduced the simulation test model as well as the general height retrieval and CCD process, we shall next examine in greater details the multi-baseline height retrieval techniques. The slope biasing effects on CCD will be discussed and possible solutions presented.

Chapter 2

Multi-baseline Height Retrieval and CCD

The introduction of a third satellite, SAR 3, to the conventional InSAR two-satellite configuration of SAR 1 and SAR 2 provides two additional baselines, B_{13} and B_{23}. This corresponds to a total of three interferograms instead of one that are available for height inversion. In section 1.3.1, we noted the traditional view of treating the multi-baseline setup as a combination of distinct satellite pairs. This way, three separate height data of the same terrain can then be retrieved and later post-processed to reduce noise errors via height averaging, to be discussed in section 2.1.

In section 2.2, a novel approach of combining the multi-baseline data, called *phase averaging*, is investigated. Instead of combining the final retrieved heights, we now seek to combine the three interferograms before the height retrieval process so that only one set of height data, corresponding to a virtual baseline, is attained. A new virtual baseline has to be utilized since alterations to the interferograms correspond to changes in the satellites geometries. The main advantage of this multi-baseline approach over the conventional view of distinct satellite pairs is that the combined phase data may now be treated as if it is from a pair of satellites, enabling the application of the original height inversion process to the three-satellite case without need for excessive modifications. We shall discuss the implementations of such an approach, analyze its impact on height inversion and compare the results with height averaging techniques. The collinear configuration shall first be addressed. After which, it becomes trivial to extend the same idea to a non-collinear satellites configuration.

In section 2.3, relationships between the terrain slope, baseline length between satellite passes and the coherence values are examined. It was found that application of the multilook coherence estimator of eq. 1.21 resulted in coherence losses due to terrain slope variations, eventually leading to misinterpretation of changes in the imaged scenes. The topography-corrected and wavelet transform-based coherence estimators are applied to compensate for these slope biasing effects.

2.1 Height Averaging Technique

2.1.1 Data Averaging

Wong [8] has shown that in a three-satellite setup, the *data averaging* method is effective in reducing the root-mean-square height error[1]. This is a simple method extending from the results obtained using the two-satellite model. Here, the three sets of data, corresponding to each of the three available baselines, are grouped into pairs, and the two statistical best data pairs are averaged to produce an improved estimate of the DEM. Data averaging is applied considering eq. 2.1:

$$h_{average} = \left(\frac{w_{12}h_{12} + w_{23}h_{23} + w_{13}h_{13}}{w_{12} + w_{23} + w_{13}} \right) \tag{2.1}$$

where h_{ij} is the height profile corresponding to each of the three available baselines formed between satellite i and j (i.e. B_{ij}), with $\{i, j\} = \{1, 2, 3\}, i \neq j$. w_{ij}'s are the appropriate weighting functions.

If h_{12} and h_{13} give the two best height profiles data, then, for data averaging, eq. 2.1 simplifies to:

$$h_{average} = \left(\frac{h_{12} + h_{23}}{2} \right) \tag{2.2}$$

where the following weighting functions are applied:

$$w_{12} = 1; w_{13} = 1; w_{23} = 0 \tag{2.3}$$

Wong pointed out that the above weights assignment does not give the optimum solution. In section 2.1.2, we shall explore a more comprehensive weighting function that accounts for the baseline lengths. Nonetheless, the data averaging method shall be used as the basis of comparison in analyzing other three-baseline InSAR height retrieval methods due to its simplicity and effectiveness, as concluded in [8]. Moreover, data averaging works for both the collinear and non-collinear satellites configuration.

2.1.2 Weighted Averaging

Before proceeding further to integrate all three multi-baseline interferograms, a digression will be made to introduce a new weighting scheme, either than the one already defined for data averaging in eq. 2.3, to be applied to eq. 2.1. Later, we will compare the performance of this scheme to that using unity weights and to both data and phase averaging, in terms of the RMS retrieved height error. It turned out that this proposed weighted averaging scheme outperforms data averaging and shall eventually be used to combine all interferograms of the three-satellite configuration

[1] See section 1.3.5

in application of phase averaging.

Ferretti *et al.*, in [17], combines the multi-baseline DEM data, derived by means of a multi-look Gaussian estimation, as follows:

$$\hat{h} = \frac{\sum_{i=1}^{N} \frac{h_i}{\sigma_{hi}^2}}{\sum_{i=1}^{N} \frac{1}{\sigma_{hi}^2}} \tag{2.4}$$

where h_i is the DEM retrieved from the i^{th} interferogram and σ_{hi}^2 is the associated noise variance. In order to relate the weighted averaging of eq. 2.4 to the baseline lengths, relationship between the height dispersion and phase dispersion [14] is used.

$$\sigma_h = \frac{h_{2\pi}}{2\pi} \; . \; \sigma_e = \frac{\lambda}{4\pi} \frac{r}{B_\perp} \sin\theta \; . \; \sigma_e \tag{2.5}$$

where $h_{2\pi}$ is the height variation corresponding to one cycle phase variation, $B_\perp$ is the perpendicular baseline, θ is the look-angle, r is the slant range distance from satellite to target, λ is the wavelength, σ_e is the phase error in the interferogram, and σ_h is the corresponding height error. Hence, by relating

$$\sigma_{hi}^2 = \frac{1}{B_{\perp i}^2} \tag{2.6}$$

with $B_{\perp i}$ being the perpendicular baseline corresponding to interferogram i, eq. 2.4 is eventually modified to become

$$\hat{h} = \frac{\sum_{i=1}^{N} B_{\perp i}^2 h_i}{\sum_{i=1}^{N} B_{\perp i}^2} \tag{2.7}$$

Eq. 2.7, referred to as *weighted height averaging*, shall be the new weighted averaging scheme adopted for the three-satellite setup such that the weighting function is

$$w_{12} = B_{\perp 12}^2; w_{13} = B_{\perp 13}^2; w_{23} = B_{\perp 23}^2 \tag{2.8}$$

Simulation Results

Figure 2-1 depicts the mean RMS height error plot of various averaging techniques applied on a non-collinear three-satellite setup as described in section 1.3. These include data averaging, phase averaging, weighted averaging of eq. 2.1 with eq. 3.7's weighting function applied (unity-weighted averaging), and the baseline-weighted av-

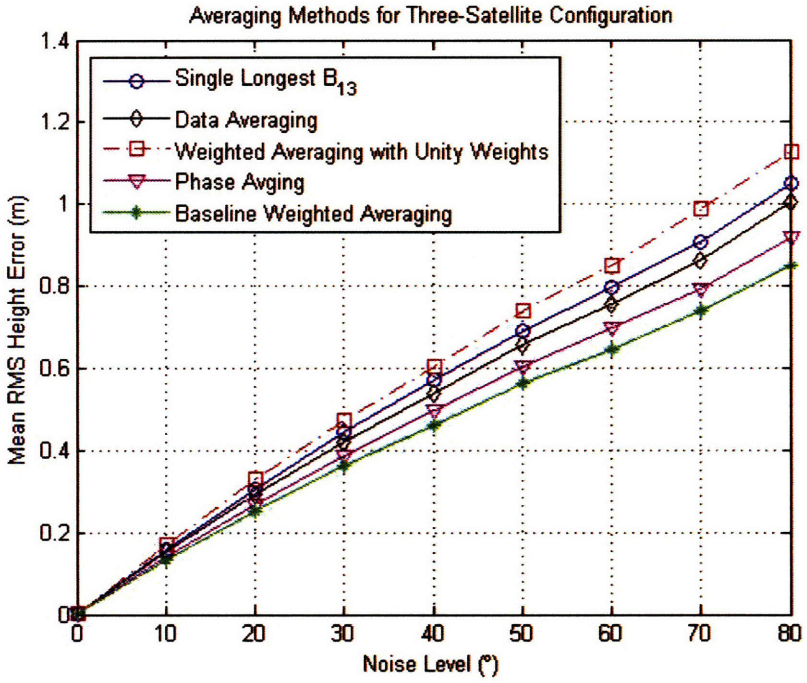

Figure 2-1: Data averaging, phase averaging and baseline-weighted averaging methods applied on a three-satellite configuration.

	Mean RMS height error (m)				
Noise Level (°)	**Single Longest Baseline**	**Data Averaging**	**Unity Weighted Averaging**	**Phase Averaging**	**Baseline Weighted Averaging**
0	0.0004	0.0003	0.0003	0.0005	0.0003
10	0.1576	0.1521	0.1705	0.1409	0.1319
20	0.3036	0.2911	0.3278	0.2686	0.2502
30	0.4435	0.4206	0.4732	0.3885	0.3613
40	0.5712	0.5393	0.6056	0.4973	0.4617
50	0.6899	0.6580	0.7383	0.6057	0.5618
60	0.7977	0.7567	0.8496	0.6971	0.6459
70	0.9073	0.8628	0.9878	0.7935	0.7376
80	1.0514	1.0033	1.1279	0.9199	0.8503

Table 2.1: Mean RMS height error of data averaging, phase averaging and baseline-weighted averaging applied on three-satellite non-collinear configuration.

eraging of eq. 2.7. The corresponding data are tabulated in table 2.1.

As already concluded in [8], unity-weighted averaging performs worse than without averaging, when only data corresponding to the single longest baseline, B_{13}, is considered. Similar to conclusions to be drawn in section 2.2.7, data averaging outperforms both unity-weighted averaging and single baseline data while phase averaging does better than them all. The baseline-weighted averaging which would be applied as part of the cartwheel height retrieval process turns out to be the most robust to noise and give the lowest mean RMS height error at all noise levels.

2.2 Phase Averaging Technique

2.2.1 Three-Satellite Collinear Configuration

Figure 2-2 and figure 2-3 show the collinear satellites setup that we will consider in this section, with their flight paths along the azimuth direction. In figure 2-2, the three satellites are lined-up and their corresponding slant range, ρ, are shown. Since $\rho \gg B$, we can approximate the three slant range directions to be parallel, i.e. $\rho_1 \parallel \rho_2 \parallel \rho_3$. Figure 2-3 depicts this approximation.

Eq. 1.6 relates the unwrapped interferogram, Φ, directly to the one-way slant range difference, δ, between the satellites. Similarly, the wrapped interferogram, ϕ, is also directly proportional to δ. For now, only the absolute phase data shall be considered, with the slant range difference being related to the unwrapped interferogram (Φ_{12} and Φ_{13}), as illustrated in figure 2-3.

We shall start off the analysis by manipulating only *two* phase data of the available three, which correspond to the longer perpendicular baselines. Apart from simplifying our investigation, this approach allows us to readily compare the performance of phase averaging to that of data averaging, already discussed in section 2.1.1. To combine all three data, the baseline-weighted averaging technique presented in section 2.1.2 will be used as the basis of the three-interferogram phase averaging scheme.

Single Height Method

As what was done in data averaging, two interferograms of the three available are selected. With reference to eq. 1.12, we chose the interferogram selection criteria to be based on the longest projected baseline length. In our current setup, this corresponds to B_{12} and B_{13}. Hence, starting with ϕ_{12} and ϕ_{13}, the two interferograms are first aligned spatially, follow by independent applications of denoising, flat earth phase removal, weighted least square unwrapping and GCP alignment on each of them, to eventually attain Φ_{12} and Φ_{13}.

At this stage, instead of retrieving a DEM from each of the unwrapped phase data,

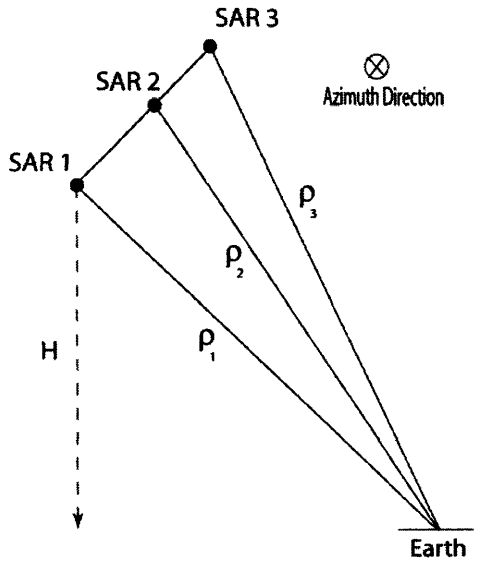

Figure 2-2: Three-satellite collinear geometry.

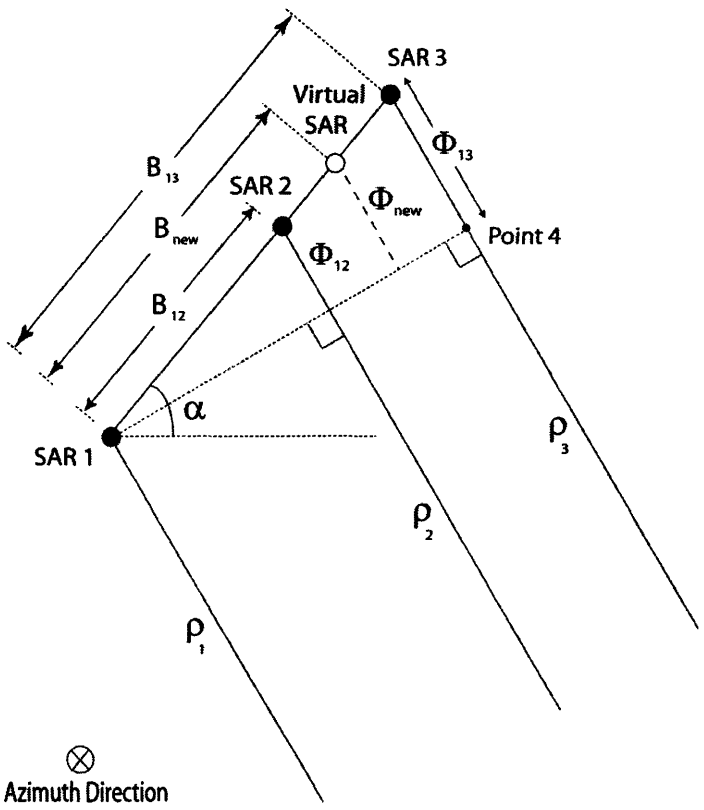

Figure 2-3: Three-satellite collinear geometry, with parallel slant range approximation.

we seek to combine Φ_{12} and Φ_{13} in the following way, so that only a single DEM is attained from the multi-baseline data:

$$\Phi_{new} = \frac{\Phi_{12} + \Phi_{13}}{2} \tag{2.9}$$

Since our phase data is related to the geometry of the satellites setup, we shall relate Φ_{new} in eq. 2.9 to figure 2-3 using similar triangle concepts, applied on the triangle bounded by SAR 1, SAR 3 and point 4 (i.e. $\triangle$(SAR 1, SAR 3, point 4)). Thus,

$$\frac{\Phi_{12}}{B_{12}} = \frac{\Phi_{13}}{B_{13}} \tag{2.10}$$

Using eq. 2.9 and defining a B_{new} as shown in the setup,

$$\frac{\Phi_{new}}{B_{new}} = \frac{\Phi_{13}}{B_{13}}$$

$$B_{new} = \frac{B_{13}\Phi_{12}}{2\Phi_{13}} + \frac{B_{13}}{2}$$

Applying eq. 2.10 to the above,

$$B_{new} = \frac{B_{12} + B_{13}}{2} \tag{2.11}$$

From eq. 1.18 and eq. 1.19, the parameters required for height inversion are ρ, B, α and Φ. Upon modification of the phase data according to eq. 2.9, ρ and α used for height retrieval remains the same (i.e. ρ_1) while the corresponding change in B is derived in eq. 2.11, using similar triangle approximation.

As such, we can now retrieve a single DEM using the combined multi-baseline data of Φ_{new}, B_{new}, ρ_1 and α. In fact, we may replace the three-satellite system with only SAR 1 and a virtual SAR, as indicated in the figure. It should, however, be emphasized that the interferogram corresponding to this pair of satellites are a result of combining two interferograms from the original setup. We shall refer to this phase averaging technique, where each of the original interferograms are processed and unwrapped individually before combining, as the *single height method.*

Single Interferogram Method

Another approach to the same phase averaging method is to combined the spatially aligned wrapped interferograms right before weighted least-squares unwrapping instead. In this case, we first obtain

$$\phi'_{new} = \phi_{12} + \phi_{13} \tag{2.12}$$

After phase unwrapping, the absolute phase data of eq. 2.9, is attained as follows:

$$\Phi_{new} = \frac{\Phi'_{new}}{2} \tag{2.13}$$

After retrieving Φ_{new}, a single DEM may be retrieved exactly as described in the single height method. We shall name this approach of combining the interferograms before weighted least-squares unwrapping as the *single interferogram method.*

The advantage of the single interferogram method over the single height method is that nearer the onset of the height retrieval process, after flat earth phase removal is applied, the combined multi-baseline data may be treated as if it is from a pair of satellites, SAR 1 and virtual SAR. This way, the conventional height inversion process designed for satellite pairs can be applied to the three-satellite case without the need for excessive modifications. However, as we shall see and explain in section 2.2.7, this approach will eventually breakdown at high noise environment while the single height method remain stable. In section 2.2.4, the performances of both phase averaging techniques, applied on the collinear setup of figure 2-3, will be examined.

Similar Triangle Approximation

The phase averaging method derived is based on the parallel slant range approximations such that similar triangle concepts may be applied. As a result, the α and B_{new} corresponding to Φ_{new} that we used for height inversion are also approximated values. Since the retrieved heights are sensitive to the parameters' accuracies, these inexact height retrieval parameter values will propagate into unacceptable retrieved height errors. From our three-satellite collinear setup simulations, it was found that applications of the phase averaging methods, without accounting for similar triangle approximation, as described in section 2.2.1 resulted in vertical shift of the retrieved heights away from the original terrain by $\sim (1-5)m$. These vertical shifts of the terrain are similar to the observations made when inexact baseline parameters are used for height inversion [8].

To account for this error, the following are noted:

- Φ_{new} is defined according to eq. 2.9 and 2.13.
- SAR 1 is used as a pivot between the original and new setup, so its position remains the same and no uncertainties exist in ρ_1 parameter value.
- Inexact α and B_{new} parameters are the cause of the terrain misalignment and can be rectified using the single GCP available, in one of the following two ways:
    1. Estimate α_{new} from similar triangle geometry and then find B_{new} using the GCP. In the current collinear setup, the estimated α_{new} will be equal to the original α.

2. Estimate B_{new} from similar triangle geometry, as in eq. 2.11, and then find α_{new} using the GCP.

α_{new} or B_{new} is attained via the GCP by back-solving eq. 1.19 and eq. 1.18. In our implementation, the latter approach is adopted. After the above correction, we are then able to retrieve the exact terrain profile in a noiseless environment using phase averaging with a virtual satellite.

2.2.2 Interferograms Manipulations

An overview of how the phase data are handled in the data averaging, single height and single interferogram methods is presented in figure 2-4. The distinction between single height and single interferogram is that the phase data are combined *after* unwrapping in the former while in the latter, they are combined *before* unwrapping. Nonetheless, both approaches result in a single DEM retrieved from the multi-baseline data. In data averaging, two interferogram is processed independently to attain two sets of DEM, which is then averaged to attain the final terrain profile. Though this section only deals with combining two of the three available phase data, the same approaches apply to the general case of fusing all three data.

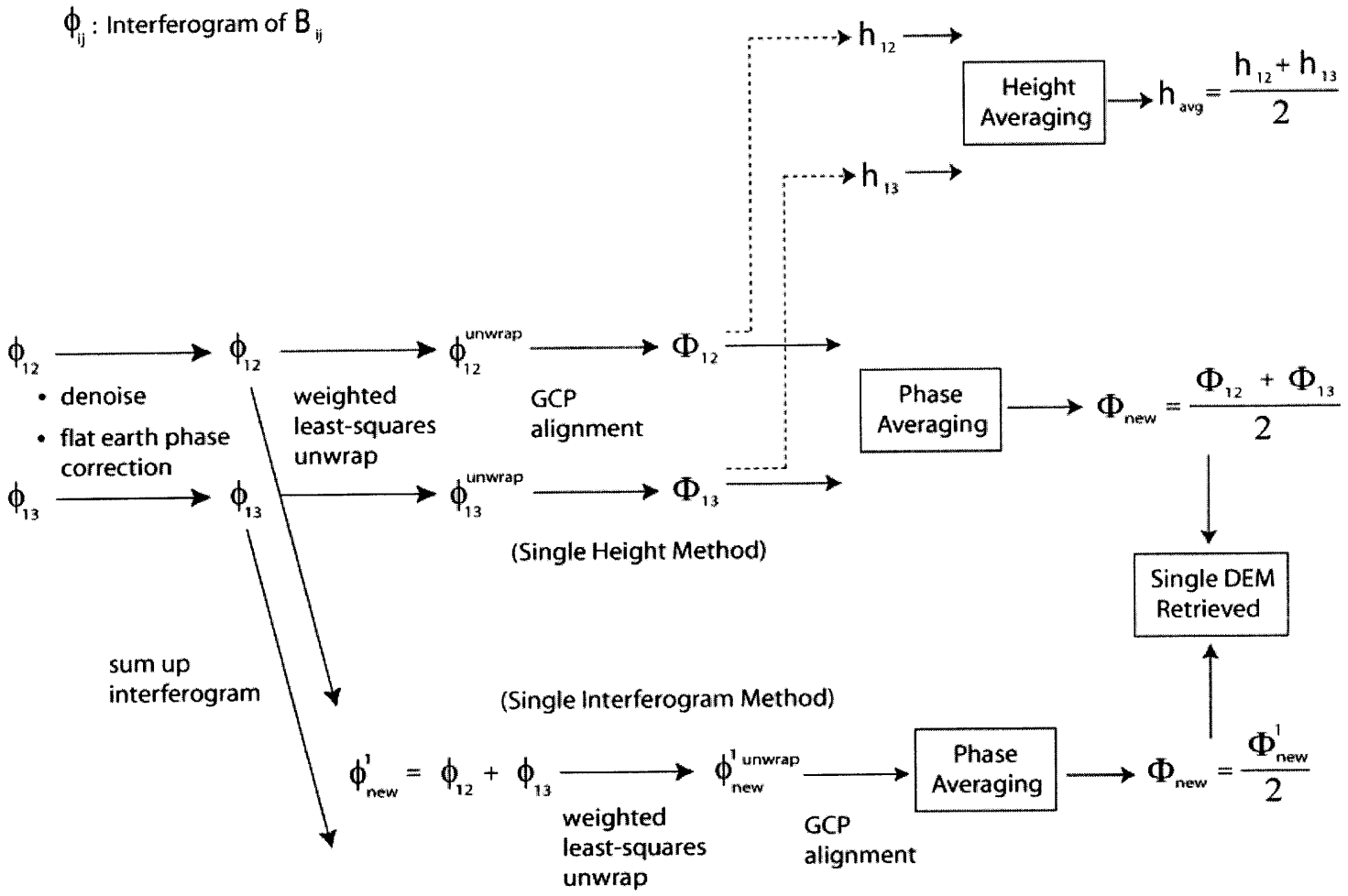

Figure 2-4: Interferograms manipulations for the data averaging, single height and

2.2.3 Weighted Phase Averaging on Collinear Setup

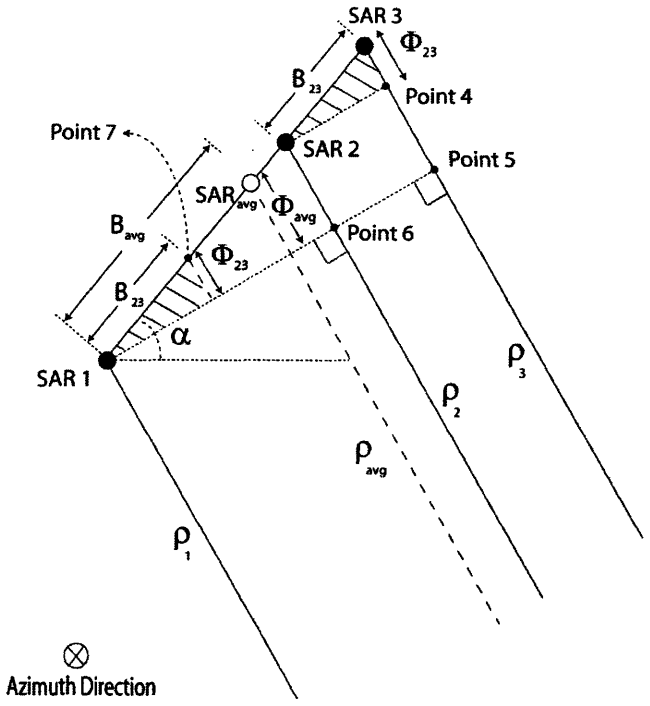

Figure 2-5: Three-satellite collinear geometry, for application of the weighted averaging scheme.

Similar to the single height and single interferogram method applied on Φ_{12} and Φ_{13}, manipulations of the three phase data (i.e. Φ_{12}, Φ_{13} and Φ_{23}) also warrant a corresponding change in the baseline length and elevation angle used for height retrieval. We shall again relate the phase data to the satellites geometry, as depicted in figure 2-5, and seek to obtain the baseline length, B_{avg}, corresponding to the manipulated phase data, Φ_{avg}.

Parallel slant range from each satellite is again approximated and similar triangle concepts are applied to $\triangle$(SAR 1, SAR 3, point 5). To visually aid our understanding of the forthcoming data manipulations, first recognize that $\triangle$(SAR 2, SAR 3, point 4) may be slide down such that vertex 'SAR 2' of this triangle matches with vertex 'SAR 1', as represented by the two shaded triangles in figure 2-5. This means that Φ_{23} can now be considered as an interferogram formed by SAR 1 and a satellite located at point 7 instead, since it is associated with the slant range differences rather than the absolute range distances. The above analysis approach is justified due to the parallel slant range approximation made, where the various satellites in figure 2-5 share the same target-view geometries (i.e. same look angle from the various satellites to a target) so that the absolute positions of satellite pairs become somewhat insignificant in forming interferograms. Rather, only the slant range differences matters.

In the following analysis, we will consider only $\triangle$(SAR 1, SAR 3, point 5), $\triangle$(SAR 1,

SAR 2, point 6) and the shaded triangle containing vertex 'SAR 1'. We first obtain the relationship between the baseline lengths and slant range differences, as shown below.

$$\frac{\Phi_{12}}{B_{12}} = \frac{\Phi_{13}}{B_{13}} = \frac{\Phi_{23}}{B_{23}} \tag{2.14}$$

Similar to eq. 2.1, we next combine the slant range differences, Φ_{ij}, according to

$$\Phi_{avg} = \left(\frac{w_{12}\Phi_{12} + w_{23}\Phi_{23} + w_{13}\Phi_{13}}{w_{12} + w_{23} + w_{13}} \right) \tag{2.15}$$

Extending from eq. 2.14 and with reference to figure 2-5, B_{avg} is defined as

$$\frac{\Phi_{avg}}{B_{avg}} = \frac{\Phi_{13}}{B_{13}} \tag{2.16}$$

$$\begin{aligned} B_{avg} &= \frac{B_{13}}{\Phi_{13}} \cdot \Phi_{avg} \\ &= \frac{w_{12}B_{12} + w_{23}B_{23} + w_{13}B_{13}}{w_{12} + w_{23} + w_{13}} \end{aligned} \tag{2.17}$$

Having obtained Φ_{avg} and its corresponding B_{avg}, the heights may then be retrieved if α and ρ are known. As described in section 2.2.1, α_{new} can be obtained by back solving eq. 1.19 and eq. 1.18 with the GCP. In this collinear configuration case, α_{new} is expected to be $\sim \alpha_{original}$ (i.e. 35°). Using ρ_1, a single set of height, taking into account all three phase data, is attained.

Note that the choice of using ρ_1 in all our height retrieval process is arbitrary. ρ_2 could have been utilized instead and the resulting heights would still be the same. In this case, eq. 1.19 and eq. 1.18 would become

$$\theta'_{12} = \alpha_{12} + \sin^{-1}\left(\frac{\delta_{12}}{B_{12}} - \frac{B_{12}}{2\rho_2} + \frac{\delta_{12}^2}{2B_{12}\rho_2} \right) \tag{2.18}$$

$$\Delta z_{12} = H_{SAR2} - \rho_2 \cos\theta'_{12} \tag{2.19}$$

where H_{SAR2} is the height of SAR 2.

2.2.4 Simulations and Results: Collinear Setup

Eq. 1.12 tells us that the mean RMS retrieved height error is directly proportional to the noise level and inversely proportional to the projected baseline length. In this section, such a relationship will be compared among various height and phase averaging techniques, for a collinear satellite setup. The setup of our simulation is as described in section 1.3.3 with B_{13} as the single longest baseline.

Two Phase Data

Here, we shall look at the relationship between the RMS error and the noise level, and compare this relationship among the following four height retrieval techniques: height inversion based on the single longest baseline, data averaging, single height and single interferogram methods, with weighting function described by eq. 2.3. The simulation results are plotted and tabulated in figure 2-6 and table 2.2 respectively.

As expected from [8], data averaging of the multi-baseline configuration outperforms, in terms of retrieved heights, the approach where only a single baseline is considered, for all noise levels. Phase averaging not only produces lower mean height errors than the single baseline approach, but outperforms data averaging as well. Also, both the single height and single interferogram methods yield the same RMS error up to 60° noise level. This observation is in line with the conclusion of section 2.2.1 where we showed that the two methods represent different approaches in obtaining the same Φ_{new}. However, at higher noise levels, single interferogram method begin to deviate and produces greater errors. This phenomenon is observed in the non-collinear setup as well and will be explained in section 2.2.7.

Weighted Height and Phase Averaging

In this section, all three multi-baseline data are combined and the heights in weighted phase averaging are retrieved as describe in section 2.2.3. The weighting function used for eq. 2.15 and eq. 2.17 is that of eq. 2.24. The performances of the weighted height and phase averaging techniques are compared to the two-satellite averaging techniques examined in the previous section, where weighting function of eq. 2.3 was applied. Simulation results are illustrated in figure 2-7 and table 2.3.

The plot shows that using all available multi-baseline data and averaging them in a non-linear weighted fashion allow heights to be retrieved with smaller mean RMS errors, when compared to using only two of the data. In fact, this was found to be true even when non-linear weights are applied to two phase data such that

$$w_{12} = B_{\perp 12}^2; w_{13} = B_{\perp 13}^2; w_{23} = 0 \tag{2.20}$$

Thus, the ability to utilize all three data in height and phase averaging is certainly advantageous.

From figure 2-7, we see that while two-satellite phase averaging outperforms height averaging, the same cannot be said about the three-satellite averaging case. This may be attributed to the fact that the choice of weights in the former is non-optimal, as highlighted in [8]. Hence, we expect the existence of better methods than simply averaging two sets of heights, such as the phase averaging technique. On the other hand, derivation of the non-linear baseline-dependent weights function in section 2.1.2

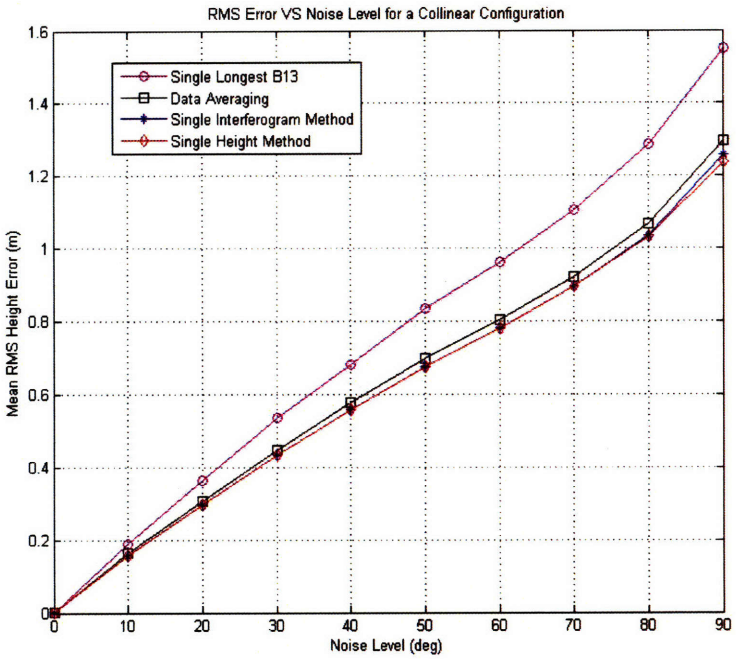

Figure 2-6: Mean RMS height error vs. noise level relationship for data averaging and phase averaging techniques, applied on a three-satellite collinear configuration.

	Mean RMS height error (m)			
Noise Level (°)	**Single Longest Baseline**	**Data Averaging**	**Single Height Method**	**Single Interferogram Method**
0	0.0003	0.0003	0.0003	0.0003
10	0.1908	0.1633	0.1588	0.1588
20	0.3651	0.3073	0.2987	0.2987
30	0.5347	0.4481	0.4353	0.4353
40	0.6817	0.5763	0.5583	0.5583
50	0.8338	0.6974	0.6764	0.6764
60	0.9612	0.8038	0.7794	0.7795
70	1.1056	0.9216	**0.8941**	**0.8945**
80	1.2852	1.0657	**1.0310**	**1.0356**
90	1.5521	1.2974	**1.2376**	**1.2587**

Table 2.2: Mean RMS height error of data averaging and phase averaging, applied on three-satellite collinear configuration.

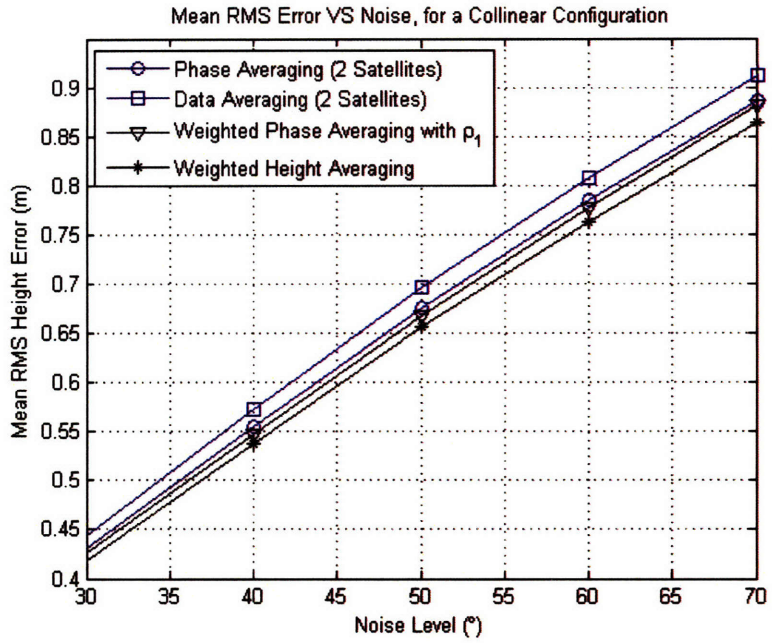

Figure 2-7: Mean RMS height error vs. noise level relationship for two-satellite and three-satellite height and phase averaging techniques, applied on a three-satellite collinear configuration.

	Mean RMS height error (m)			
Noise Level (°)	**Phase Averaging**	**Data Averaging**	**Weighted Phase Averaging**	**Weighted Height Averaging**
0	0.0003	0.0003	0.0004	0.0003
10	0.1575	0.1620	0.1556	0.1535
20	0.2996	0.3088	0.2959	0.2911
30	0.4302	0.4432	0.4259	0.4185
40	0.5547	0.5722	0.5474	0.5381
50	0.6760	0.6971	0.6682	0.6565
60	0.7846	0.8084	0.7764	0.7623
70	0.8872	0.9125	0.8816	0.8638
80	1.0243	1.0555	1.0147	0.9948
90	1.2567	1.2956	1.2434	1.2197

Table 2.3: Mean RMS height error of two-satellite and three-satellite height and phase averaging, applied on three-satellite collinear configuration.

ensures, to a large extent, that the weighted height function of eq. 2.7 is optimal.

Nonetheless, the main advantage of the weighted phase averaging lies in its ability to combine the multi-baseline data into one, such that it may be perceived as coming from only a pair of satellites, allowing the application of the conventional two-satellite height inversion process without need for excessive modifications. In fact, not only is weighted phase averaging shown to work correctly, it outperforms the heights retrieved from individual baseline, as well as from the two-satellite phase and data averaging approaches.

Next, we shall extend the phase averaging concepts to the three-satellite non-collinear configuration.

2.2.5 Three-Satellite Non-Collinear Configuration

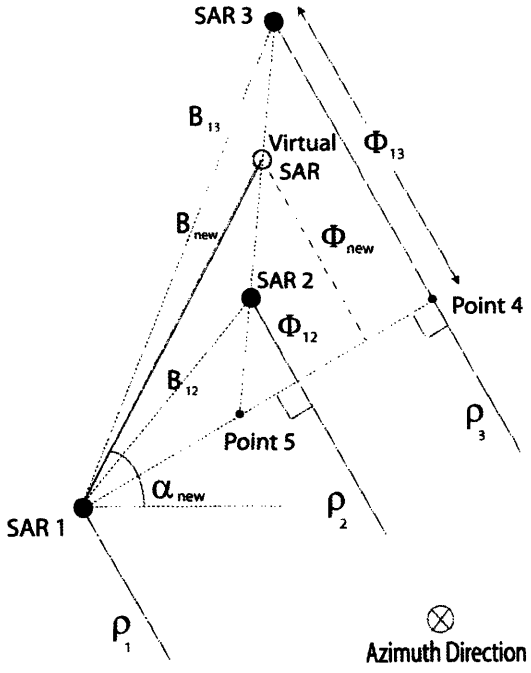

Figure 2-8: Three-satellite non-collinear geometry.

We shall first consider only two of the three interferograms, corresponding to the two longest perpendicular baselines, and later address weighted phase averaging using all three interferograms in section 2.2.6. The phase averaging technique discussed previously shall be extended to the three-satellite non-collinear configuration, using the same argument presented for the single height and single interferogram methods. The geometry of such a setup, with parallel slant range approximation, is shown in figure 2-8. As before, the slant range difference between the satellites may be related to the interferograms.

The multi-baseline interferograms are combined by first selecting the two that corre-

spond to the longest projected baseline lengths. In our case, they are $B_{12}^{\perp}$ and $B_{13}^{\perp}$. These interferograms, after aligned spatially, are processed according to eq. 2.9 or 2.13 to attain Φ_{new}. We shall again relate such modifications made to the phase data to the non-collinear setup geometry.

Referring to figure 2-8, similar triangle concept is applied on the triangle bounded by SAR 3, point 4 and point 5. Using a similar derivation as in eq. 2.10 and 2.11, the coordinates of the virtual SAR's location are attained as

$$[Vitual_X, Virtual_Z] = \left[\frac{SAR\ 2_X + SAR\ 3_X}{2}, \frac{SAR\ 2_Z + SAR\ 3_Z}{2}\right] \tag{2.21}$$

This way, the new baseline length, B_{new}, can be determined since the positions of SAR 1, SAR 2 and SAR 3 are known quantities. Hence, we are able to invert the multi-baseline terrain profiles to obtain a single DEM just by considering SAR 1 and virtual SAR, using Φ_{new}, B_{new}, ρ_1 and α_{new}. In order to account for errors due to similar triangle approximation, B_{new} is estimated from the geometry while α_{new} is attained via use of the GCP. Even so, it should be noted that we are expecting

$$\alpha_{new} \approx \frac{\alpha_{12} + \alpha_{13}}{2} \tag{2.22}$$

2.2.6 Weighted Phase Averaging on Non-Collinear Setup

Figure 2-9(a) illustrates the three-satellite non-collinear geometry for the application of weighted phase averaging. The interferograms Φ_{12}, Φ_{13} and Φ_{23} are combined according to eq. 2.24 and eq. 2.15 to arrive at a single Φ_{avg}. As before, we seek to find the corresponding B_{avg} that may be applied to eq. 1.18 and eq. 1.19 for height retrieval, while α_{new} is attain using the GCP.

B_{avg} is derived with similar triangle concepts applied to $\triangle$(SAR 3, point 5, point 8). Adopting the same argument as presented in section 2.2.3, we may consider $\triangle$(point 6, point 8, point 9) instead of $\triangle$(SAR 2, SAR 3, point 4) due to parallel slant range approximations made. Before arriving at B_{avg}, the baseline lengths corresponding to slant range differences Φ_{12}, Φ_{13} and Φ_{23}, projected on line segment (point 8, SAR 3) of $\triangle$(SAR 3, point 5, point 8) have to be attained. These virtual baselines are labeled as B_A, B_B and B_C in figure 2-9(b). A B_{temp} is defined to be the distance between point 8 and SAR_{avg} such that

$$B_{temp} = \frac{w_A B_A + w_B B_B + w_C B_C}{w_A + w_B + w_C} \tag{2.23}$$

where

$$w_A = B_{\perp A}^2; w_B = B_{\perp B}^2; w_C = B_{\perp C}^2 \tag{2.24}$$

Knowing B_{temp}, the position of SAR_{avg} as well as B_{avg} can be deduced. Figure 2-9(a)

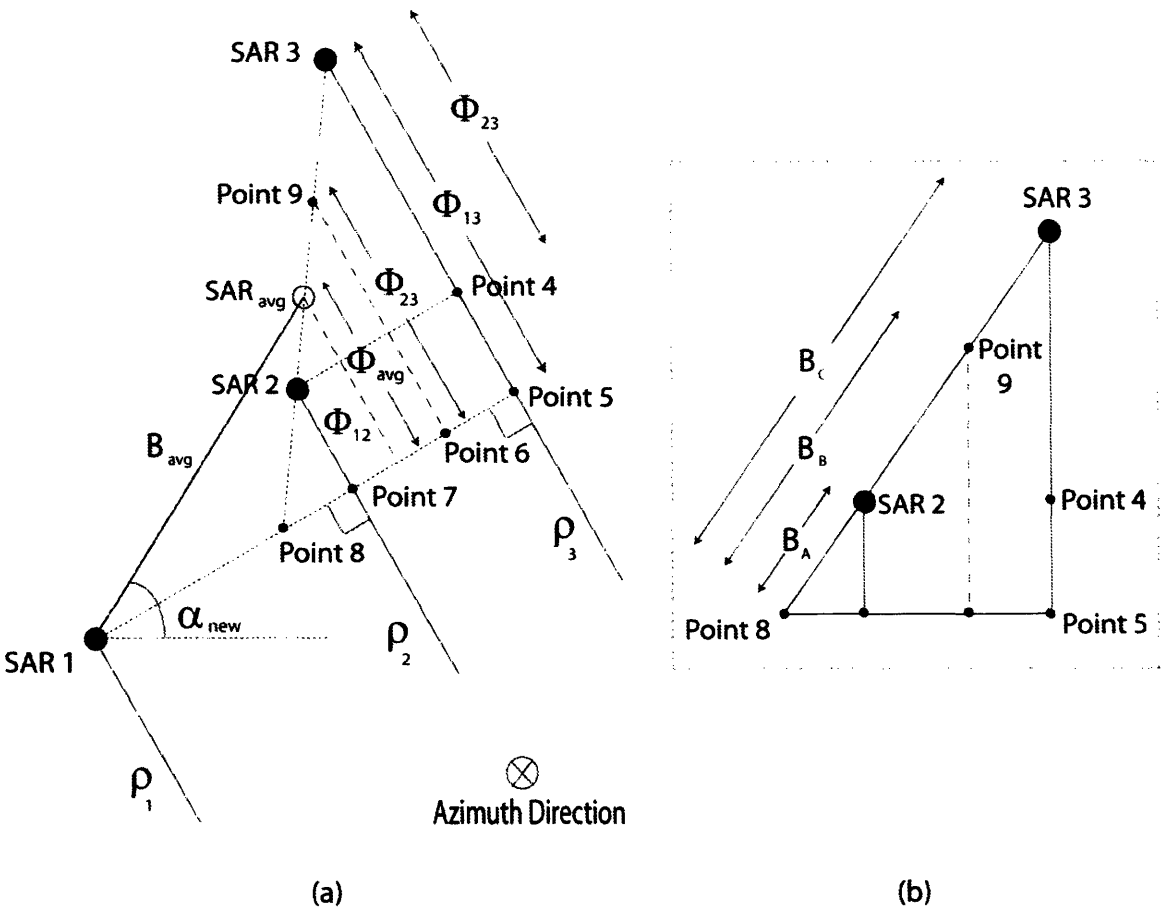

Figure 2-9: (a) Three-satellite non-collinear geometry for weighted phase averaging (b) Application of similar triangle concepts on $\triangle$(SAR 3, point 5, point 8).

illustrates these parameters. Final terrain heights, using the combined multi-baseline data, can then be retrieved with B_{avg}, Φ_{avg}, ρ_1 and α_{new}.

In the above analysis, the position of point 8 has to be first attained so that B_A, B_B and B_C, and eventually B_{avg} can be found. This is achieved by applying simple geometry and making use of ρ_1 slant range distance and a GCP located in pixel $(1,1)$. However, this *approximated* point 8's position is not fixed. As we consider data further away from pixel (1,1) in the ground range direction, $\triangle$(SAR 3, point 5, point 8) alters. Visually, we can think of an increment of the look angle such that the parallel slant range direction shifts, resulting in a corresponding change in point 8. Simulation results show that this inability to accurately deduce point 8's position for all pixels in the interferogram leads to heights retrieved with unacceptable magnitude of errors, when weighted phase averaging is applied to the non-collinear three-satellite configuration.

We will next examine the performance of phase averaging technique on the non-collinear satellite setup. Weighted phase averaging will no longer be considered since

errors are introduced upon the approximations made, as described in the previous paragraph.

2.2.7 Simulations and Results: Non-Collinear Setup

In this section, application of weighted phase averaging will not be considered. In phase averaging, the original three-satellite configuration is collapsed into two satellites using a virtual SAR (see figure 2-8) which is obtained by manipulating the interferograms. In our simulation, an additional real satellite is physically added to the exact position of virtual SAR to illuminate the scene and record the phase data. As such, an additional physical baseline exist between SAR 1 and this real SAR, and shall be called *physical baseline*. By doing so, we would like to investigate the improvements in height retrieval brought about by the three-satellite data over a two-satellite setup, even though both cases may be perceived as having two satellites at the same locations. The results for the non-collinear setup are plotted and tabulated in figure 2-10 and table 2.5 respectively.

Simulation results show that phase averaging again outperforms both the heights retrieved from the single longest baseline and data averaging. In fact, it also did much better than retrieving heights with the physical baseline. This implies that having data from an additional third satellite is favorable for increased accuracies of the DEM. Again, as in the collinear configuration, we are now able to combine the multi-baseline data into one such that the conventional two-satellite height inversion process may be applied, and yet returns more accurate results than just using data from each of the three possible satellite pairs.

	Number of Residues		
	Single Height Method		**Single Interferogram Method**
Noise Level (°)	ϕ_{12}	ϕ_{13}	$\phi_{12} + \phi_{13}$
70	0	0	8
80	1	2	36
90	4	24	268

Table 2.4: Number of residues in 256 × 256 phase data prior to unwrapping.

As in the collinear configuration simulations, single interferogram method performs the same as single height method for noise levels up to 60°. Beyond that, its performance starts to deteriorates. The deviation between the two phase averaging approaches may be explained in terms of residues in the phase data prior to residue-weighted least-squares unwrapping. In single height method, ϕ_{12} and ϕ_{13} are unwrapped individually while in single interferogram method, $\phi_{12} + \phi_{13}$ is unwrapped instead. Table 2.4 shows the number of residues in the 256 × 256 denoised wrapped phase data used in both of the phase averaging methods. Below 70° noise level, no

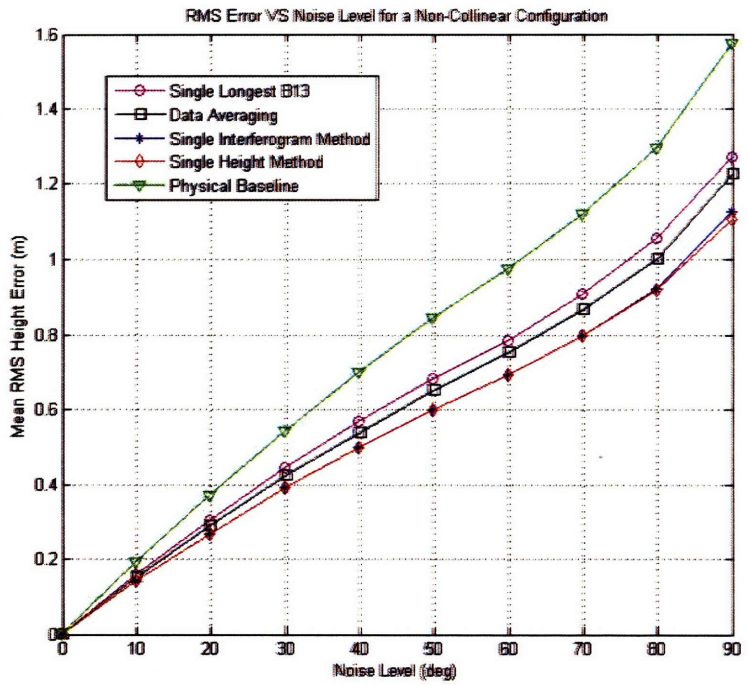

Figure 2-10: Mean RMS height error vs. noise level relationship for data averaging and phase averaging techniques, applied on a three-satellite non-collinear configuration.

	Mean RMS height error (m)				
Noise Level (°)	**Single Longest Baseline**	**Data Averaging**	**Single Height Method**	**Single Interferogram Method**	**Physical Baseline**
0	0.0004	0.0003	0.0005	0.0005	0.0003
10	0.1600	0.1542	0.1431	0.1431	0.1936
20	0.3035	0.2898	0.2680	0.2680	0.3711
30	0.4470	0.4251	0.3927	0.3927	0.5417
40	0.5704	0.5401	0.4991	0.4991	0.6997
50	0.6825	0.6537	0.6010	0.6010	0.8457
60	0.7860	0.7550	0.6931	0.6931	0.9755
70	0.9084	0.8678	**0.7971**	**0.7977**	1.1198
80	1.0579	1.0020	**0.9182**	**0.9228**	1.2963
90	1.2728	1.2294	**1.1073**	**1.1262**	1.5743

Table 2.5: Mean RMS height error of data averaging and phase averaging, applied on three-satellite non-collinear configuration.

phase inconsistencies are detected in all three interferograms. In single interferogram method, summing up the phase data before unwrapping act to amplify the effects of noises, resulting in greater number of residues as compared to each separate interferogram. These phase inconsistencies are accounted for in the weighting schemes of the least-squares unwrap and is the cause for deviations between the methods, even though they both seek to attain the same unwrapped Φ_{new}. Hence, depending on the effectiveness of the selected phase denoising scheme, single interferogram method will eventually breakdown as the noise level increases.

In the next section, slope-biasing effects of CDD as well as the solutions will be studied.

2.3 Multi-baseline CCD

In this section, a problem inherent in current coherent change detection techniques shall first be analyzed. A solution based in the wavelet domain [4] is then implemented and compared with another solution which uses the scene's DEM. The latter requires a multi-baseline satellite configuration in order to avoid temporal decorrelation in the retrieved heights.

2.3.1 Coherence Losses and Terrain Slopes

[17] concluded that multilook coherence estimates (eq. 1.21) of the surface in undulating terrain appear to vary if different interferometric baseline is used. In particular, shallow slopes exhibit high coherence whereas steeper slopes exhibit low coherence. We shall first examine this relationship in our implementation and then discuss its implication in CCD.

Unlike in the height retrieval process, the SAR images are processed separately before combining them to compute their coherence values, as in eq. 1.21. Interferometric flat earth phase progression, similar to that described in section 1.4.3, is first removed from each image [12, 39]. The two images are then spatially aligned before the multilook coherence estimator is applied. Misregistration errors contributes to coherence losses and may be factored into ρ_{themal} of eq. 1.22. Note also that phase denoising is no longer applied here.

In the following simulations, we seek to explore the effects of varying baseline length between satellite passes to the multilook coherence values of eq. 1.21. As well, the impacts of different terrain slope on this relationship are looked into. Our setup is similar to the two-satellite case of section 1.3.3 where α remains at 35°, except that the baseline length between the satellites are no longer fixed, but rather made to vary from $0m$ to $1080m$, at increments of $40m$. Here, the two satellites are used to represent two passes of a single satellite at different times in near-repeat orbital tracks separated by the baseline, B, as depicted in figure 2-11. The illuminated ter-

rain remains totally unchanged between the passes and no noise is present such that $\rho_{temporal}$ and $\rho_{thermal}$ both equal one. Eq. 1.22 becomes

$$\rho_{total} = \rho_{spatial} \tag{2.25}$$

Thus, we are really measuring spatial baseline correlation in the coherence values. Ideally, we would always like to be able to relate the ρ_{total} computed to $\rho_{temporal}$ in order to measure the scene change.

Plots of the coherence between the two SAR images against baseline length are shown in figure 2-11 for (a) a flat ground terrain, (b) for a terrain with a 11° slope facing the radars and (c) for one with a 27° slope. Since we are dealing with a 256×256 terrain size, the corresponding coherence map attained is also 256×256 in size. In making the plots, the coherence value of the middle $(128, 128)$ pixel is used. As stated earlier, a satellite in an exact repeat orbit, i.e. $B = 0$, has $\rho_{spatial} = 1$ as observed for all the three terrains. In figure 2-11(a) $\rho_{spatial}$ for flat terrain are well accounted for due to the flat earth phase correction made to each of the two images, resulting in $\rho_{total} = \rho_{spatial} = 1$. This high coherence allows us to correctly relate ρ_{total} to scene changes (no change). As the terrain slope is increased to 11° in (b), coherence values ρ_{total} begin decreasing as the baseline length is increased, even though the terrain scene remains unchanged. This is due to deterioration of $\rho_{spatial}$. At an even greater terrain slope of 27°, figure 2-11(c) predicts that the coherence of the two scenes decays at a faster rate. These observations agree well with the conclusions of [17] presented at the beginning of this section.

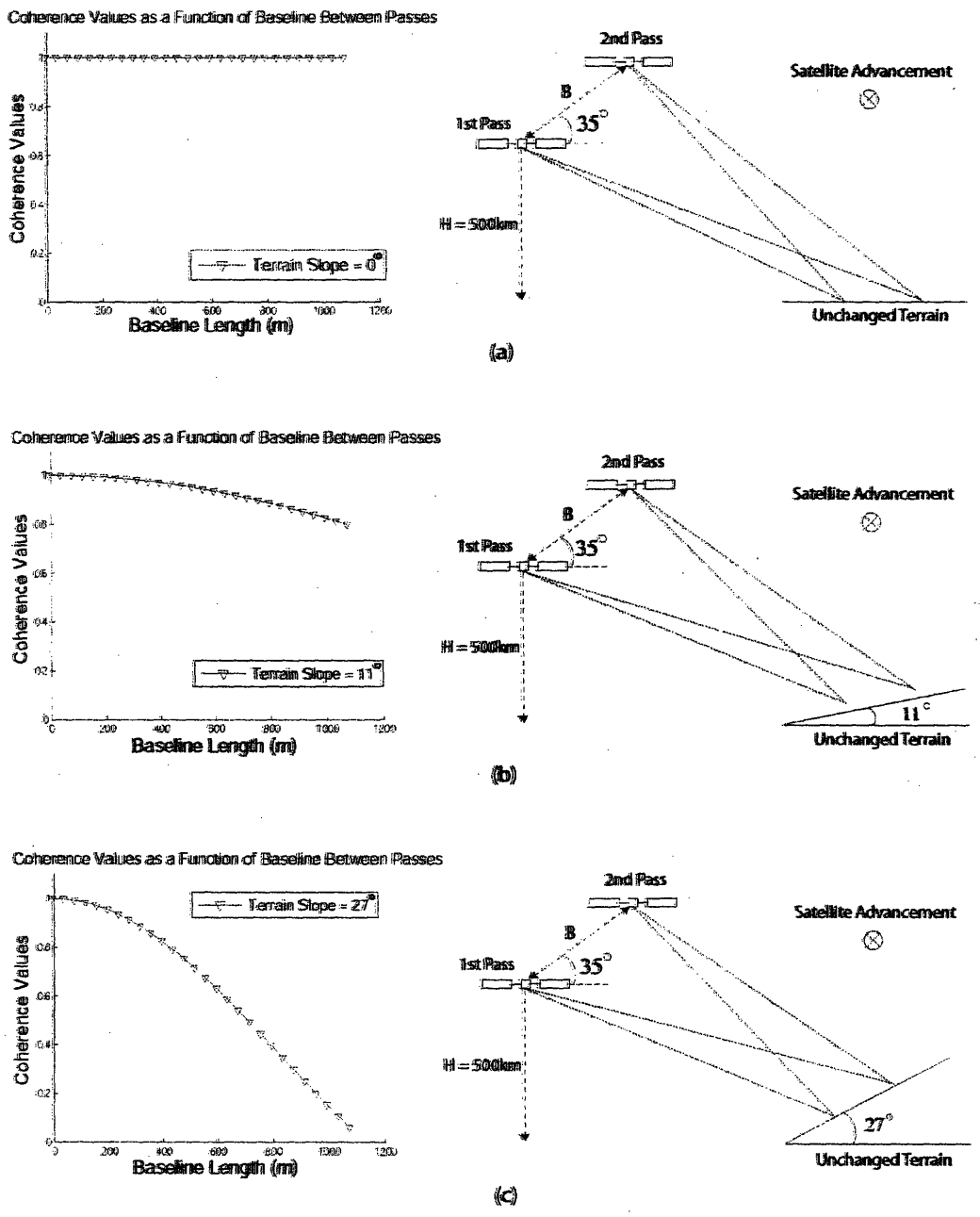

Figure 2-11: Coherence values as a function of baseline length, B, between satellite passes on unchanged terrain with slopes (a) 0°, (b) 11° and (c) 27°.

2.3.2 CCD and Terrain Slopes

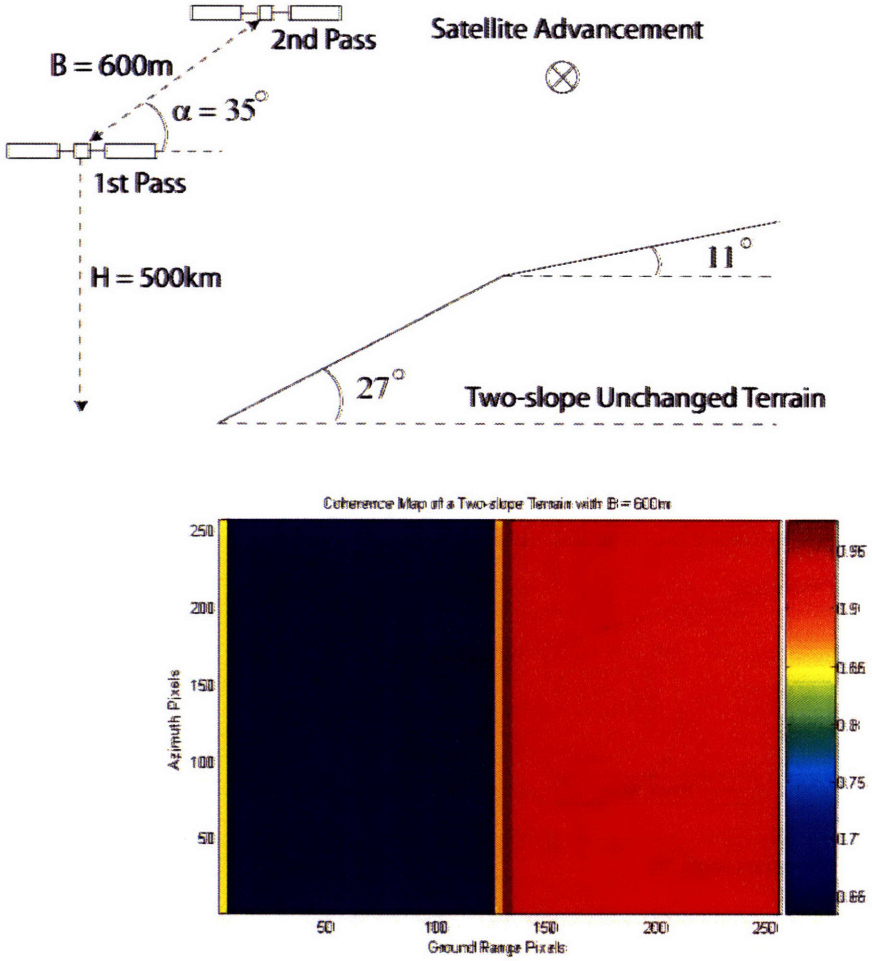

Figure 2-12: Two-slope unchanged terrain and its corresponding coherence map, in a noiseless environment.

Some form of thresholding is usually applied in CCD [13, 38]. In its simplest form, pixels with coherence values below the threshold are classified as "change present" while those above the threshold are classified as "change absent". In dealing with *constant-slope* terrain as above, care must be taken to ensure that the interferometric baseline is small enough so that $\rho_{spatial} \neq 0$. Although coherence losses occur even when the constant-slope terrain stays unchanged, these losses, for a given baseline, are constant and may be accounted for by choosing an appropriate value of the threshold. However, if the scene contains terrain of varying slopes, as in mountainous regions, then $\rho_{spatial}$ will vary drastically across the map for a particular B and it becomes impossible to set a threshold without a prior knowledge of the DEM, since we can no longer identify which coherence losses are a result of spatial baseline decorrelation and which are due to actual scene changes. In these cases, it would be desirable to have a short baseline as simulation results in figure 2-11 shows that the coherence values for unchanged scenes remain high for varying terrain slope when $B < 400m$.

Figure 2-12 presents one such case, with $B = 600m$, where an unchanged two-slope terrain returns two coherence values, making it hard to distinguish if the coherence losses are due to large spatial baseline or actual scene alterations.

2.3.3 Multi-baseline Considerations

Similar observations due to the large variation in the terrain's slopes are made in [14, 41]. Suggestions by [14] to remove the contributions due to $\rho_{spatial}$ in calculating ρ_{total} include having a detailed knowledge of the true DEM. This approach, when applied on a one-satellite repeat-track scenario, is limited by the fact that the retrieved DEM is susceptible to temporal decorrelation. If two or more satellites are available simultaneously, as in the interferometric cartwheel, then, temporal correlation becomes high and a more accurate DEM is attained. In section 2.3.5, we shall look into the case where three satellites are available for height retrieval and the resulting topography is factored into the coherence analysis so that eq. 1.21 becomes [4]

$$|\rho_{topo}| = \frac{\left|\sum_{m=1}^{M}\sum_{n=1}^{N} S_1(m,n)S_2^*(m,n)e^{-j\hat{\phi}_x(m,n)}\right|}{\sqrt{\sum_{m=1}^{M}\sum_{n=1}^{N}|S_1(m,n)|^2 \sum_{m=1}^{M}\sum_{n=1}^{N}|S_2(m,n)|^2}} \tag{2.26}$$

where $\hat{\phi}_x$ is the estimated topographic component obtained by means of external DEMs. Eq. 2.26 shall be referred to as the *topography-corrected coherence estimator.* This coherence value is not biased by the terrain slopes anymore and works best if a multi-baseline satellite configuration is available for DEM retrieval. However, an external DEM may not always be available and considerations of terrain profiles in CCD greatly increase the computational complexities.

In [4, 5], a method that uses the two-dimensional discrete wavelet packet transform (2D-DWPT) to retrieve the coherence map is presented, and unlike the multilook method, is shown to be unbias to the terrain's topography even without any knowledge of the DEM. This approach also allows a higher spatial resolution coherence estimation since no windowing is applied.

2.3.4 Wavelet Transform-Based Interferometric Coherence Estimator

According to [5], the measured interferometric phase, ϕ, may be described by

$$\phi = \phi_x + v \tag{2.27}$$

where v is a zero-mean noise independent of ϕ_x, which represents the topographic induced phase. It should be recognized that ϕ here is the same as the ϕ_{12} of eq. 1.3,

which we have been using in the height retrieval process. By considering the complex phasor, $e^{j\phi}$, an average wavelet coefficient intensity may be derived as

$$E\{|\mathrm{DWT}_{2D}e^{j\phi}|^2\} = 2^{2i}N_c^2 + \sigma_{v_c^w}^2 + \sigma_{v_s^w}^2 \tag{2.28}$$

where i represents the wavelet scale, v_c and v_s are two zero-mean noises associated with the real and imaginary parts of $e^{j\phi}$ respectively, and $\sigma_{v_c^w}^2$, $\sigma_{v_s^w}^2$, are the variance values of the noise terms in wavelet domain. Nc contains the same information as the original coherence nonbiased by terrain slope variations since topography information is already encompassed in ϕ [4]. So, if N_c has a high value, the corresponding phase contains information about the topography, and if its zero, then the phase contains only noise. Also, unlike in the multilook techniques, images S_1 and S_2 need not be considered separately. Thus, the same processing of the combined data in height retrieval applies here as well.

Eq. 2.28 shows that N_c, hence, the coherence information, can be retrieved by selecting a large i so that influence of the noise terms become negligible and the wavelet coefficients' intensity is only proportional to coherence. i is selected to be $i_{max} = 3$ in our implementation since that is shown to be sufficient for the decoupling of N_c from the random noise terms, by 2D-DWPT. Daubechies filters are used in our implementation of the coherence estimation process, which closely follows the algorithm presented in [5]. It should be noted that the selection of threshold values in the algorithm is non-automated. The final effect of the process is that the weight of those wavelet coefficients classified as containing useful information are amplified with respect to those not processed, reducing the influence of the noise terms with respect to N_c. After the inverse 2D-DWPT is applied to the processed signal, the derived complex phasor output in the original domain, $N_c e^{j\phi_x}$,has a denoised topographic phase and an amplitude proportional to N_c. The coherence value is obtained by normalizing the amplitude by $2^{i_{max}}$.

In short, the algorithm first convert the input, $e^{j\phi}$, into the two-dimensional frequency-space wavelet domain, do some processing to enhance the useful signals inside that domain, and returns the output, $N_c e^{j\phi_x}$, in the original domain. By applying 2D-DWPT to the entire image rather than employing a windowing process as done in multilook techniques, spatial resolution is maintained. Furthermore, noise wavelet coefficients of interferometric phases with low coherence, which may contain phase details, are not eliminated. Instead, the algorithm is based on enhancing the importance of useful wavelet signal coefficients. In this way, spatial details are also maintained. We shall verify our implementation using the denoised topographic phase of the algorithm's output, ϕ_x. Ultimately, our interest is in the algorithm's ability in retrieving the nonbiased coherence map without the use of a DEM.

In this investigation, the three-satellite non-collinear setup of section 1.3 is used. Phase averaging method presented in earlier sections is applied for the height retrieval process, and three different denoising schemes (see section 1.4.2) are adopted and com-

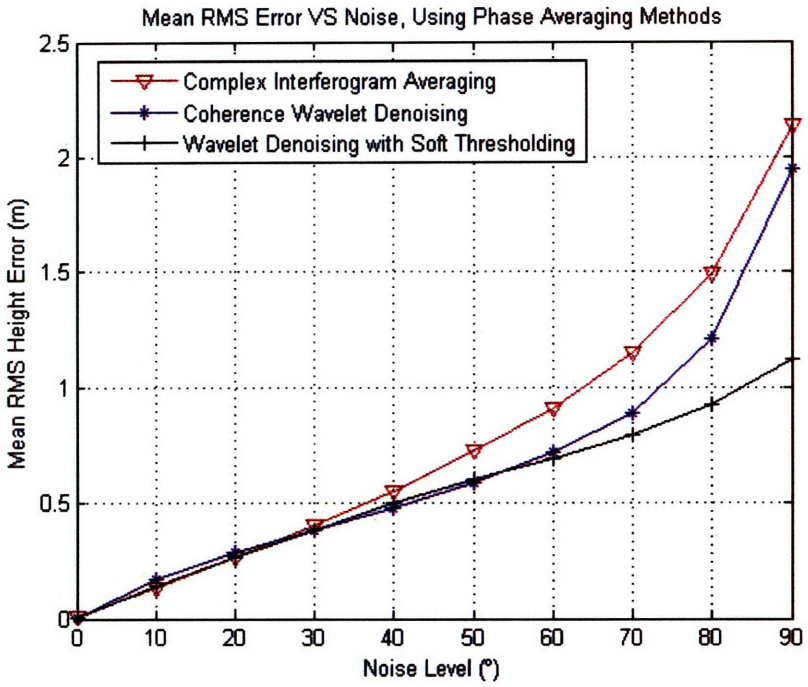

Figure 2-13: Mean RMS height error of phase averaging method as a function of noise, with complex interferogram averaging, coherence wavelet denoising and wavelet denoising with soft thresholding.

	Mean RMS height error of Phase Averaging Method (m)		
Noise Level (°)	**Complex Averaging**	**Coherence Wavelet Denoising**	**Wavelet Denoising Soft Thresholding**
0	0.0116	0.0003	0.0005
10	0.1324	0.1736	0.1409
20	0.2649	0.2871	0.2689
30	0.4071	0.3823	0.3853
40	0.5545	0.4823	0.5005
50	0.7241	0.5901	0.6052
60	0.9137	0.7193	0.6940
70	1.1526	0.8880	0.7911
80	1.4955	1.2085	0.9221
90	2.1350	1.9466	1.1228

Table 2.6: Mean RMS height error of phase averaging method, with different denoising schemes applied.

pared: complex interferogram averaging, wavelet denoising with soft-thresholding, and denoising using the current method which we refer to as *coherence wavelet denoising*. In figure 1-6, it was already shown that both complex interferogram averaging and soft-thresholding wavelet denoising outperforms the case with no denoising at all noise levels. In the plot of figure 2-13, mean RMS error using the three denoising schemes are comparable for low noise levels, i.e. $< 30°$. As the noise level increases, coherence wavelet denoising did even better than complex interferogram averaging while soft-thresholding wavelet denoising outperforms the other two eventually. Hence, the topographic phase, ϕ_x, of the complex phasor output is indeed a denoised version of the original phase data, as indicated in [4, 5]. To a certain extend, this verifies our implementation of the algorithm.

It is interesting to note that even though wavelet denoising with soft-thresholding generally fair better than coherence wavelet denoising, and that its threshold selection process is automated, coherence values may not be retrieved from this approach. This is because in soft-thresholding, some complex wavelet coefficients are eliminated, preventing a correct reconstruction of the complex output, $N_c e^{j\phi_x}$.

2.3.5 Compensating for Slope Biasing Effects in CCD

The wavelet transform-based coherence estimator is next applied on the same terrain we had in figure 2-12, except that scene changes do occur between the satellite passes. Figure 2-14(b) depict this scene change. Compared to the first pass, the two-slope terrain in the second pass has a $4.5cm$ deep, one-pixel wide trench running along the azimuth direction in the steeper sloped portion and a $4.5cm$ deep, four-pixel big hole entrenched in the middle of the gentler sloped portion. In the ideal case, we would hope that the resulting coherence map indicates high coherence values across the entire scene except where the trench and hole deformation occur. Figure 2-14(c) shows the ideal coherence map where the resolutions of the deformations are exact. This map shall be used as the basis of comparison in the computation of the mean RMS coherence error, which can be attained in a similar fashion as eq. 1.9 and 1.10, with the exception that the heights are replaced by the coherence values.

It was already shown that multilook coherence estimator suffers from varying coherence losses dependent on the terrain slope, even for an unchanged scene. Here, applications of the topography-corrected and wavelet transform-based CCD techniques will be applied, and comparisons be made among these three approaches of detecting changes. To facilitate the above, the setup illustrated in 2-14(a) is used. It consist of the non-collinear three-satellite configuration of section 1.3.3, at two different times, separated by a baseline of $600m$ between the passes. This baseline length, as observed in figure 2-12, is sufficient to induce slope-dependent coherence losses in the multilook estimator. Only SAR 1 of both passes are utilized in retrieving coherence values from the three CCD techniques. However, all three satellites of the first pass are involved in retrieval of the original topographic phase term, without the need for temporal degradation considerations, in applying eq. 2.26. The three-satellite height retrieval

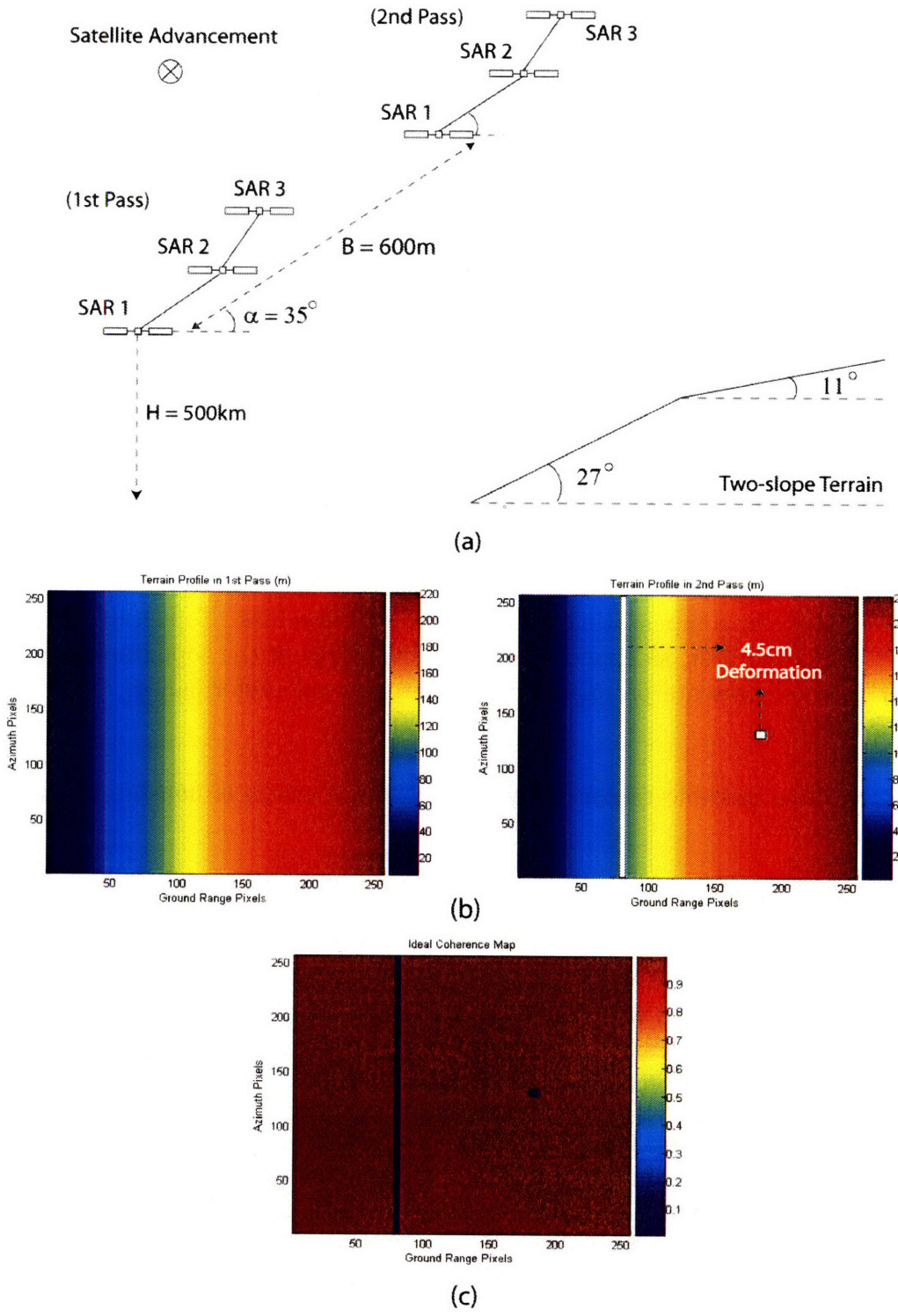

Figure 2-14: (a) Satellite configuration for coherence mapping with multilook, wavelet transform-based and topo-corrected coherence estimator (b) The terrain profile in the 1st and 2nd satellite pass (c) Ideal coherence map for the observed scene change in (b).

technique adopted for this case is phase averaging, with coherence wavelet denoising discussed in section 2.3.4 applied. Note that both the height and coherence retrieval processes are susceptible to the same noise level.

In this investigation, we vary $\rho_{temporal}$–scene change, $\rho_{spatial}$–varying terrain slopes and $\rho_{thermal}$–noises, and seek to achieve the following:

- Detect the actual scene changes, i.e. $4.5cm$ deep trench and hole
- Investigate slope bias effects on the various CCD techniques
- Examine the coherence map errors in the presence of noise
- Look at the coherence map spatial resolution of the various CCD techniques

Figure 2-15 shows a plot of the mean RMS coherence error as a function of noise level using the multilook, topography-corrected and wavelet transform-based coherence estimator. The corresponding values are tabulated in table 2.7. In general, the RMS coherence error increases with the noise level. Topography-corrected and wavelet CCD techniques significant outperforms the multilook approach, primarily due to the latter's inability in compensating for the terrain's slope bias. Topography-corrected method works the best, as expected, having knowledge of the topography while the wavelet method presents promising coherence retrieval performances even without use of a DEM.

There are three possible reasons why the coherence errors is non-zero in noiseless environments.

1. Due to the slope bias effects, as discussed in section 2.3.2, that occur even when no noise is present.
2. The ideal map used has an absolute value of 1 when no change occurs while total decorrelation (i.e. 0) when a change is detected. However, in our implementation and practical cases, no detected changes corresponds to high coherence values, > 0.7, while scene changes lead to low values of > 0.3.
3. Ideal coherence map has spatial resolution exact to the actual terrain changes, i.e. 0 values occupying regions exactly as the one-pixel wide trench and four-pixel size hole. In implementation, lower resolution may be obtained depending on the CCD technique applied.

From the above, it becomes necessary to visually observe the coherence map of the three different approaches so as to better understand each implication on spatial resolution, bias slope effects, scene change detection and errors due to noise. Figure 2-16 to 2-18 depicts the coherence maps for a single simulation trial run with noise level 0°, 10°, 20°, 30°, 40° and 50°.

From figure 2-16(a), in the noiseless case, multilook CCD with a baseline of $600m$

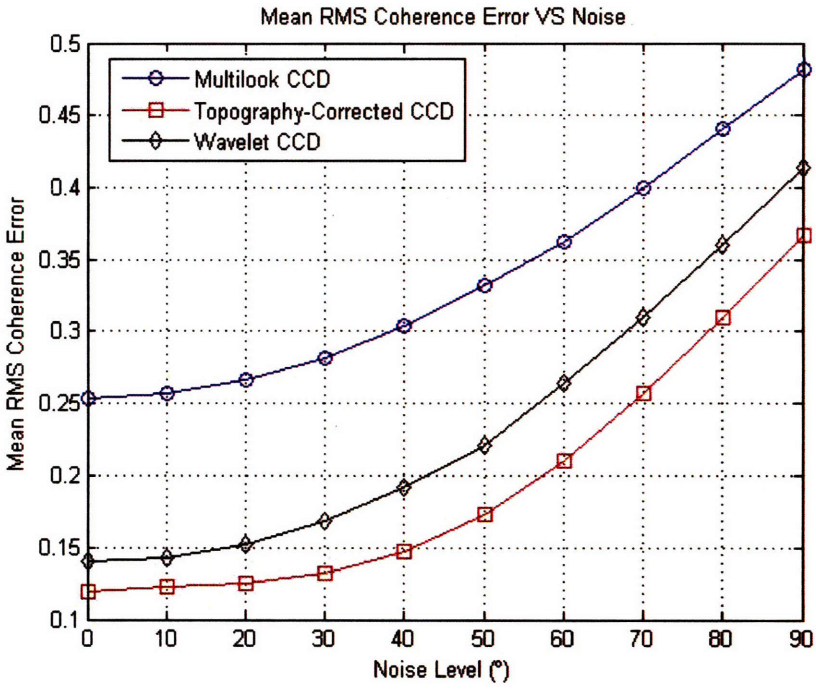

Figure 2-15: Mean RMS coherence error as a function of noise for multilook, topography-corrected and wavelet CCD.

	Mean RMS coherence error		
Noise Level (°)	**Multilook CCD**	**Wavelet CCD**	**Topography-Corrected CCD**
0	0.2538	0.1400	0.1194
10	0.2570	0.1428	0.1231
20	0.2665	0.1522	0.1252
30	0.2824	0.1679	0.1320
40	0.3040	0.1913	0.1475
50	0.3317	0.2207	0.1733
60	0.3630	0.2644	0.2108
70	0.4005	0.3100	0.2570
80	0.4408	0.3603	0.3096
90	0.4814	0.4136	0.3673

Table 2.7: Mean RMS coherence error for various CCD techniques on a non-collinear three-satellite near-repeat orbit setup.

is corrupted by the unchanged terrain slopes such that coherence value remains high for the gentler slope but medium for the steeper one. Due to windowing, the spatial resolution is also worse-off than the ideal's. Wavelet CCD, though affected by the slopes, still register a high coherence > 0.8 for the entire map except where deformation occurs. Spatial resolution of the detected changed regions is high, as predicted. Accounting for the slopes via knowledge of the DEM, topography-corrected CCD is seen to be non slope-biased. Again, because of windowing involve in such a coherence estimator, it loses spatial resolution when compared to the ideal or wavelet CCD map. As the noise level increase, both the topology-corrected and wavelet approach, as seen in figure 2-18(b), still depicts the correct information, i.e. there is no change detected throughout the map except for the trench and hole regions. However, multilook CCD breaks down and it is impossible to tell if the coherence losses in the left half portion of the map are due to temporal or spatial decorrelation.

In this chapter, phase averaging technique has been successfully applied to the three-satellite non-collinear configuration and is shown to perform better than data averaging, in terms of the mean RMS height error. Weighted phase averaging technique, though expected to outperform phase averaging using only two satellite data, break down in the non-collinear setup. As well, the single height method is shown to be more robust to varying noise levels than the single interferogram method. The ability to combine the multi-baseline data into one, such that it may be perceived as coming from only a pair of satellites, allows the application of the conventional two-satellite height inversion process without need for excessive modifications. Yet, at the same time, this approach returns more accurate results than just using data from each of the three possible satellite pairs.

As well, coherence losses due to terrain slopes and inexact satellite repeat tracks are identified. This introduces ambiguities in the interpretations of low or medium coherence values: if they represent a scene change or simply an undulating terrain. Solutions to this issue include accounting for the topographic phase variations via prior knowledge of the DEM or a distinctive approach in the wavelet domain. While the latter is shown to produce a map with higher spatial resolutions, the former returns the best overall performance in CCD, in terms of mean RMS coherence error, and requires a multi-baseline satellite configuration for accurate retrieval of the DEM.

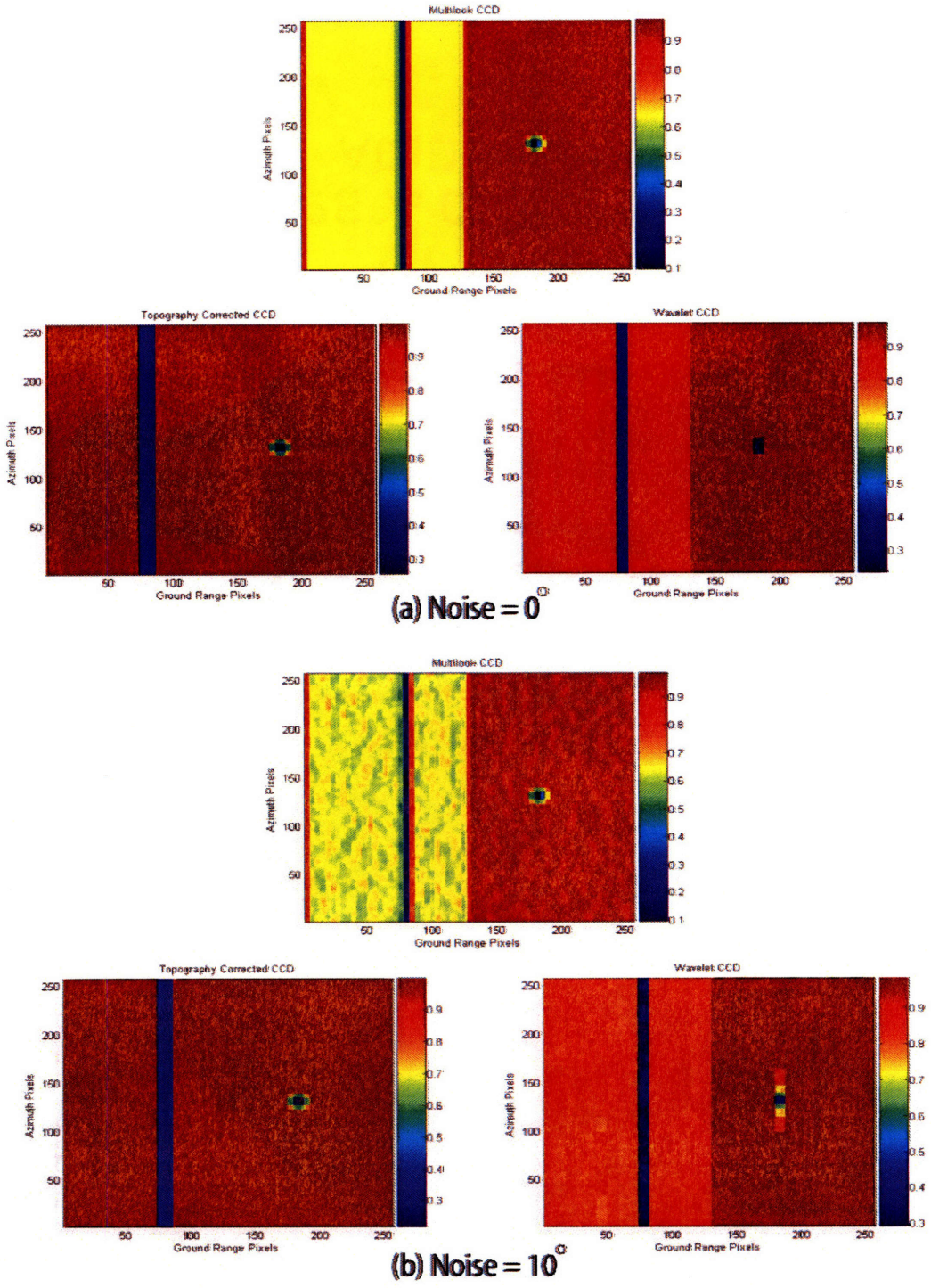

Figure 2-16: Coherence map for one simulation trial using multilook, topography-corrected and wavelet CCD with noise level at (a) 0° (b) 10°.

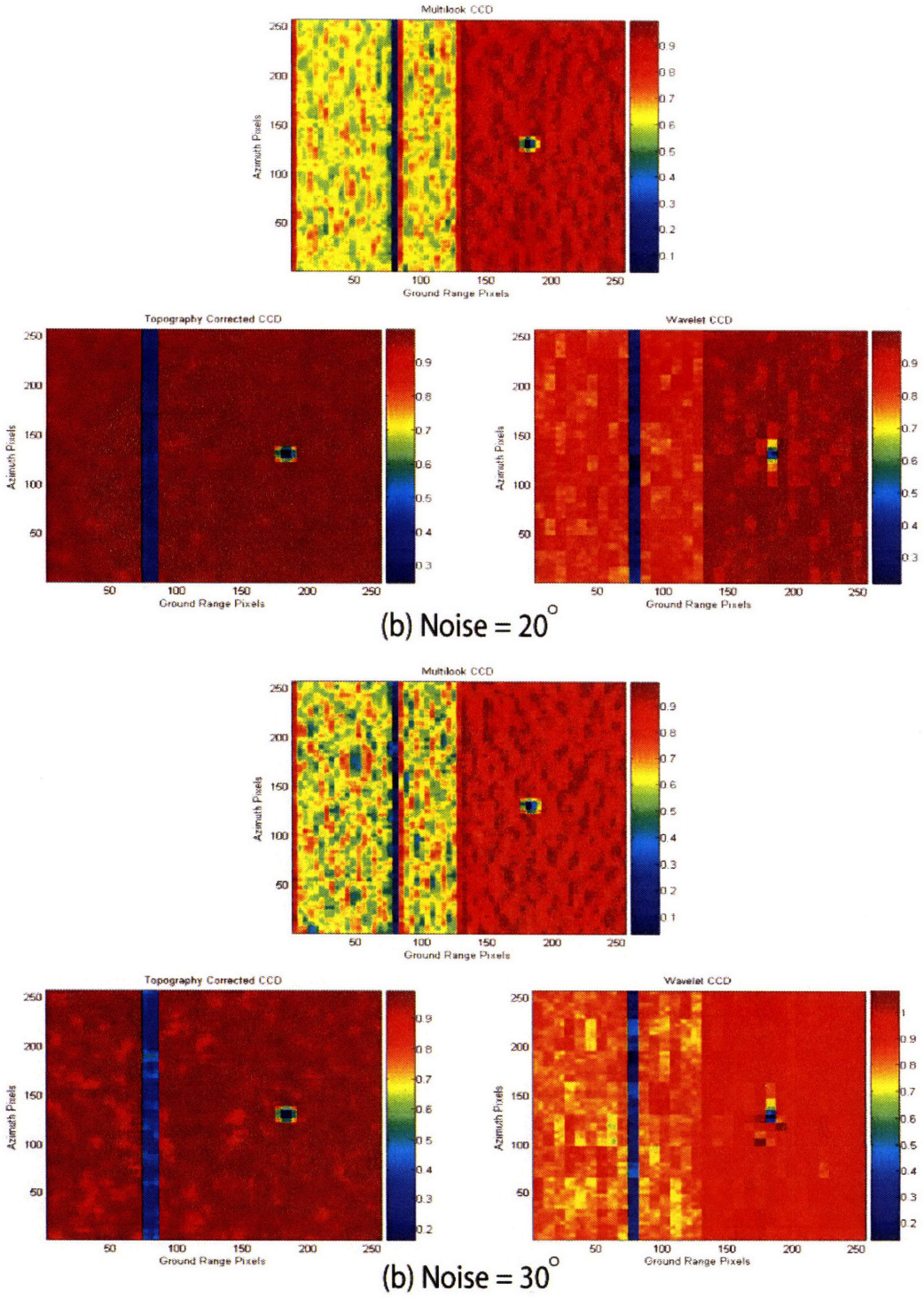

Figure 2-17: Coherence map for one simulation trial using multilook, topography-corrected and wavelet CCD with noise level at (a) 20° (b) 30°.

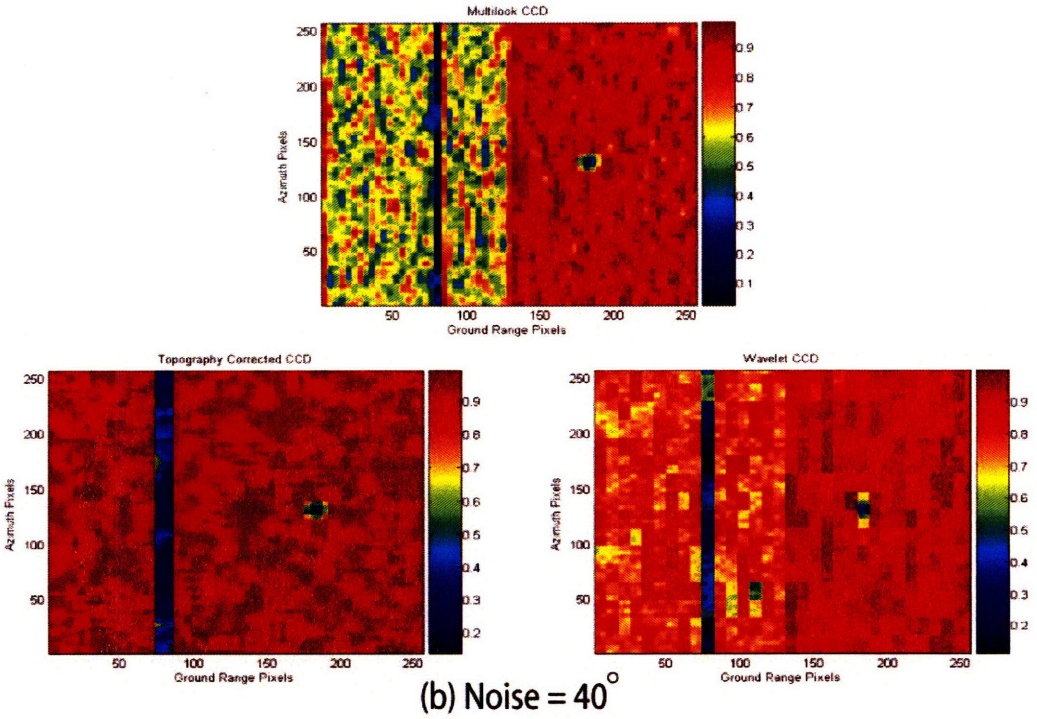

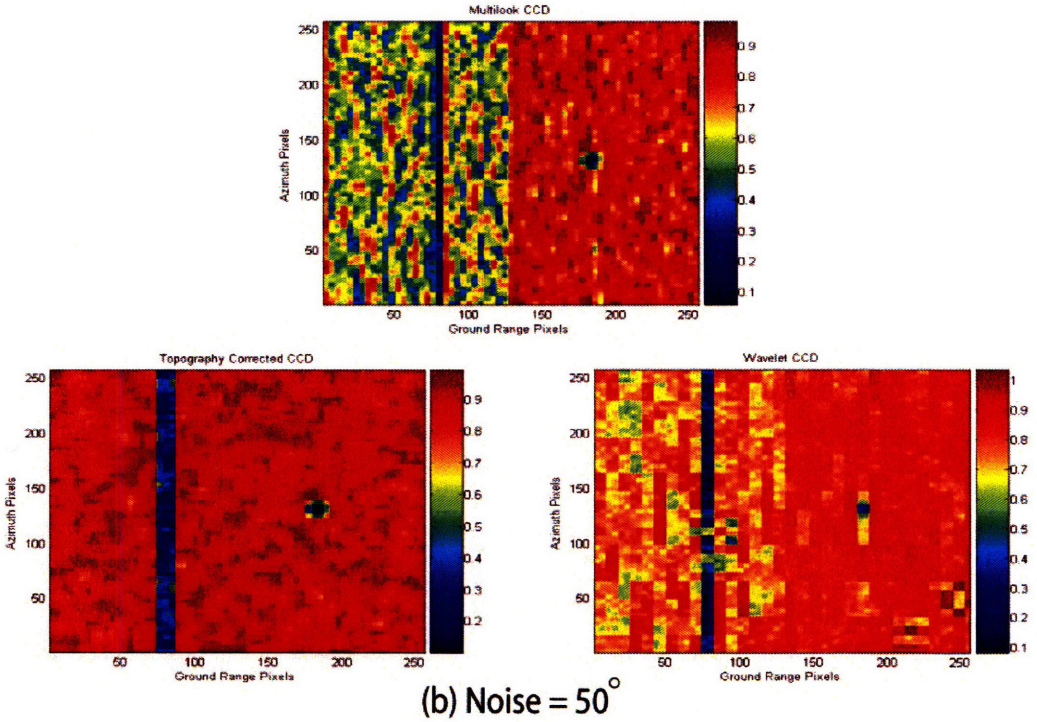

Figure 2-18: Coherence map for one simulation trial using multilook, topography-corrected and wavelet CCD with noise level at (a) 40° (b) 50°.

Chapter 3

Three-Satellite Interferometric Cartwheel Orbit

Interferometric cartwheel system is one of the more recent applications of InSAR. The constellation is composed of at least three satellites, which are assume to be active in our analysis. Such a configuration is capable of acquiring the data required for a more accurate computation of the DEM, since the simultaneous reception of interferometric echoes on these satellites will avoid the temporal decorrelation effects inherent to repeat-pass interferometry [6]. Each satellite orbit is characterized by different eccentricities and perigee arguments so that the relative motion of the satellites, in general, follows an ellipse. As such, the constellation can constantly provide interferometry baselines by selecting appropriate pairs of satellites.

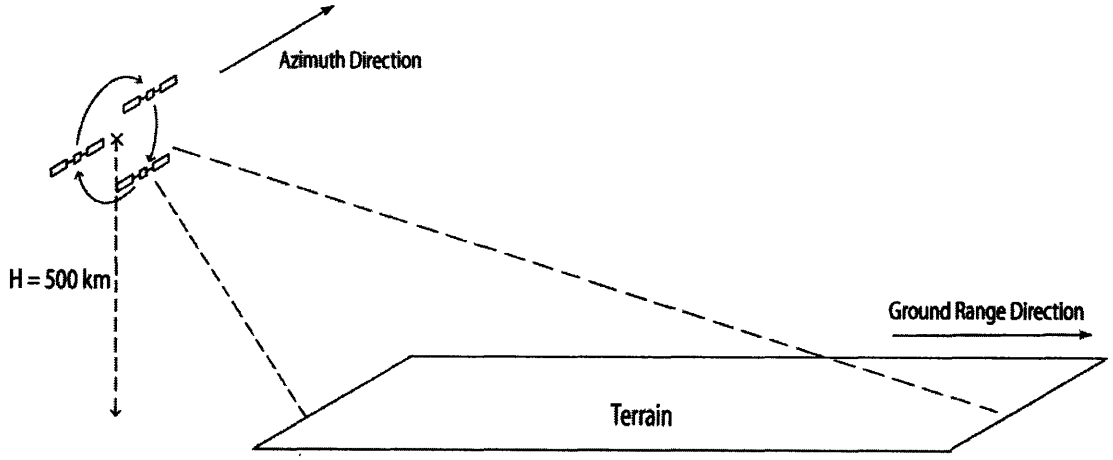

Figure 3-1: Interferometric cartwheel configuration.

Figure 3-1 illustrates the cartwheel setup used in our analysis. The cartwheel's plane lies perpendicular to the constellation's direction of motion. The satellites constantly rotate in a circular cartwheel fashion as the constellation advances in the azimuth direction, with each satellite side-looking on the same terrain. In addition, every satellite orientates itself with respect to a reference point [34], which in our case, is

chosen to be the center of the wheel. This reference point is assumed to be fixed at a height of $500km$ above sea level as the constellation advances.

We shall start off the analysis by first considering and setting up a three-satellite circular cartwheel system. The cartwheel's impacts on InSAR applications of both height retrieval and CCD shall then be addressed.

3.1 Satellites Cartwheel Setup

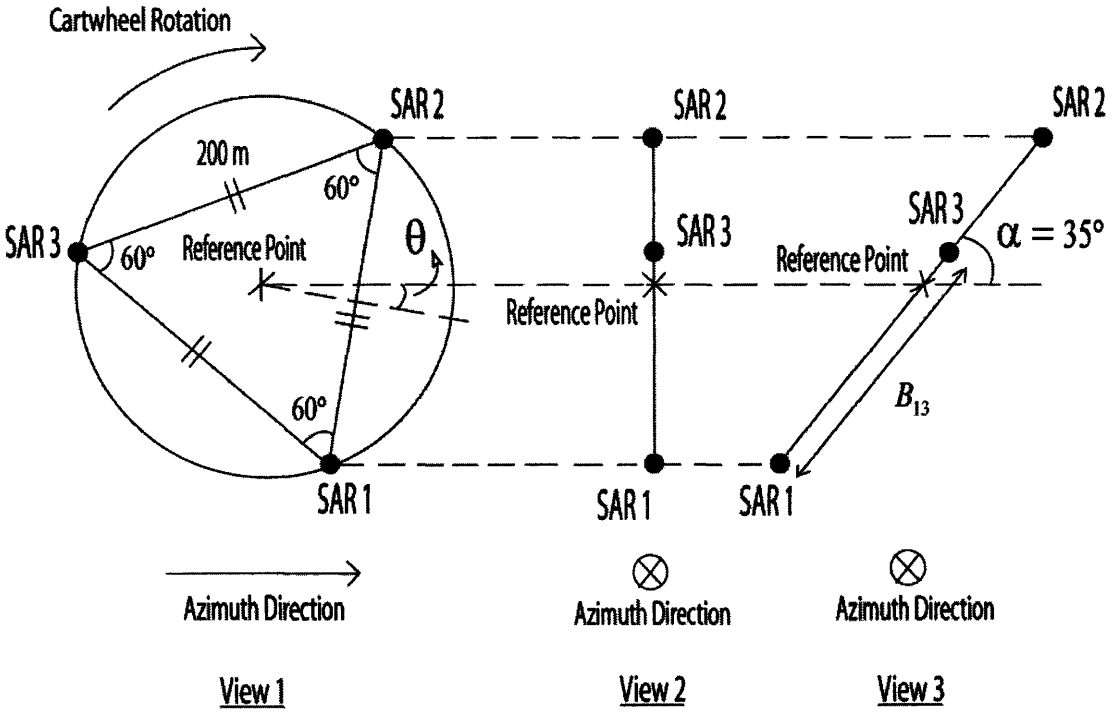

Figure 3-2: Three different views of the satellite cartwheel in the azimuth and range directions.

The satellite cartwheel when viewed from the azimuth and range directions are illustrated in figure 3-2. With reference to view 1, the three satellites are separated from one another by $200m$, forming an equilateral triangle upon joining up SAR 1, SAR 2 and SAR 3. As the constellation rotates in the clockwise direction about the triangle's centroid, the paths traced by the satellites define a circular wheel. This is assuming that the centroid, which is also assigned to be the constellation's reference point, remains stationary. In reality, the reference point, thus the constellation, advances in the azimuth direction. A rotation angle, θ, is defined to be the angle between the horizontal flight path and the line through the reference point perpendicular to side

12 of $\triangle 123$. θ is eventually used to relate to the satellite positions.

View 2 and 3 show the geometries which we will consider for height inversion. In fact, view 3 closely resembles the setup of figure 1-2 with side-looking radars, except that a collinear configuration is considered here. In our simulation, we first collapse the configuration of view 1 into that of view 2, and then project the vertical satellites arrangement such that they are at an angle, α, from the horizontal, as shown in view 3. The baseline elevation angle, α, is selected to be 35°, which is consistent with the definitions of section 1.3.3. This then allows us to apply the height retrieval process exactly as before on a collinear satellite configuration. In the following sections, the detailed implementation of the above cartwheel model is discussed.

3.1.1 Varying Baseline Lengths

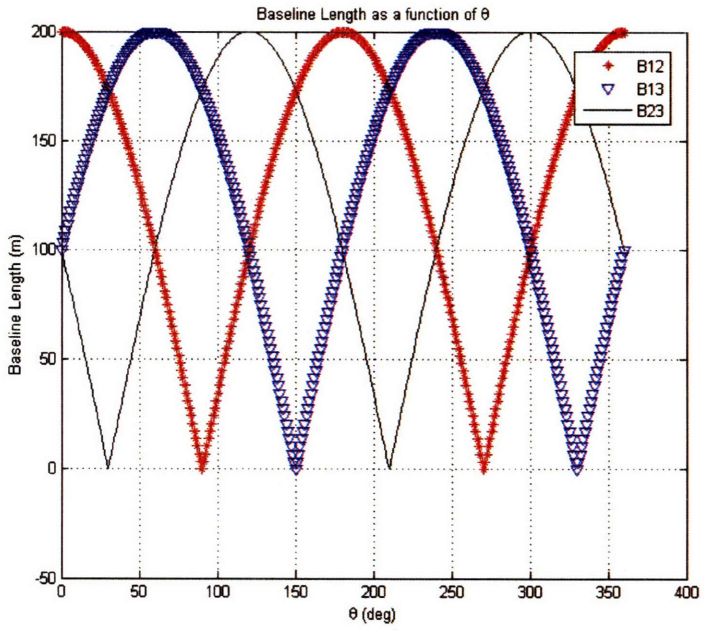

Figure 3-3: Relationship between the baseline length and the rotation angle, θ.

From figure 3-2, the true baseline length, B_{ij}, used for InSAR is the distance between satellite i and j of view 3. However, since view 2 and 3 only differs by horizontal shifts of the satellites, it is sufficient to only examine the *vertical* separations of the satellites in view 2 and treat them as the baselines. In that case,

$$B_{12} = 200\cos\theta \tag{3.1}$$

$$B_{13} = 200\cos(60° - \theta) \tag{3.2}$$

Depending on the value of θ, the corresponding B_{23} can be computed from B_{12} and B_{13} of eq. 3.1 and 3.2. This way, all three possible baseline lengths become functions

of the rotation angle. A plot showing this relationship for a complete turn of the cartwheel is presented in figure 3-3.

At $\theta = 0°$, it becomes obvious from view 1 of figure 3-2 that SAR 1 and SAR 2 are joined vertically with $B_{12} = 200m$ and $B_{13} = B_{32} = 100m$. This agrees well with the plot. As θ increases to 90°, SAR 1 and SAR 2 becomes joined up horizontally with $B_{13} = B_{23}$ and $B_{12} = 0m$. These observations again agreed with our plot.

3.1.2 Detection of the Bottommost Satellite

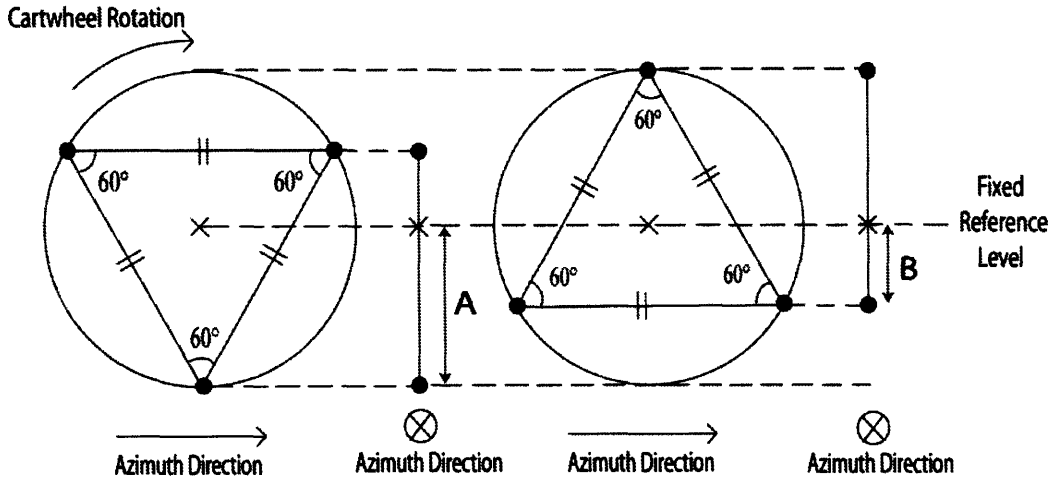

Figure 3-4: Bottommost satellite varying distance below the reference as the cartwheel rotates.

The figure above shows that the relative satellite positions with respect to the fixed reference level is constantly changing as the cartwheel rotates, such that the bottommost satellite changes from A to B distance below the reference. In order to correctly relate the satellite positions to the rotation angle, the bottommost satellite must first be detected, and then its vertical distance from the reference can be computed with knowledge of the wheel's spoke length. Figure 3-5 depicts these relationships as functions of θ in our implementation. For instance, at $\theta = 30°$, the plot detected SAR 1 as the bottommost satellite and it is at the maximum distance (wheel's spoke length) below the reference level. This, in view 1 of figure 3-2 translate to the cartwheel position where SAR 2 and SAR 3 form a horizontal line.

3.1.3 Satellite Positions for InSAR

By combining the work of the previous two sections, the satellite positions to be used for InSAR applications may now be established. For any value of θ, the bottommost satellite is first detected and its position relative to the reference point in the height-range plane is determined as described in section 3.1.2. After which, the relative positions of the other two satellites can be derived with knowledge of the baseline

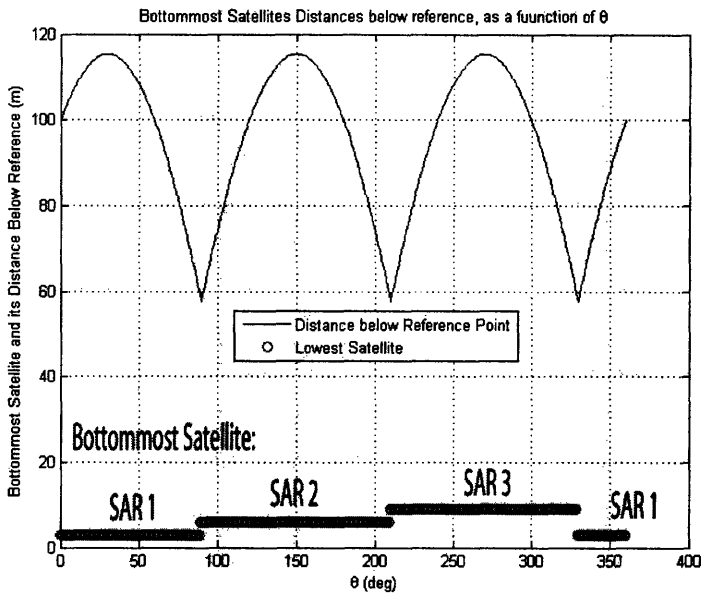

Figure 3-5: Detection of the bottommost satellite and its distance below the reference point.

lengths already obtained in section 3.1.1. The final positions are attained by projecting the satellites onto the line that forms an angle, α, with the horizon. This method is capable of modeling a three-satellite collinear configuration similar to that seen in view 3 of figure 3-2. In figure 3-6, the satellite positions used for height retrieval in our model are presented at $\theta = 0°, 10°$ and $30°$. It would be useful to compare these plots with their corresponding cartwheel orientations gathered in appendix A.

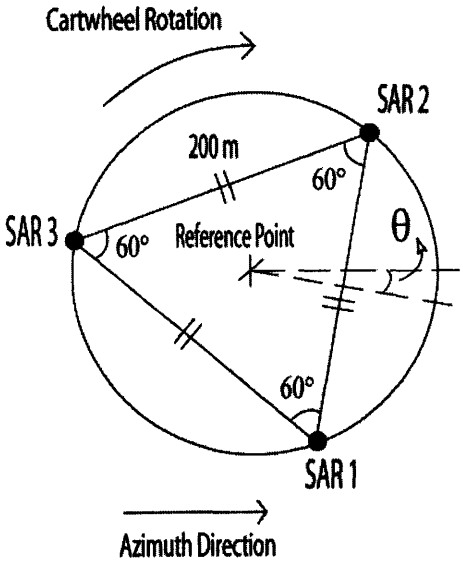

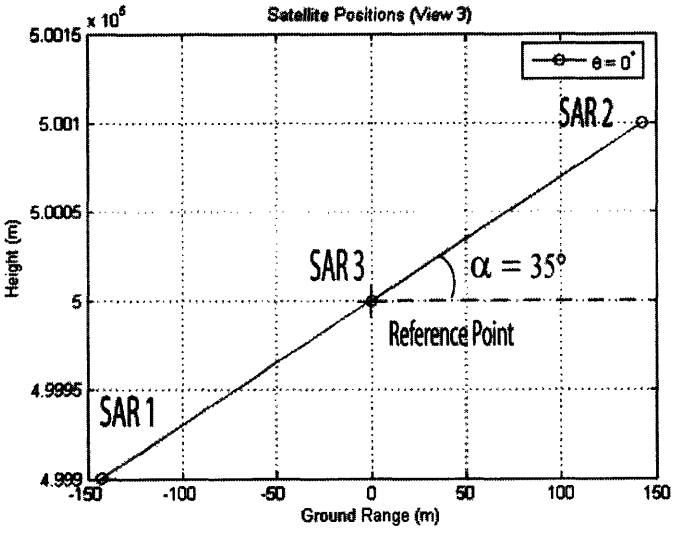

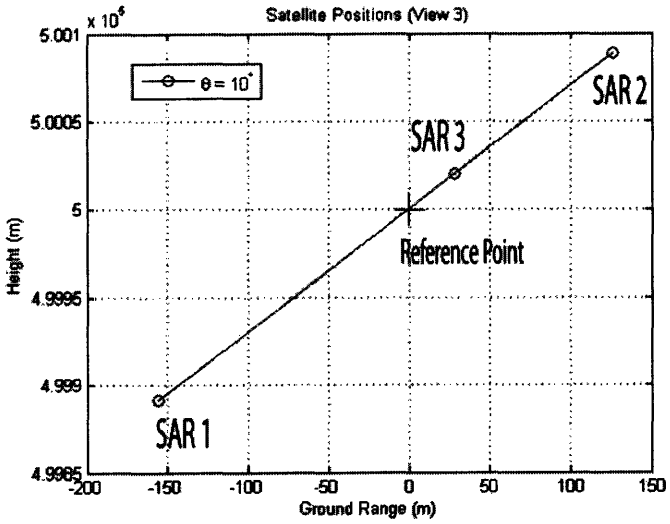

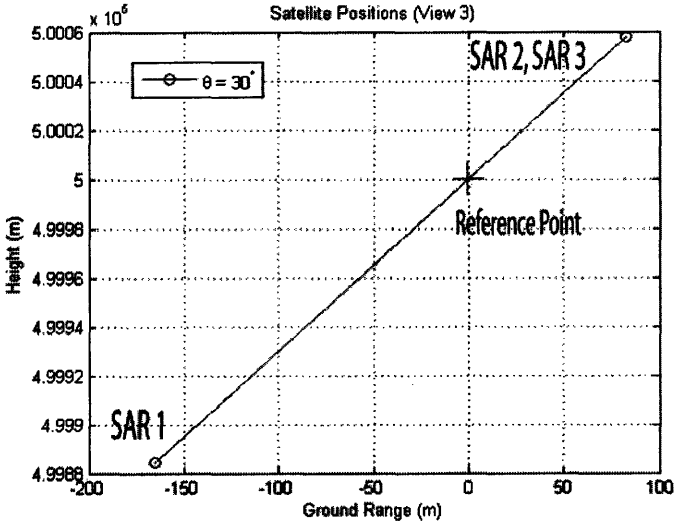

Figure 3-6: Satellite positions for $\theta = 0°, 10°$ and $30°$.

3.1.4 Accounting for Co-registration

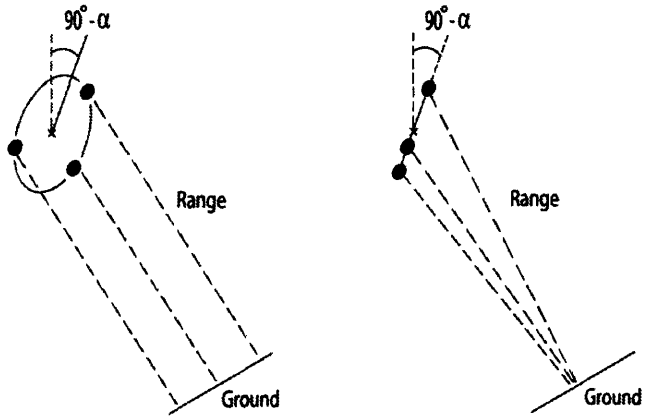

Figure 3-7: Modeling the three-satellite cartwheel as a collinear arrangement, upon application of co-registration.

Figure 3-7 shows the actual satellite cartwheel configuration when measurements of the ground's radar reflectivity are being taken. Each of the satellite, at any one time, lies on a distinct azimuth plane. Since DEM retrieval is not a real-time process, the measurements may first be recorded and the data be processed at a later stage. After applying co-registration to spatially align the data from each satellite, the original cartwheel configuration may equivalently be collapsed into a collinear arrangement, as illustrated in figure 3-7. This explains why the model described earlier, where the three satellites are implemented as if they all lie in a single cut of the azimuth plane, is valid.

3.1.5 Satellite Cartwheel Trajectory

We have been looking at the case where the cartwheel rotates about a stationary reference point. In this section, the trajectories of the satellites, as the cartwheel advances in the azimuth direction, will be derived. This implies that we should now relate the positions of the satellites to time, t, instead of θ.

At the same time the cartwheel rotates (i.e. θ changes), the constellation is also in motion along azimuth with the reference level fixed at a height of $500km$. In order for this constellation to maintain a circular orbit at $500km$ above earth, gravitational laws dictate the orbital period, as follows [35]:

$$T = 2\pi\sqrt{\frac{r^3}{\mu}} \tag{3.3}$$

where T is the orbital period and r is the orbit's radius. μ is a gravitational parameter that equals $\sim 398601km^3/s^2$ for earth. In our setup, the orbital period turns out to be $\sim$ 95 minutes and the corresponding velocity is $\sim 7.6km/s$. Furthermore, we

will assume the realistic case where the cartwheel rotates one complete round for one period of the constellation's revolution about earth [45]. As such, both cartwheel and constellation share the same period and all previous parameters that are functions of θ can be modified to become functions of t by replacing θ with $2\pi/T \times t$.

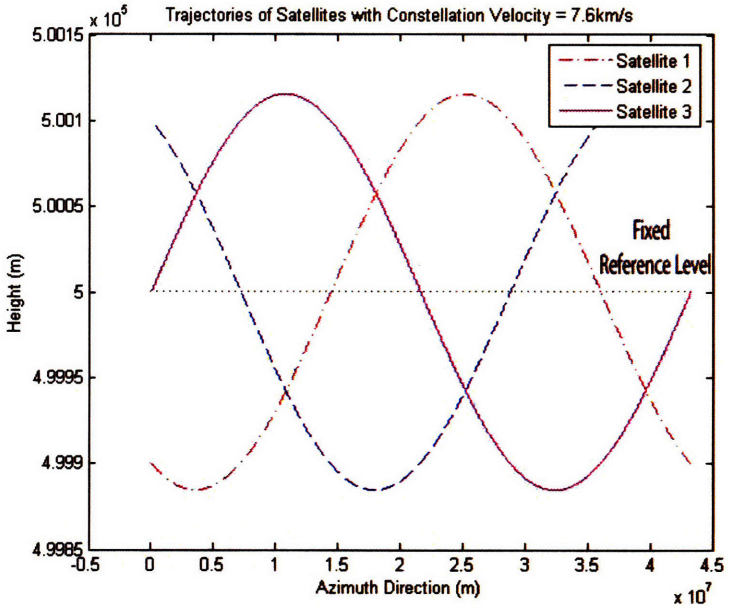

Figure 3-8: Satellites trajectories for a constellation velocity of $7.6km/s$.

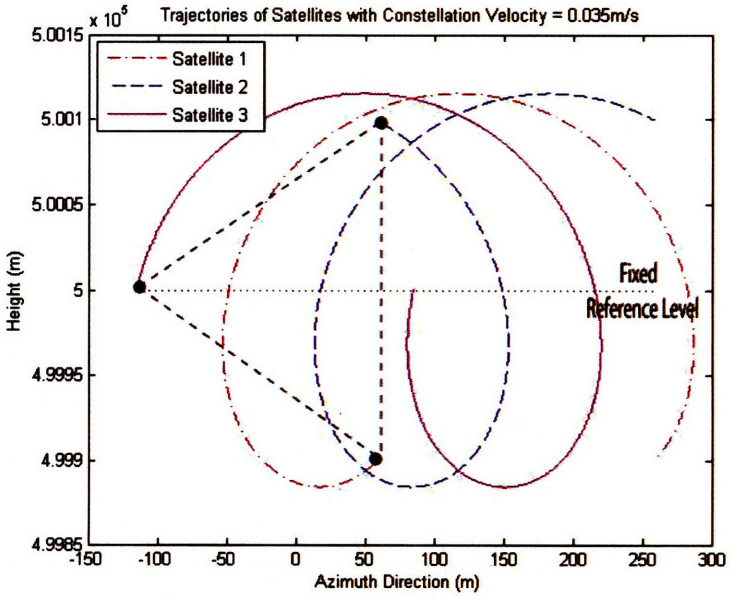

Figure 3-9: Satellites trajectories for a constellation velocity of $0.035m/s$.

In figure 3-8, the trajectories of the satellites, in the height and azimuth directions, are plotted for an orbit of the constellation about earth. It can be observed that each satellite makes one turn of the cartwheel during this time frame.

To examine the trajectories in greater details, figure 3-9 shows a similar plot but with the constellation velocity drastically reduced to $0.035m/s$, allowing us to more closely follow each satellite's path. Again, the cartwheel makes one complete rotation during this time. In the plot, the initial satellite positions (i.e. $\theta = 0°$) are also highlighted.

3.2 Height Retrieval with the Cartwheel

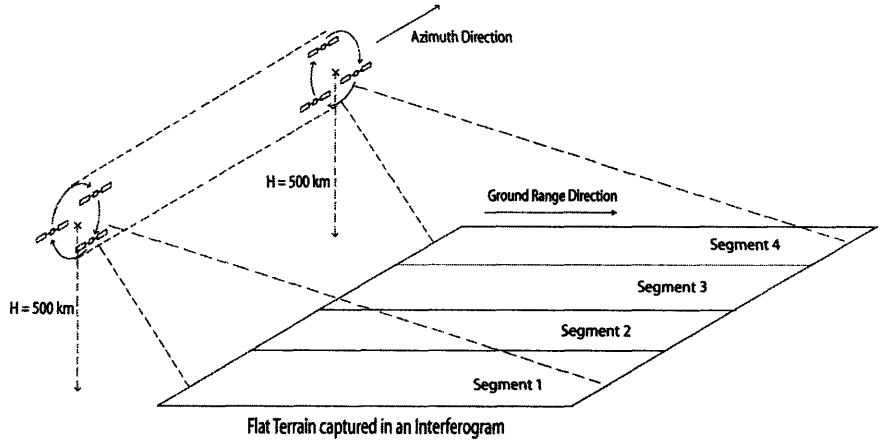

Figure 3-10: Snapshot of an interferogram using the interferometric cartwheel.

In this section, we shall apply our interferometric cartwheel model to retrieving the DEM. To facilitate our understanding of this consequence, a flat ground at sea level is used as the test terrain. A snapshot of a 256×256 interferogram, with azimuth resolution $\sim 5m$, usually occurs in $\ll 1s$ for a satellite's velocity of several km/s. Hence, the satellite positions may generally be approximated to be constant in the height-azimuth plane within this small time frame. However, as we shall see later in this section, the same approximation can no longer be made with a cartwheel configuration. Figure 3-10 shows a snapshot of the test terrain by the satellite cartwheel. Notice that in forming this single interferogram, the cartwheel rotates within itself as the constellation advances.

Ideally, we would like to be able to trace the actual positions of the satellites as the cartwheel rotates while taking the snapshot. However, in practice, only one set of the geometry parameters and satellite positions corresponding to each interferogram is available. In our analysis, we shall assume that the set of parameter values that corresponds to the satellite positions at the beginning of every shot of the interferogram is used for terrain height inversion. This assumption is illustrated in figure 3-11.

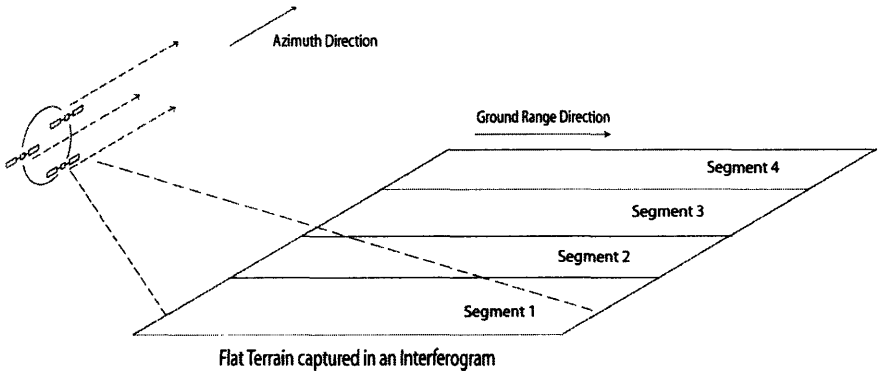

Figure 3-11: Snapshot of an interferogram, assuming that the interferometric cartwheel is not rotating in this time frame.

We have already seen from eq. 1.18 that the baseline length, B, is required for height inversion. This equation is presented here again for the general case:

$$\theta = \alpha + \sin^{-1}\left(\frac{\delta}{B} + \frac{B}{2\rho} - \frac{\delta^2}{2B\rho}\right)$$

Furthermore, because $\rho \gg B$ and $\rho \gg \delta$, the following approximation can be made:

$$\left(\frac{\delta}{B} + \frac{B}{2\rho} - \frac{\delta^2}{2B\rho}\right) \approx \frac{\delta}{B} \tag{3.4}$$

such that eq. 1.18 now becomes

$$\theta = \alpha + \sin^{-1}\left(\frac{\delta}{B}\right) \tag{3.5}$$

This shows that the baseline elevation angle, α, the one-way slant range difference, δ, and the baseline length are critical parameters in the height inversion process. For our setup, α is kept at 35° while δ is retrieved from the unwrapped interferogram (see eq. 1.17). Hence, knowledge of only one set of the parameter values when the actual cartwheel configuration is constantly rotating propagates into errors of the baseline length. This may also be inferred from figure 3-3. Effects of under- and over-estimation of the baseline lengths will be look into in section 3.2.3.

3.2.1 Determining the Angle of Rotation

A realistic implementation of our model is to assume that the cartwheel rotates one complete round for one period of the constellation's revolution about earth. The path distance covered by the constellation in a period of its orbit can be determined by

$$L = 2\pi(R + H) \tag{3.6}$$

where R is the earth's radius and H is the constellation's height. L is found to be $4.3 \times 10^4 km$ for our setup. A typical 512×512 interferogram having azimuth resolution of $4m$ covers a ground distance of $\sim 2km$ in the azimuth direction. In order to cover this ground area in our setup, the cartwheel would have to rotate $2/L \times 360° = 0.02°$ within a snapshot of the interferogram. This angle of rotation shall henceforth be used for subsequent height retrieval with the interferometric cartwheel.

3.2.2 Discretizing the Rotation Angle

In setting the cartwheel to rotate 0.02° within a snapshot of the test terrain, the interferogram is divided up into four segments, as shown in figures 3-10 and 3-11. Consequently, the total angle of cartwheel rotation is also discretized evenly into four angles, from $\Delta\theta = 0°$ to $\Delta\theta_{final} = 0.02°$. Each segment of the interferogram then corresponds to an angle of the cartwheel orientation, θ. For instance, if segment 1 is related to $\theta_{initial}$ of the cartwheel, then segment 4 relates to $\theta_{initial} + \Delta\theta_{final}$.

In reality, the change in the cartwheel's angle of rotation is continuous and a better approximation would be to sample $\Delta\theta_{final}$ at a much higher rate, i.e. dividing the interferograms into many more segments. However, a coarse sampling rate of $\Delta\theta_{final}$ is preferred for analysis because it enables us to more closely study the impact of the cartwheel effects on height retrieval for each segment. In fact, for small $\Delta\theta_{final}$, varying sampling rate has minimal impacts on analysis since the ideal continuous case can really be thought of as the discretized case with varying sampling rates. Nonetheless, when $\Delta\theta_{final}$ gets too large (i.e. 5°), abrupt phase changes occur in the interferograms leading to breakdown of the coarsely sampled approximation. We shall look into the cause of this breakdown for the case when $\Delta\theta_{final}$ is large and at the same time coarsely sampled, and compare to the case when it is small or more finely sampled.

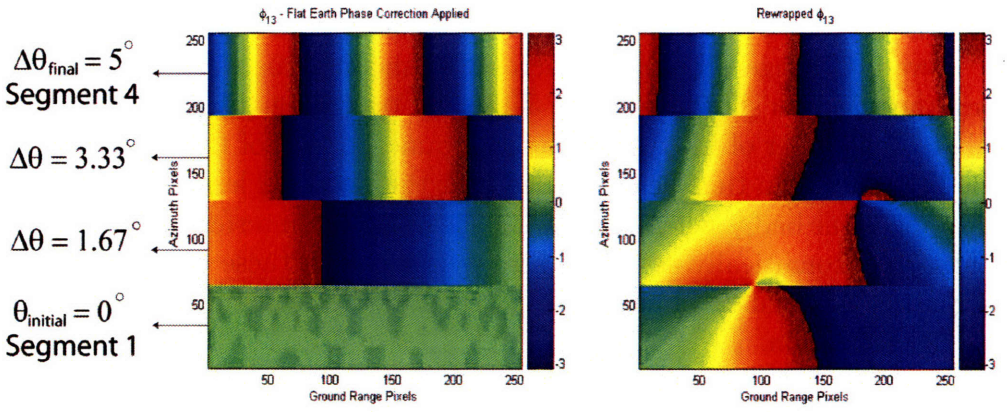

Figure 3-12: $\Delta\theta_{final} = 5°$ with *coarse* sampling — interferogram, ϕ_{13}, after flat earth correction and the rewrapped phase.

Figure 3-12 illustrates the phase data for a setup where the cartwheel's total angle of rotation in a snapshot of the interferogram is 5°, with a starting position of $\theta_{initial} = 0°$. Interferogram ϕ_{13}, corresponding to data from SAR 1 and SAR 3, is shown after flat earth phase correction has been applied. The interferogram is divided into four segments and each of them corresponds to an angle θ of the cartwheel's orientation, as highlighted in the figure. Since the test terrain is flat and segment 1's true parameter values are known, the flat earth correction compensate the phase exactly in segment 1 such that it has a constant zero value. The same does not hold true for the other segments due to the cartwheel's rotation. Nonetheless, it should be pointed out this inexact flat earth correction for the other segments does not propagate into any form of error in the height retrieval process since the flat earth is only a reference phase used to reduce the phase variations before unwrapping. The key here is to add back the same phase that was subtracted, after the unwrapping process.

The rewrapped phase data after unwrapping of ϕ_{13} is observed to differ from the original wrapped data, implying that least-squares unwrapping has failed. In particular, the constant phase of segment 1 cannot be retrieved. The reason is that coarse sampling of $\Delta\theta_{final}$ results in the cartwheel's orientation changing abruptly from one segment to the next, creating fringes in the flat earth corrected phase data in segments 2, 3 and 4. If the residue-weighted least-squares unwrapping is applied without modification, these fringes will propagate across the shears into neighboring segments, leading to incorrect unwrapped phase data.

To understand the above phenomenon better, a flat-ramp test terrain, consisting of a $600m$ high ramp placed directly besides a flat ground, is used. Figure 3-13(a) also illustrates the corresponding interferogram formed by a two-satellite setup after being corrected for flat earth. While the flat ground portion of it has zero phase values, the ramp portion consist of fringes similar to those in figure 3-12. Figure 3-13(b) shows the propagation of these fringes into the neighboring flat ground portion together with the weighting scheme that the least-squares unwrapping used. In order to prevent unwanted fringe propagation across the shear, zeros weights are later enforced along the shear as shown in figure 3-13(c). Comparing (b) and (c), it can be observed that the number of fringes in the flat ground portion of the rewrapped data has been decreased. It can thus be concluded that the weighted least-squares unwrap will generally perform badly when faced with shears in the interferogram, due to its ineffectiveness in automatically assigning zero weights along these boundaries. Thus, we should restrict to smaller values of $\Delta\theta_{final}$, as in the realistic case, when using such coarse discretization.

Coarse sampling is only used to help us investigate the effects of the interferometric cartwheel on the height retrieval process. Once we have understood its mechanics after the next section, all subsequent simulations will be carried out with much finer sampling. In that case, such phase errors will no longer surface, allowing our model to be applied for large values of $\Delta\theta_{final}$. In figure 3-14, fine sampling is applied such that the interferogram is divided into segments equal to the number of azimuth pixels

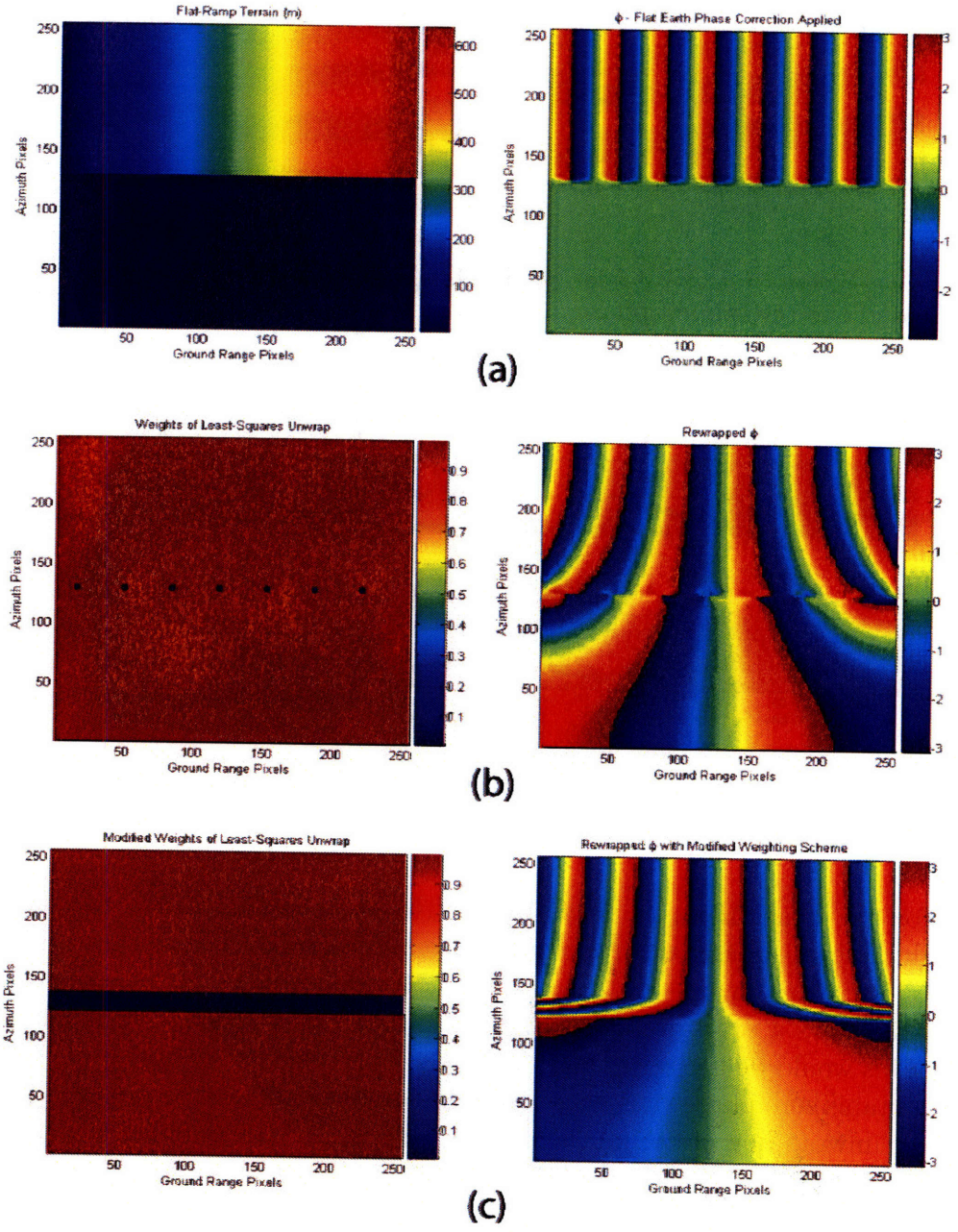

Figure 3-13: (a) Flat-ramp terrain and its interferogram. (b) Automated weighting scheme and the rewrapped interferogram. (c) Modified weighting scheme and the rewrapped interferogram.

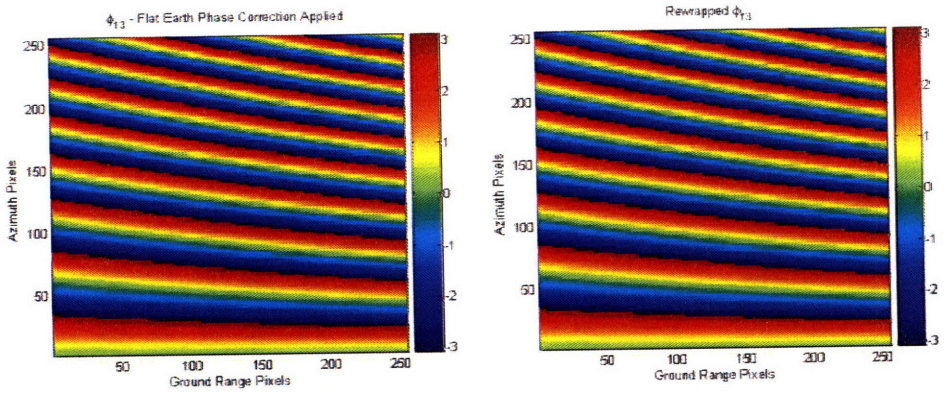

Figure 3-14: $\Delta\theta_{final} = 5°$ with *fine* sampling — interferogram, ϕ_{13}, after flat earth correction and the rewrapped phase.

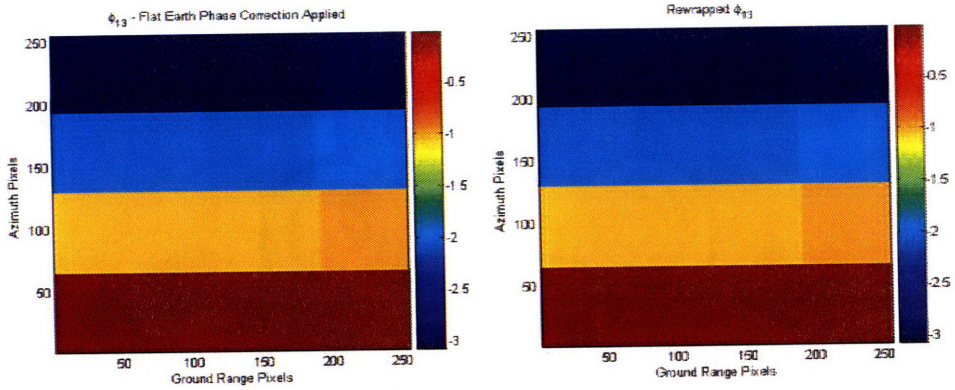

Figure 3-15: $\Delta\theta_{final} = 0.02°$ with *coarse* sampling — interferogram, ϕ_{13}, after flat earth correction and the rewrapped phase.

– 256. For the same $\Delta\theta_{final} = 5°$ as before, the ϕ_{13} now appears to be continuous and weighted least-squares unwrapping is executed correctly.

Figure 3-15 shows a coarse discretization as in figure 3-12 but with a much smaller $\Delta\theta_{final}$. This would be the setup used for analysis in the next section. Here, segment 1 again contains zero phase values and no fringes appear in the other regions, enabling the correct unwrapping of the interferogram. Hence, our model remains valid.

3.2.3 Baseline Errors and Cartwheel Height Retrieval

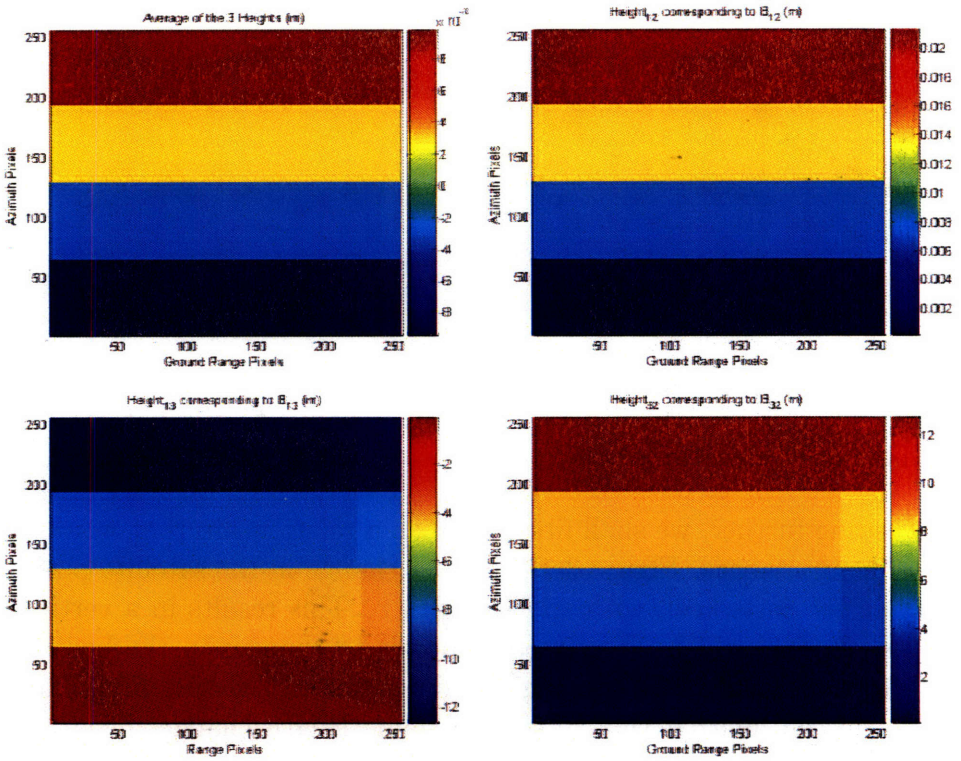

Figure 3-16: Retrieved terrain heights corresponding to B_{12}, B_{13} and B_{32}, and their average, for $\theta_{initial} = 0°$.

We begin our investigation of the cartwheel effects on height retrieval by looking at the $\theta_{initial} = 0°$ case. In this section, noise will not be introduced and the total cartwheel rotation angle of 0.02° within a snapshot of the interferogram is always evenly discretized into four values. Figure 3-16 shows the retrieved heights h_{12}, h_{13} and h_{32} from the flat test terrain corresponding to B_{13}, B_{12} and B_{32}. Notice that the correct height is always retrieved in segment 1, i.e. the lowest segment in the map, as expected because the retrieval parameters used correspond to this segment. It can be observed that h_{12} correctly retrieve the flat test ground while the topology in h_{13} and h_{32} appears as steps going downwards and upwards respectively. In fact, some form of symmetry appears between h_{13} and h_{32}. Furthermore, when these three sets of retrieved heights are averaged according to eq. 2.1, with weighting functions

$$w_{12} = 1; w_{13} = 1; w_{23} = 1 \tag{3.7}$$

the resulting averaged height profile is flat with a variation of $\pm 1 \times 10^{-2} m$ over the entire map. It was suggested at the beginning of this section that a constantly rotating cartwheel propagates into baseline errors in height retrieval. We shall now investigate this in greater details, on the specific case when $\theta_{initial}$ is 0°, in order to explain the symmetry in heights observed and why averaging seems to work well here.

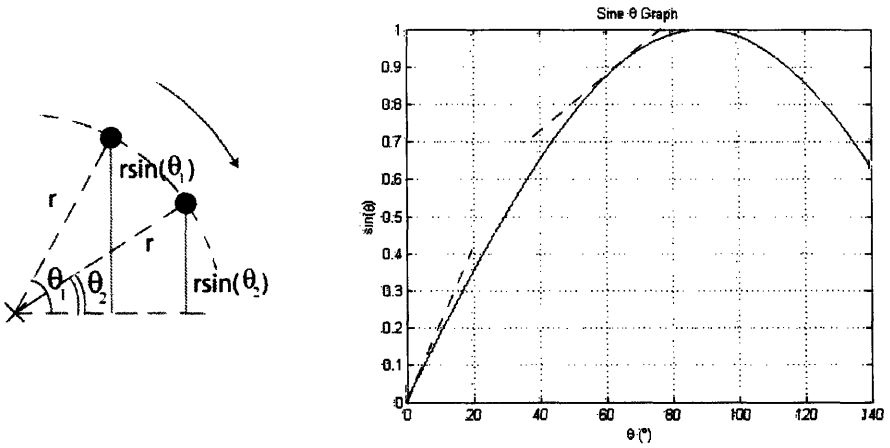

Figure 3-17: Relating the magnitude of baseline change to the horizontal distance form cartwheel's reference point.

Before proceeding further, we shall first establish a relationship that would be useful in the subsequent analysis. Figure 3-17 shows a change in the satellite position from θ_1 to θ_2 about the cartwheel, with spoke length r. This results in a vertical change of $r(\sin(\theta_1) - \sin(\theta_2))$ which directly corresponds to changes in the baseline length (see view 2 of figure 3-2). By relating the difference in the sine functions to their gradients, it can be inferred that greater baseline length changes occur at smaller angles of θ while small baseline length changes occur for θ near 90°. As such, the following relationship is established:

$$\text{Magnitude of vertical change} \propto \text{Horizontal distance from reference point} \quad (3.8)$$

Figure 3-18 illustrates the rotation of the cartwheel from 0° to 0.02°, and the corresponding change in the vertical baseline lengths. Using the relationship derived in eq. 3.8, SAR 1 and 2, which are at the same horizontal distance from the cartwheel's reference point, are both shifted downwards by an amount a. SAR 3 is shifted upwards by b, where $b > a$ since SAR 3 is at the maximum possible distance away from the reference point. As a result, vertical B_{13} *increases* by $a + b$, vertical B_{32} *decreases* by $a + b$, and B_{12} remains relatively unchanged. Such observations may be generalized as an underestimation of B_{13}, that worsens from segment 1 to 4, in the height retrieval process since the actual baseline length increases from one segment to the other but fixed parameter values corresponding to segment 1's are used instead. Similarly, an overestimation of B_{32} occurs.

Simulations data in table 3.1 confirms our observations made in figure 3-18 where B_{13} and B_{32} changes by the same amount in opposite directions while B_{12} remains the same as the cartwheel rotates 0.02° clockwise.

Wong, in his thesis [8], has already investigated the effects of baseline errors on two-dimensional height retrieval using a two-satellite setup. Ignoring foreshortening effects, his findings may be summarized as:

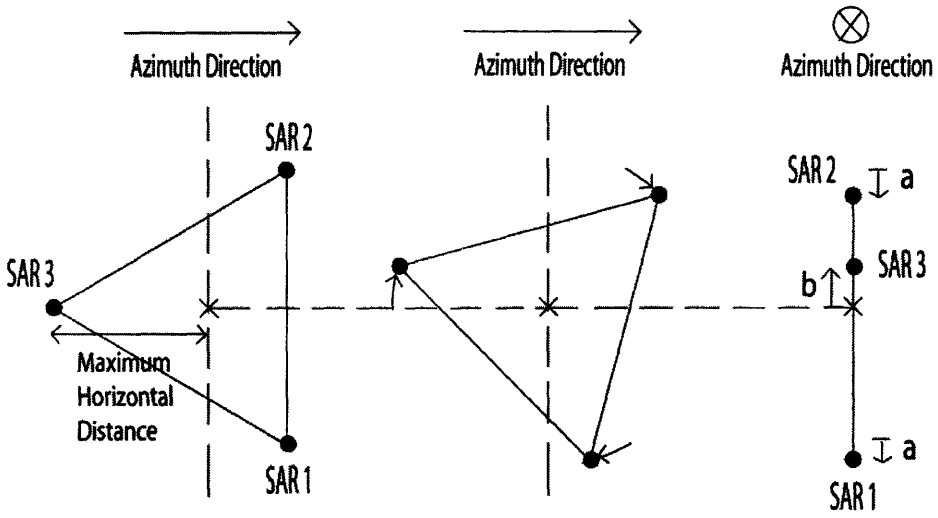

Figure 3-18: Relating cartwheel rotation to baseline changes for $\theta_{initial} = 0°$.

θ (°)	0	0.02	**Percentage Change (%)**
B_{12} (m)	348.69	348.69	0
B_{13} (m)	174.34	174.45	+0.06
B_{32} (m)	174.34	174.24	−0.06

Table 3.1: Baseline lengths for $\theta_{initial} = 0°$.

- An underestimate of the baseline length leads approximately to a vertical shift of the retrieved terrain heights downwards as compared to the original terrain profile.

- Similarly, an overestimate of the baseline length will lead to a upwards shift of the retrieved terrain heights.

- For small change of the baseline length such that θ', in his derivation, is small, an equal increment or decrement of the baseline will result in the same shift of the retrieved terrain upwards and downwards respectively. This is true in our case since baseline length changes by $< \pm 1\%$.

- The more the baseline length deviates from the true value, the greater the shift in the retrieved heights.

The above summary allows us to relate figure 3-18 to the observations made in figure 3-16, where

- Underestimation of B_{13} leads to vertical shifts of the original flat terrain, at $H = 0m$, downwards to negative values. These shifts in h_{13} increases from segment 1 to 4 as the cartwheel rotates and deviations of the baseline length increases, from one segment to the next. This explains the downwards steps observed in h_{13}.

- The opposite may be concluded for h_{32}.

- Minimal distortions occur for h_{12} because B_{12} remains relatively unchanged.

Furthermore, the symmetry observed between h_{13} and h_{32} is well-defined since B_{13} and B_{32} changes in the opposite directions by the same small amount. Thus, averaging of the three sets of heights data with simple weighting functions of eq. 3.7 indeed should work to cancel out the vertical shifts and return the original flat terrain. Now, in circular cartwheel configuration, averaging is no longer an option but rather, a necessary step in order to retrieve correctly the DEM. However, does simple averaging always work? To address this, we look at another extreme case where the $\theta_{initial}$ of the cartwheel is selected to involve satellites at the minimum horizontal distance away from the reference point. $\theta_{initial} = 30°$ satisfies the requirements and its corresponding cartwheel configuration is shown in figure 3-19.

θ (°)	30	30.02	**Percentage Change (%)**
B_{12} (m)	301.97	301.91	−0.02
B_{13} (m)	301.97	302.03	+0.02

Table 3.2: Baseline lengths for $\theta_{initial} = 30°$.

There is minimum change in the vertical displacement of SAR 1 since it is right below the reference point. SAR 2 and 3 are at equal horizontal distances away from the reference point and are therefore, vertically displaced by the same amount c as the cartwheel rotates 0.02° clockwise. This results in an equal increment and decrement of B_{13} and B_{12} respectively (see table 3.2), leading eventually to underestimates of h_{13} and overestimates of h_{12} in the form of steps, as depicted in figure 3-20. The above observations agree well with our previous analysis of the $\theta_{initial} = 0°$ case. h_{32} is ignored here because B_{32} is initially zero such that height retrieval is impossible.

The symmetries of the retrieved heights, h_{13} and h_{12}, are consequences of an equal but opposite change in B_{12} and B_{13}. Thus, applying averaging with eq. 2.1 and weighting functions

$$w_{12} = 1; w_{13} = 1; w_{23} = 0 \tag{3.9}$$

the initial flat test terrain can be attained. Now, it seems that by selecting appropriate weighting functions each time for a different $\theta_{initial}$, the correct terrain may be retrieved despite the cartwheel's constant rotation within a snapshot of the interferogram. However, we would like this process to be automated so that it also works for cases where symmetry of the retrieved heights does not exist. Intuitively, from the $\theta_{initial} = 30°$ example, the weighting functions should somehow be related to the baseline length such that $w_{23} = 0$ when $B_{23} = 0$. In the next section, the weighted averaging technique discussed in section 2.1.2 shall be applied to cartwheel height retrieval.

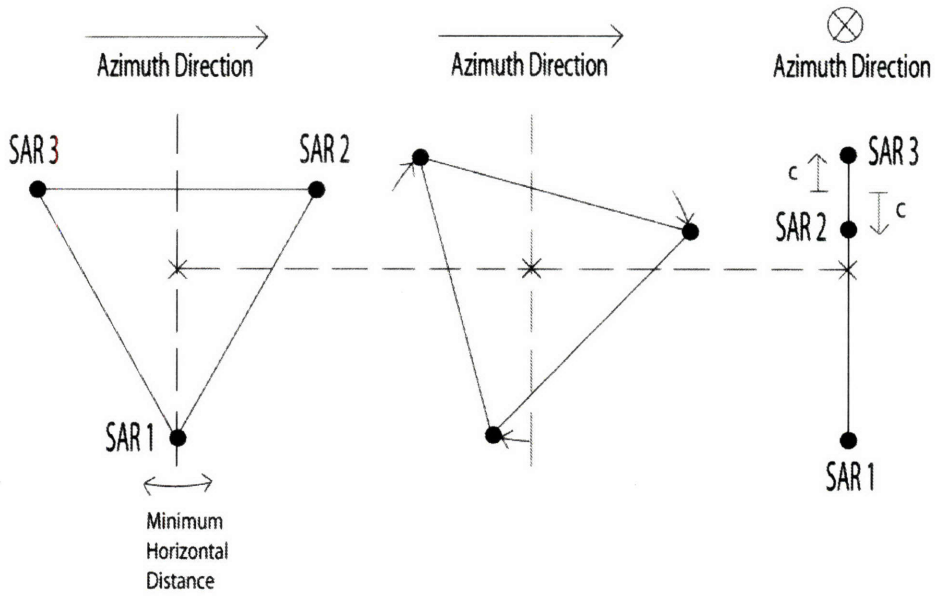

Figure 3-19: Relating cartwheel rotation to baseline changes for $\theta_{initial} = 30°$.

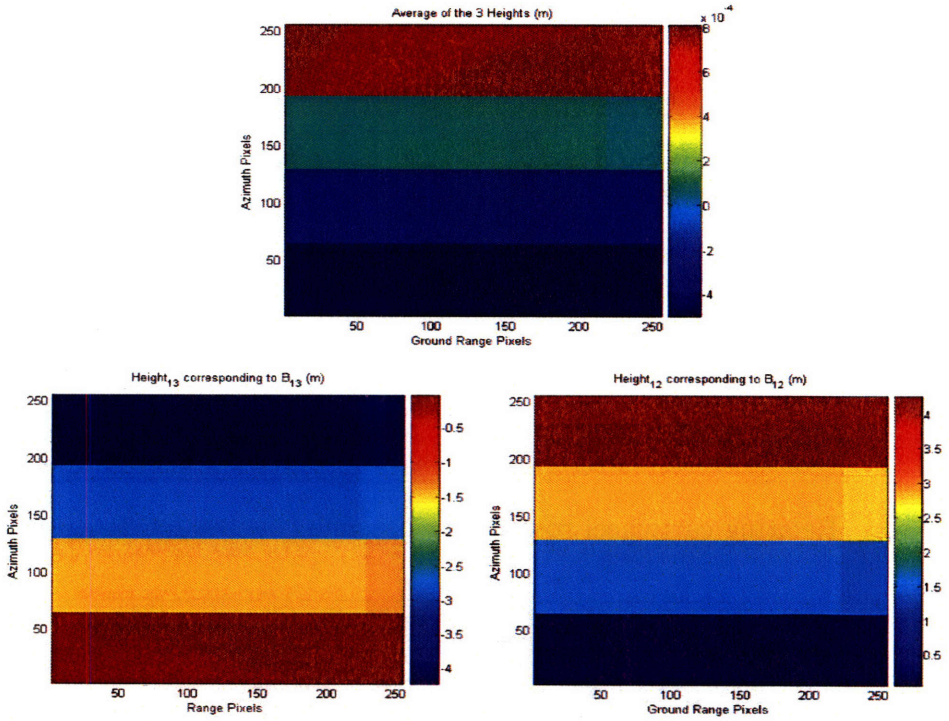

Figure 3-20: Retrieved terrain heights corresponding to B_{12}, B_{13} and B_{32}, and their average, for $\theta_{initial} = 30°$.

3.2.4 Weighted Averaging

Simply by inspection, it becomes obvious that baseline-weighted height averaging of eq. 2.7, repeated below for convenience, should work in the cartwheel height retrieval process in our two previous examples.

$$\hat{h} = \frac{\sum_{i=1}^{N} B_{\perp i}^2 h_i}{\sum_{i=1}^{N} B_{\perp i}^2} \tag{3.10}$$

In the $\theta_{initial} = 0°$ example, equal weighting (i.e. $B_{13} = B_{32}$) of h_{13} and h_{32} ensures that the equal and opposite vertical shifts of the retrieved heights are canceled out. Similarly, for the $\theta_{initial} = 30°$, h_{13} and h_{12} are equally weighted while h_{32} are not considered in the averaging scheme, which is as desired.

In continuing our quest for an automatic cartwheel configuration height retrieval process, the baseline-weighted averaging technique was applied on a case where no symmetry in the retrieved heights exists. $\theta_{initial} = 15°$ and $\Delta\theta_{final} = 0.02°$ is selected for this purpose.

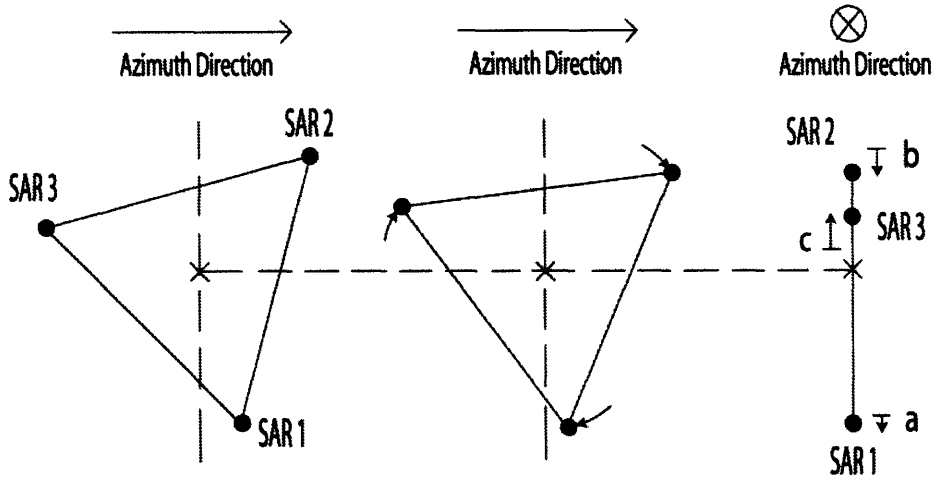

Figure 3-21: Relating cartwheel rotation to baseline changes for $\theta_{initial} = 15°$.

θ (°)	15	15.02	**Percentage Change (%)**
B_{12} (m)	336.81	336.78	−0.009
B_{13} (m)	246.56	246.65	+0.035
B_{32} (m)	90.25	90.13	−0.130

Table 3.3: Baseline lengths for $\theta_{initial} = 15°$.

From figure 3-21, the original positions of SAR 1, 2 and 3 are all at different horizontal

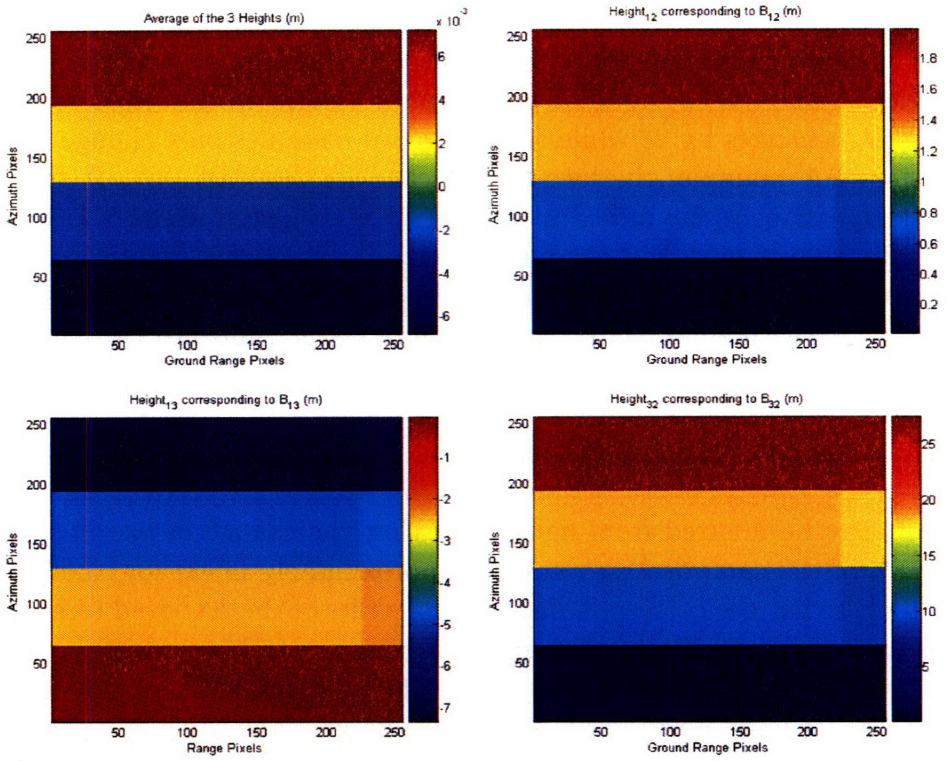

Figure 3-22: Retrieved terrain heights corresponding to B_{12}, B_{13} and B_{32}, and their average using baseline-weighted averaging technique, for $\theta_{initial} = 15°$.

distances from the cartwheel's reference point, resulting in varying vertical shifts of the satellites as the cartwheel rotates. According to eq. 3.8, it can be deduced that $a < b < c$. From the diagram, B_{12} decreases by $b - c$, B_{13} increases by $a + c$ and B_{32} decreases by $a + b$. The numerical values for these baseline length changes are tabulated in table 3.3 and it can be observed that all three lengths change by different amounts. As such, no form of symmetries in the retrieved heights are expected, as verified in figure 3-22. In fact, overestimates of B_{12} and B_{32} in the height retrieval process lead to vertical shifts of the retrieved terrain upwards while underestimates of B_{13} leads to downwards shift of the original flat terrain. These shifts are again proportional to the magnitude of baseline changes.

When the baseline-weighted averaging is applied to this cartwheel setup where no symmetries of the retrieved heights (i.e. h_{13}, h_{12} and h_{32}) exists, the original flat terrain is obtained as shown in figure 3-22. And when unity-weighted averaging that works well with the $\theta_{initial} = 0°$ case is applied instead, a RMS error of $1.3695m$ is attained. So, the baseline-weighted averaging scheme, having been successfully tested on two "extreme" cartwheel's orientation setups and an in-between case, does work to automatically retrieved the DEM.

To look deeper into the mechanics of the baseline-weighted averaging, we must first recognize from the geometries setup, i.e. figures 3-18, 3-19 and 3-21, that short base-

lines are generally associated with large changes in their length as the cartwheel rotates while the inverse is true for a longer baseline. For instance, when $\theta_{initial} = 0°$, B_{12} is the longest and has the minimal change in its length. In the $\theta_{initial} = 30°$ setup, the shortest B_{32} changes by $2c$ while the other two baselines only change by c each. In the most recent example, the longest B_{12} changes the least, by -0.009%, while the shortest B_{32} changes the most, by -0.130%. In weighted averaging, we seek to compensate for the vertical shifts of the three retrieved heights due to inexact baseline parameters. So, terrains with inherently large vertical shifts should be weighted lighter than those with small shifts, in order for the net shifts to cancel out. This is achieved with baseline-weighted averaging where we have already established that short baselines, hence, lighter weights, are associated with large length changes or corresponding, large vertical terrain shifts. The reverse applies for long baselines.

Moreover, it may be inferred from figure 3-17 that the change in baseline length as a consequence of the cartwheel's rotation is approximately linear for small angles of $\Delta\theta$. This implies that the corresponding vertical shifts of the retrieved terrains follow a linear relationship as well and that linear weights are to be used in the averaging scheme. However, eq. 2.7 derived uses B^2 weighting functions and was observed to outperform a linear baseline weight function when applied on the non-collinear three-satellite configuration setup. Nonetheless, the scheme still works well for extremely small $\Delta\theta$, as we have seen, but may eventually breakdown as it increases, and yet remains small at $< 1°$. In the next section, we shall define a critical $\Delta\theta$ where the breakdown occurs.

3.2.5 Optimum Angle of Rotation for Height Retrieval

The baseline-weighted averaging will now be applied on the interferometric cartwheel configuration using the test terrain defined in section 1.3.2 for various $\theta_{initial}$ in noisy environments. In appendix A, the orientations of the cartwheel at 15° increments of the rotation angle, θ, are shown. Due to the symmetry observed, it is sufficient to only consider θ from 0° to 120°. Moreover, dense discretization of $\Delta\theta_{final}$, similar to that applied on figure 3-14, is used to ensure that the flat-ramp phase issues discussed in section 3.2.2 do not surface. Figure 3-23 shows a plot of the mean RMS height error of the retrieved heights at varying noise levels for $\theta_{initial} = 0°$ to 105° at 15° increments. The correct terrain profiles are retrieved for all values of $\theta_{initial}$ since their plots follow a similar trend to that found in the three-satellite non-collinear setup of figure 2-1.

It was reported in [8] that the optimum cartwheel orientation for height retrieval via data averaging occurs at $\theta = 30°$. In the current baseline-weighted averaging implemented with a constantly rotating cartwheel, no optimum position is deemed to exist, as observed from table 3.4. In fact, all eight plots of the various $\theta_{initial}$ values fall almost on the same line, with the average maximum deviations among them across

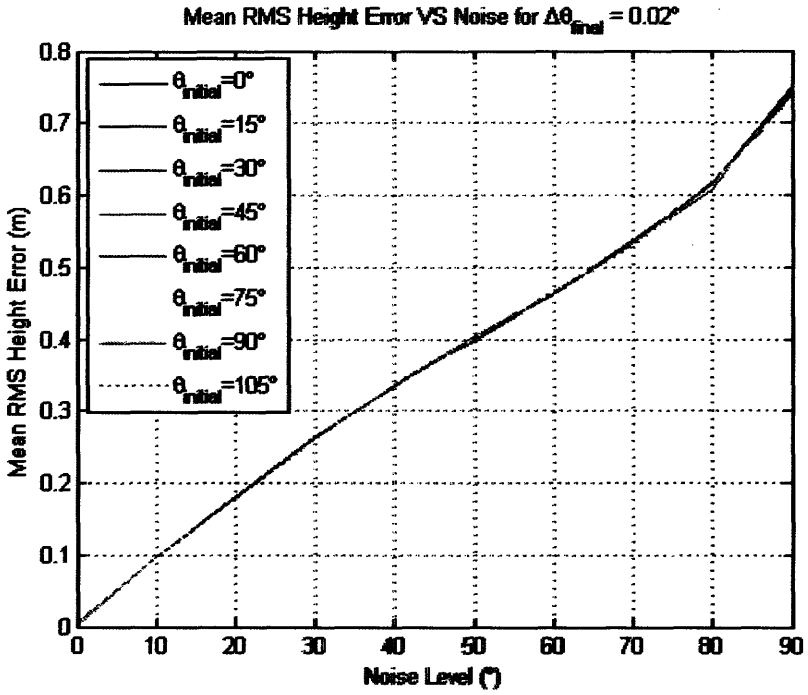

Figure 3-23: Mean RMS height error as a function of noise level for various $\theta_{initial}$ values with $\Delta\theta_{final} = 0.02°$.

	Mean RMS height error (m)							
Noise Level (°)	$\theta_{initial} = 0°$	15°	30°	45°	60°	75°	90°	105°
0	0.0057	0.0042	0.0007	0.0034	0.0049	0.0034	0.0007	0.0042
10	0.0971	0.0967	0.0970	0.0969	0.0974	0.0971	0.0964	0.0968
20	0.1813	0.1801	0.1810	0.1803	0.1815	0.1808	0.1814	0.1814
30	0.2599	0.2604	0.2623	0.2631	0.2612	0.2614	0.2603	0.2631
40	0.3380	0.3340	0.3353	0.3350	0.3335	0.3378	0.3354	0.3361
50	0.3993	0.4013	0.4041	0.4039	0.4030	0.4019	0.4029	0.4041
60	0.4643	0.4651	0.4628	0.4634	0.4651	0.4681	0.4655	0.4656
70	0.5358	0.5316	0.5323	0.5368	0.5332	0.5288	0.5331	0.5297
80	0.6119	0.6142	0.6107	0.6140	0.6062	0.6129	0.6152	0.6178
90	0.7389	0.7492	0.7417	0.7411	0.7479	0.7356	0.7380	0.7370

Table 3.4: Mean RMS height error for $\theta_{initial} = 0°$ to 105° values using baseline-weighted averaging.

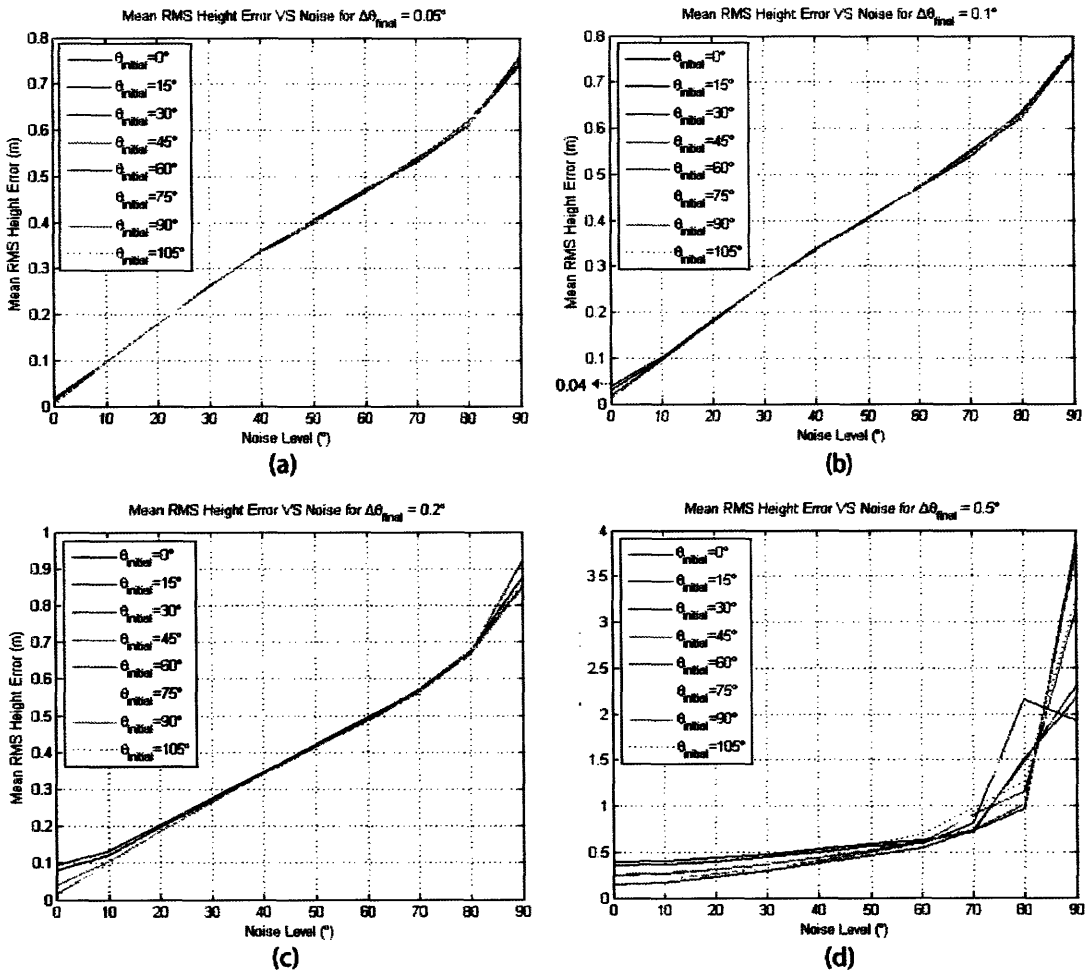

Figure 3-24: Mean RMS height error as a function of noise level for various $\theta_{initial}$ values with (a) $\Delta\theta_{final} = 0.05°$, (b) $\Delta\theta_{final} = 0.1°$, (c) $\Delta\theta_{final} = 0.2°$ and (d) $\Delta\theta_{final} = 0.5°$.

all noise levels to be $5.78 \times 10^{-3}m$.

Finally, the critical $\Delta\theta$ where breakdown of the above scheme occurs shall be defined. Figure 3-24 depict similar plots as before except that $\Delta\theta_{final}$ is increased from 0.05° in (a) to 0.5° in (d). As $\Delta\theta_{final}$ increases, the different plots of $\theta_{initial}$ begins to deviate from one another such that their RMS height errors become bigger, indicating a break down in the height retrieval process. As explained in earlier paragraphs, this is due to the approximations made when applying the B^2 weighting functions. Here, we defined $\Delta\theta_{critical}$ to be such that its mean RMS height error is less than a predefined tolerance level, e_{tol}, for all $\theta_{initial}$ values in the noiseless environment. If e_{tol} is chosen to be $4cm$, as in figure 3-24(b), then, $\Delta\theta_{critical} = 0.1°$. Using eq. 3.6, this implies that the terrain may be correctly retrieved up to a maximum cartwheel rotation speed which makes six complete turns of the wheel in one revolution of the constellation's orbit.

We shall now go on to examine the effects of cartwheel on the CCD process.

3.3 Coherent Change Detection with the Cartwheel

The setup to be used in this section is similar to that employed in figure 2-14, where the same two-slope terrain, trench-hole deformations and ideal coherence map are utilized. While three satellites coexist again in each pass, they are now placed in a circular cartwheel configuration instead, as described in section 3.1. Also, the separation between the cartwheel's reference point of pass one and two is $200m$. In this section, we would like to study the effects of the *constantly* rotating cartwheel on change detection of a snapshot of the imaged scene. As before, we shall compare the performance of the multilook coherence estimator, topography-corrected coherence estimator and wavelet transform-based coherence estimator, applied on the two-slope terrain. Here, the DEM needed for topography-corrected coherence estimator is retrieved from the three-satellite cartwheel, as explained in section 3.2.4, during the first pass.

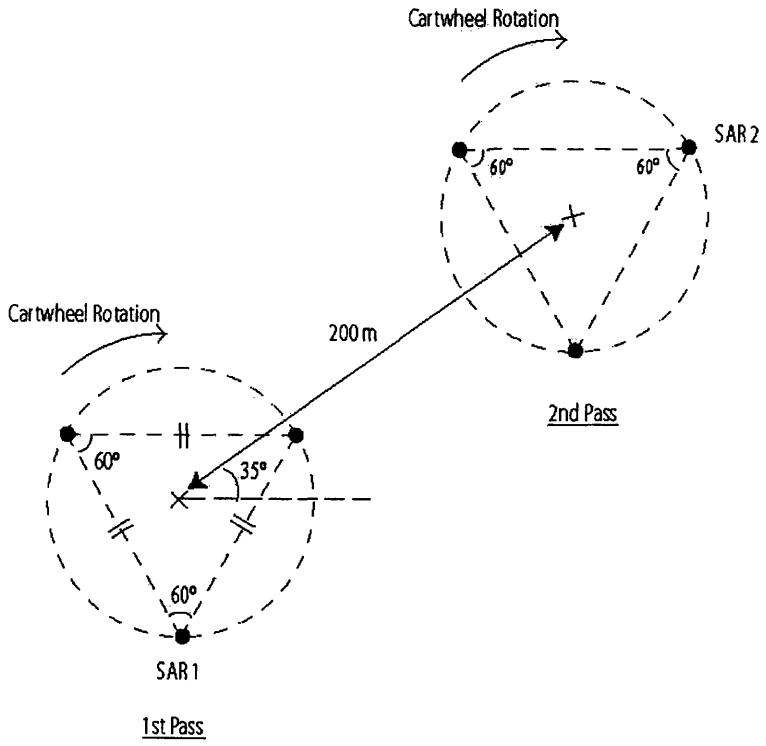

Figure 3-25: Satellite cartwheel setup for CCD with plane of the cartwheel modified for clarity.

Figure 3-25 illustrates the simulation setup of the satellite cartwheel used in CCD. The plane of both cartwheels have been rotated for clarity sake. Without loss of generality, SAR 1 of the first pass and SAR 2 of the second pass is used to form the

interferometric baseline for CCD. Of course, we could have chosen any other satellites in the first and second passes to form the baseline but since we are primarily interested in investigating the effects of the cartwheel on CCD here, such a choice would have sufficed. In addition, the cartwheels in both passes have the same start positions, $\theta_{initial}$, and final angle of rotation, $\Delta\theta_{final}$.

In the subsequent sections, we shall first assume a noiseless environment and fix $\theta_{initial}$ at 50° to examine the performance of change detection with respect to varying $\Delta\theta_{final}$. Performance of the various CCD methods is measure by the mean RMS coherence error. After that, CCD's performance in a noisy environment will be evaluated before finally, analyzing its performance as a function of $\theta_{initial}$. Note that in the realistic case, $\Delta\theta_{final} = 0.02°$ (see section 3.2.2) so that this becomes our primary value of interest.

3.3.1 Varying Angle of Rotation, $\Delta\theta_{final}$

In this section, we kept $\theta_{initial}$ fixed at 50° while assuming a noiseless environment. The coherence maps retrieved from the three approaches are illustrated in figure 3-26 with various value of $\Delta\theta_{final}$ at (a) 0.02°, (b) 0.1°, (c) 0.3°, (d) 0.4° and (e) 0.5°. Their corresponding RMS coherence errors are tabulated in table 3.5.

For small $\Delta\theta_{final} = 0.02°$ up to 0.4°, the coherence maps observed are very similar to those attained in figure 2-16(a), where the slope biasing effect showed up in the multi-look CCD while both topography-corrected and wavelet CCD are relatively unbiased by this effect. This implies that cartwheel CCD does work in the realistic case where $\Delta\theta_{final}$ is about 0.02°. However, for $\Delta\theta_{final} = 0.5°$ or greater, effects of the rotating cartwheel starts to kick in and the coherence losses in the unchanged portions of the imaged scene is so bad that they may be misinterpreted as scene-change induced low coherence values. These observations may be arrived by inspecting figure 3-26(e), where coherence values across the maps are generally low (< 0.6), irrespective of the actual scene changes.

One reason why CCD still works reasonably well despite a rotating cartwheel is due to the fact that the coherence value of a pixel is also computed based on the values of its neighboring pixels, via windowing as described in eq. 1.21 and 2.26. This may be considered as a form of averaging such that the distortions introduced by the cartwheel's rotation are partly eliminated, for small $\Delta\theta_{final} = 0.02°$ up to 0.4°.

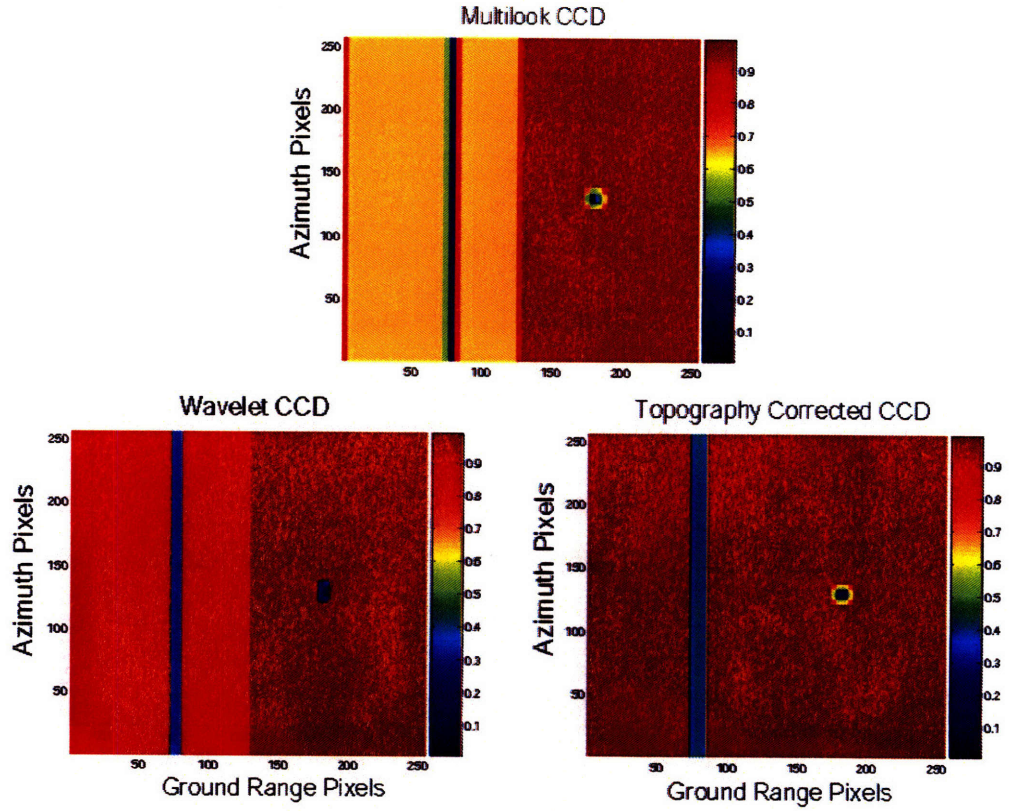
Multilook CCD
Azimuth Pixels
Wavelet CCD
Topography Corrected CCD
Azimuth Pixels
Azimuth Pixels
Ground Range Pixels
Ground Range Pixels

(a) 0.01°

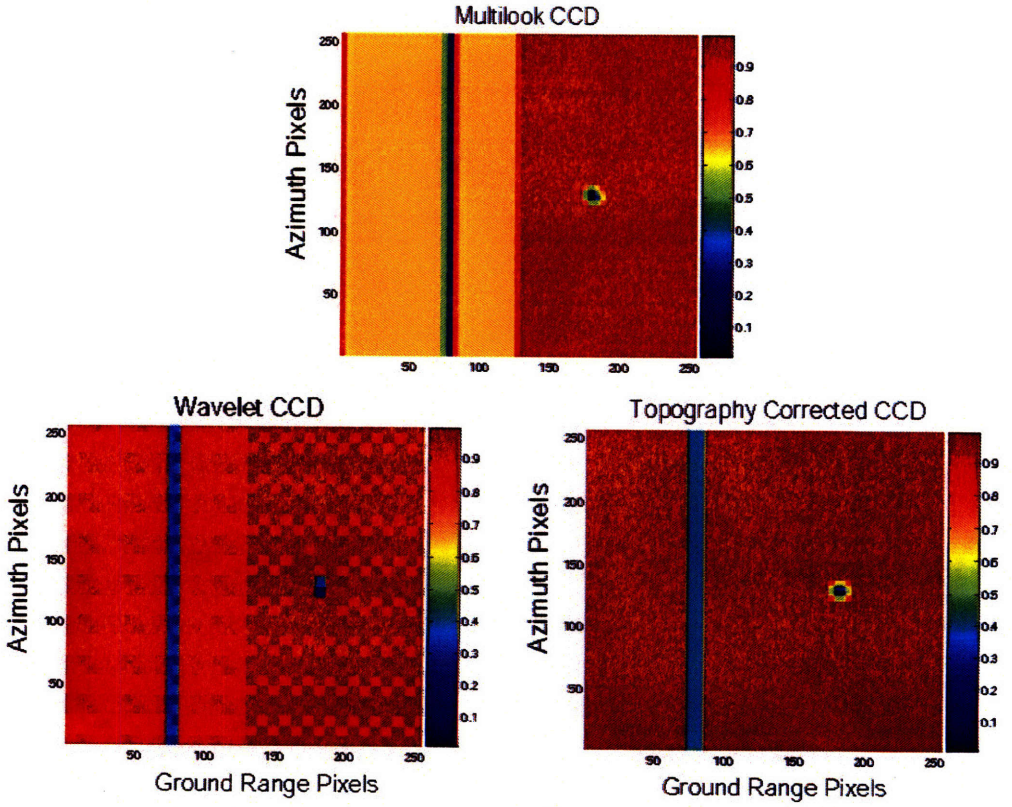
Multilook CCD
Azimuth Pixels
Wavelet CCD
Topography Corrected CCD
Azimuth Pixels
Azimuth Pixels
Ground Range Pixels
Ground Range Pixels

(b) 0.1°

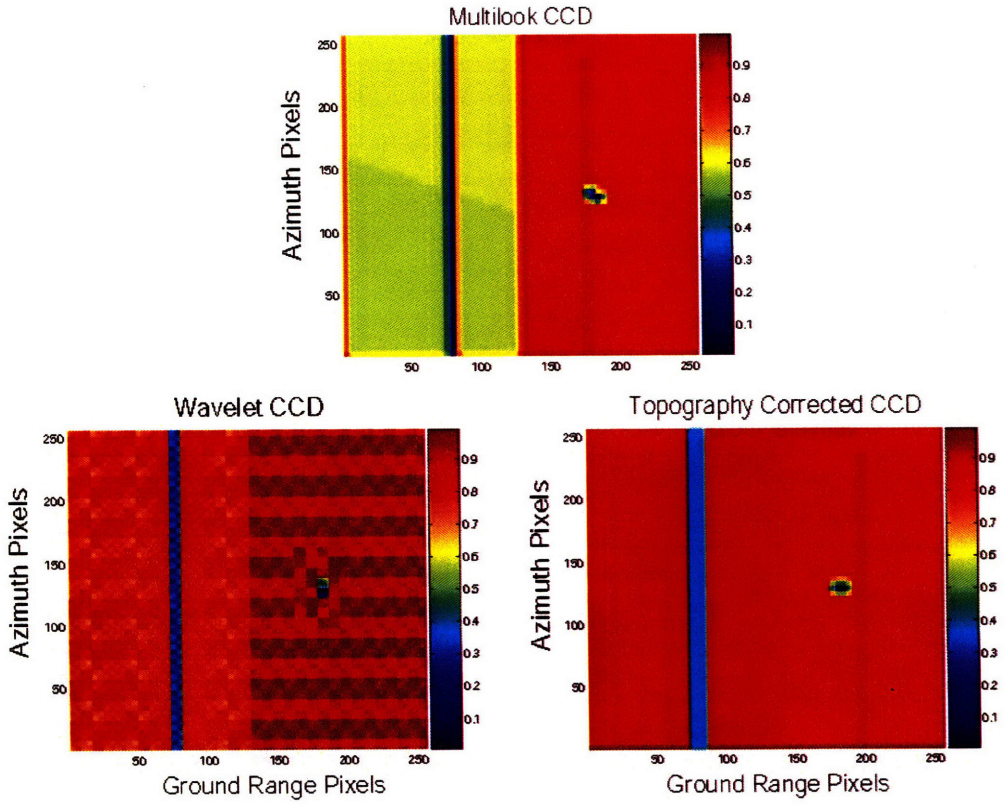
Multilook CCD
Azimuth Pixels
Wavelet CCD
Topography Corrected CCD
Azimuth Pixels
Azimuth Pixels
Ground Range Pixels
Ground Range Pixels

(c) 0.3°

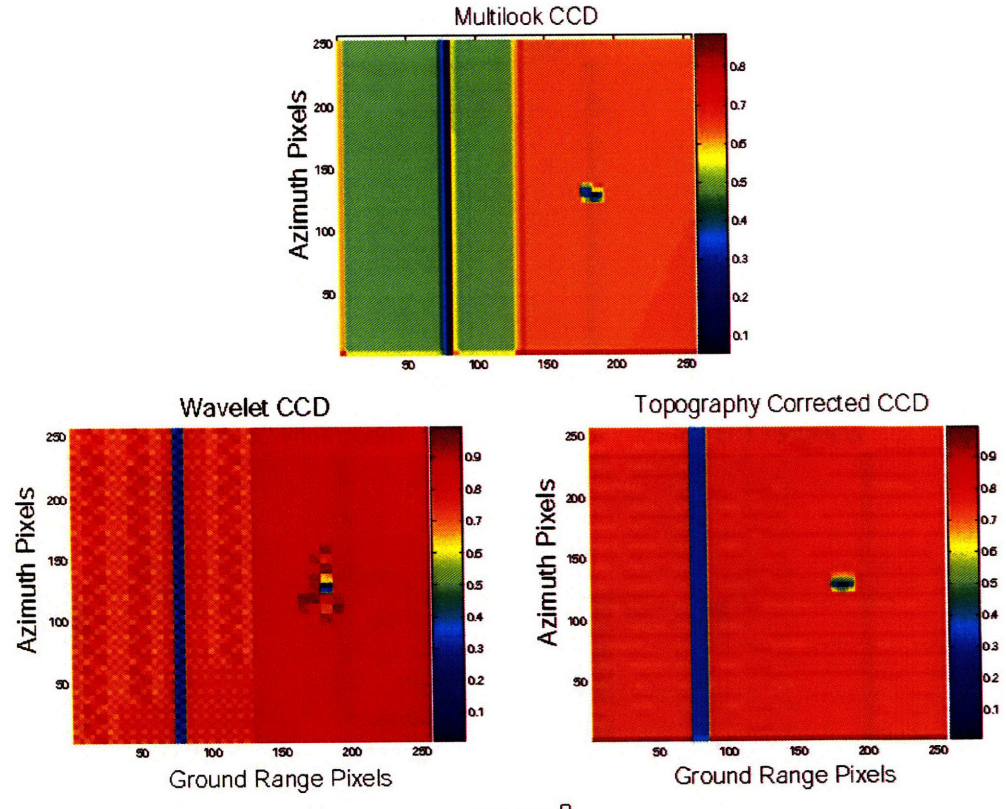
Multilook CCD
Azimuth Pixels
Wavelet CCD
Topography Corrected CCD
Azimuth Pixels
Azimuth Pixels
Ground Range Pixels
Ground Range Pixels

(d) 0.4°

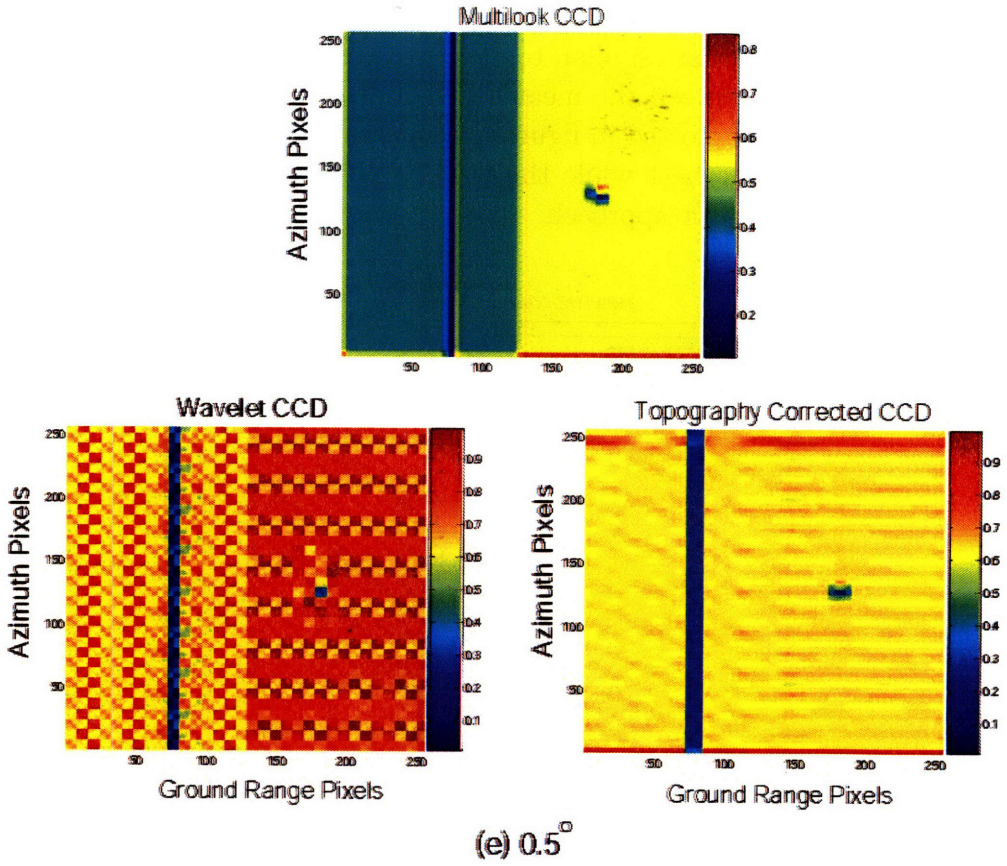

Figure 3-26: Coherence map for one simulation trial using multilook, topography-corrected and wavelet CCD with $\Delta\theta_{final}$ at (a) 0.02° (b) 0.1° (c) 0.3° (d) 0.4° (e) 0.5°.

	Coherence error		
$\Delta\theta_{final}$ (°)	**Multilook CCD**	**Wavelet CCD**	**Topography-Corrected CCD**
0.02	0.2307	0.1336	0.1191
0.1	0.2392	0.1475	0.1208
0.3	0.3168	0.1809	0.1834
0.4	0.3884	0.2057	0.2655
0.5	0.4791	0.2917	0.3710

Table 3.5: Coherence error for various CCD techniques as a function of $\Delta\theta_{final}$, applied on a three-satellite cartwheel.

3.3.2 Varying Noise Level

Now, we shall keep $\theta_{initial}$ fixed at 50° and $\Delta\theta_{final}$ fixed at 0.02°, while varying the noise level. This is somewhat similar to the investigations carried out in section 2.3.5. The relationship between the mean RMS coherence error and noise level for the three CCD methods is plotted in figure 3-27. As expected, topography-corrected CCD method performs the best while the wavelet CCD approach outperforms the multilook coherence estimator approach.

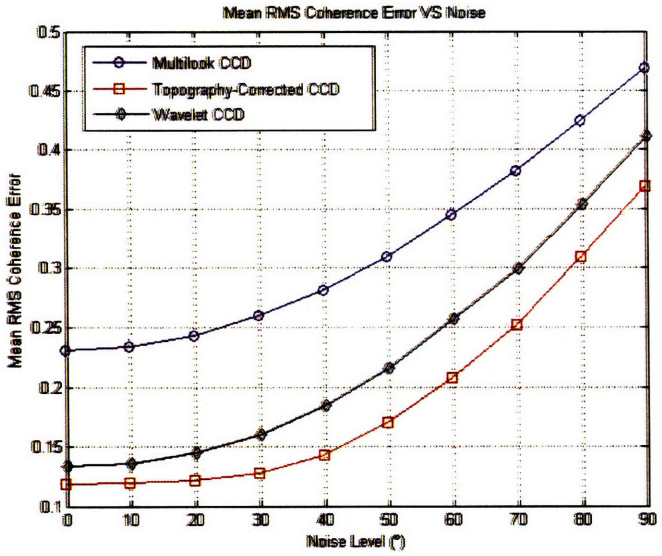

Figure 3-27: Mean RMS coherence error as a function of noise.

	Mean RMS coherence error		
Noise Level (°)	**Multilook CCD**	**Wavelet CCD**	**Topography-Corrected CCD**
0	0.2307	0.1336	0.1191
10	0.2342	0.1365	0.1192
20	0.2435	0.1455	0.1211
30	0.2601	0.1613	0.1274
40	0.2832	0.1839	0.1427
50	0.3098	0.2172	0.1690
60	0.3446	0.2563	0.2071
70	0.3821	0.3005	0.2509
80	0.4237	0.3538	0.3069
90	0.4704	0.4099	0.3711

Table 3.6: Mean RMS coherence error for various CCD techniques applied on a three-satellite cartwheel.

3.3.3 Varying Cartwheel's Start Position, $\theta_{initial}$

In this section, $\Delta\theta_{final}$ is kept fixed at 0.02° in a noiseless environment while $\theta_{initial}$ is varied, in retrieving the CCD with a constantly rotating cartwheel. A complete turn of the cartwheel is considered such that $\theta_{initial}$ changes from 0° to 345°. We shall first examine the relationship between the mean RMS coherence error and the cartwheel start position, $\theta_{initial}$. This is illustrated in figure 3-28.

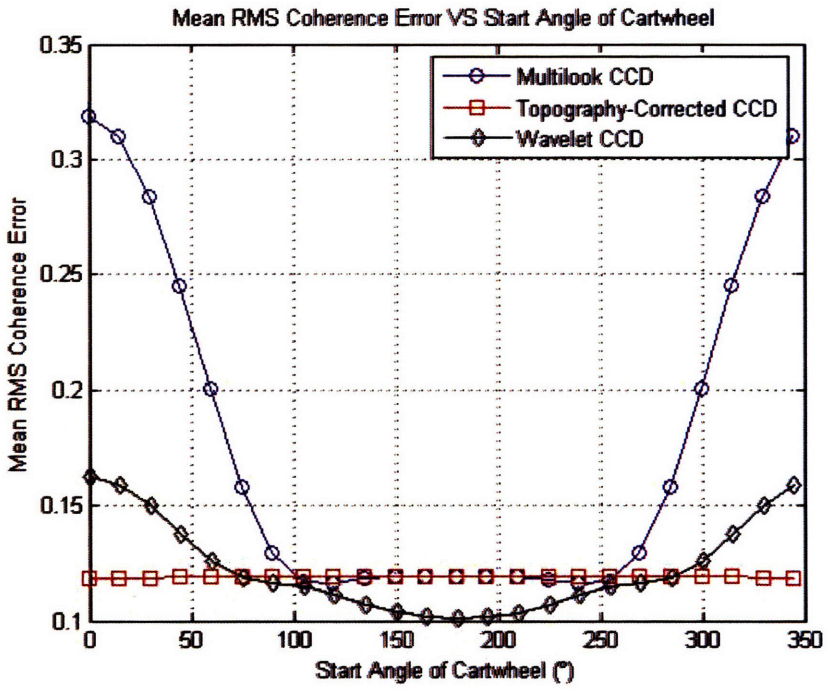

Figure 3-28: Mean RMS coherence error as a function of cartwheel start angle for multilook, topography-corrected and wavelet CCD.

From the figure above, it can be inferred that the topography-corrected CCD method is independent of the cartwheel's start position while both the multilook and wavelet CCD exhibits minimum errors at $\theta_{initial} = 180°$. As well, symmetry in the mean RMS coherence error is observed about this angle. In order to aid us in understanding this phenomenon, the interferometric baseline length formed between SAR 1 and SAR 2 of the two passes is plotted as a function of $\theta_{initial}$ in figure 3-29. Furthermore, reference to figure 2-11 has to be made. Data values of figures 3-28 and 3-29 are tabulated in table 3.7

Generally, the various cartwheel's start positions primarily affects the length of the interferometric baseline formed between SAR 1 and SAR 2 of each passes, and has a direct impact on coherence losses in CCD, as illustrated in figure 2-11. Ideally, we would like the baseline to be as short as possible such that when this baseline length

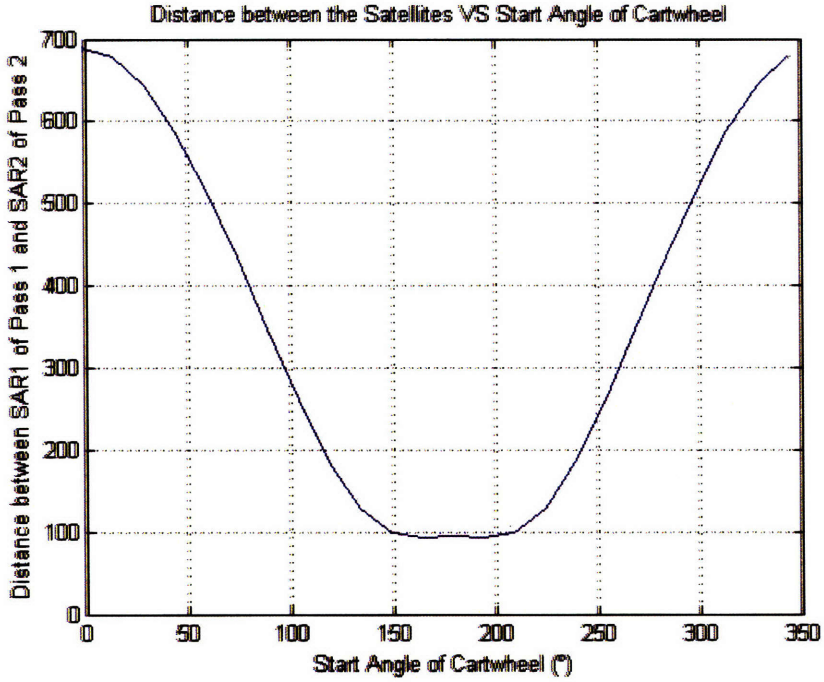

Figure 3-29: Distance between SAR 1 of the first pass and SAR 2 of the second pass as a function of cartwheel start angle for multilook, topography-corrected and wavelet CCD.

	Mean RMS coherence error			
Start Angle (°)	**Multilook CCD**	**Wavelet CCD**	**Topography-Corrected CCD**	**Distance between Satellites (m)**
0	0.3189	0.1623	0.1190	689.33
30	0.2841	0.1499	0.1189	643.05
60	0.2004	0.1260	0.1192	517.1
90	0.1294	0.1162	0.1192	347.1
120	0.1166	0.1116	0.1195	185.39
150	0.1193	0.1037	0.1196	99.332
180	0.1196	0.1009	0.1196	95.079
210	0.1193	0.1036	0.1195	99.352
240	0.1165	0.1115	0.1194	185.48
270	0.1295	0.1163	0.1191	347.22
300	0.2004	0.1261	0.1191	517.21
330	0.2841	0.1499	0.1188	643.11

Table 3.7: Coherence error for various CCD techniques and their corresponding satellites separation, applied on a three-satellite cartwheel.

becomes zero, $\rho_{spatial}$ of eq. 1.22 becomes one.

Mean RMS coherence errors of the topography-corrected CCD method in figure 3-28 remain a constant unaffected by $\theta_{initial}$ and hence, are independent of the baseline length between the passes as well. This is similar to the observation made in figure 2-11(a) where the terrain profile is compensated exactly in forming the coherence map. If the terrain variations are not totally compensated, then figure 2-11(b) and (c) tell us that coherence losses, which worsen with increasing baseline length, will occur. This is what was observed for the case of wavelet and multilook CCD in figures 3-28 and 3-29, where the two plots share very similar trends. As such, we conclude that the change detection of imaged scenes are dependent on the cartwheel's starting position, $\theta_{initial}$, unless knowledge of the DEM is available beforehand.

Furthermore, the coherence errors of the multilook CCD almost match that of the topography-corrected CCD at $\theta_{initial} = 180°$, as observed from table 3.7. This is the angle where the baseline length is minimum. The phenomenon can be explained by observing that there are two ways in achieving high $\rho_{spatial}$, unaffected by a non-zero baseline length (see section 2.3.1).

1. Accounting for terrain slope variations
2. Short interferometric baseline between the passes

Since eq. 1.21 and 2.26 are closely related except for the additional estimated topographic component, $\hat{\phi}_x$, by simultaneously satisfying the above two criterion, we would have made these equations equal. Hence, the match in coherence errors of the two methods are attained.

In this chapter, we have examined the effects of a constantly rotating circular cartwheel applied in taking a snapshot of an interferogram. Baseline-weighted averaging is found to be a necessary step for the correct and automated retrieval of heights. The proposed averaging scheme was found to work equally well for all cartwheel's orientations, as long as $\Delta\theta_{final}$ is $< 0.1°$. Cartwheel's impact on CCD was investigated as well and was found to detect scene changes correctly in the realistic case when the cartwheel rotate an angle of 0.02° within a snapshot of an interferogram. Furthermore, without prior knowledge of the DEM, CCD's performance was concluded to be dependent on the cartwheel's starting position when taking the snapshot of the scene.

Next, we shall look into the effects of possessing imperfect knowledge of the satellite positions and how such errors propagate into the height retrieval and CCD process.

Chapter 4

Satellite Positioning Errors

Due to instrumental noise effects, the satellite positioning data required for height inversion may be susceptible to errors. In previous chapters, we have highlighted the advantages brought about by the introduction of an additional third satellite. For instance, in the case of retrieving the terrain profile, three-satellite configuration enables the use of phase averaging and weighted height averaging techniques which are shown to outperform the heights retrieved from single baseline data. In CCD, a multi-baseline configuration allows for the application of topography-corrected coherence estimator, that compensates well for the slope biasing effects observed in the conventional multi-look coherence estimator.

Errors in the satellite positions propagate into unacceptably large misalignments in the retrieved terrain profiles, hence, greatly compromising any advantages in a three-satellite configuration that was discussed earlier. CCD applications are affected as well if the topography-corrected coherence estimator is adopted. We propose taking into account the satellite positioning errors in the height inversion process and attempt to retrieve the true satellite positions, without knowledge of any ground truths. In this chapter, we shall first discuss the implications and significance of such errors on the retrieved heights and CCD before looking into possible ways of rectifying them.

The setup used for analysis is the three-satellite non-collinear configuration model discussed in section 1.3.2. Here, we assume that at least one of the true satellite positions is known and so, may only be concerned with relative rather than absolute positioning errors. In this case, it suffices to fix one of the three satellite positions while introducing independent random errors to the other two. In figure 4-1, SAR 1 is fixed while both SAR 2 and SAR 3 deviates from their true positions (i.e. SAR 2_{error} and SAR 3_{error}) by amounts defined by r_2, θ_2, r_3 and θ_3 so that

$$SAR\ 2_{error} = [SAR\ 2_x + r_2 \cos\theta_2,\ \ SAR\ 2_z + r_2 \sin\theta_2] \tag{4.1}$$

$$SAR\ 3_{error} = [SAR\ 3_x + r_3 \cos\theta_3,\ \ SAR\ 3_z + r_3 \sin\theta_3] \tag{4.2}$$

where θ_i and r_i, with $\{i\} = \{1, 2\}$, represent independent random numbers uniformly distributed between $[-\pi, \pi)$ and $[0, r_{max}]$ respectively, with r_{max} being the maximum

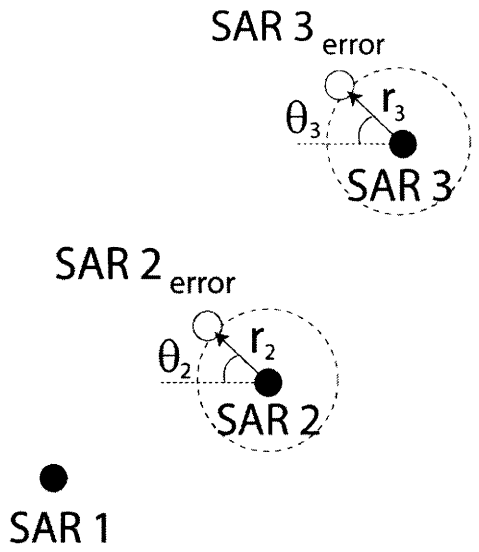

Figure 4-1: Errors in satellite positions, defined in terms of the magnitude r and phase θ, for a three-satellite non-collinear configuration.

magnitude of satellite position error.

Errors in these positions propagates into errors of the baseline length, the baseline elevation angle and the satellites' heights, resulting in retrieved height profiles that are vertically and horizontally displaced and tilted, as shall be discussed in the next section.

4.1 Impacts of Positioning Error on Height Retrieval

The height retrieval process represented by eq. 1.18 and eq. 1.19 are repeated below for easy reference, and for a more general case.

$$\theta = \alpha + \sin^{-1}\left(\frac{\delta}{B} + \frac{B}{2\rho} - \frac{\delta^2}{2B\rho}\right) \tag{4.3}$$

$$\Delta z = H - \rho\cos\theta \tag{4.4}$$

From these two equations, we again identify the retrieval parameters as the unwrapped interferogram, Φ, and its corresponding

- slant range, ρ
- look angle with respect to nadir, θ
- baseline, B
- baseline elevation angle, α

- satellite's height, H

If errors are introduced in the satellite positions, then B, α and H associated with interferogram ϕ will inevitably inherit these errors, leading to an incorrect θ and eventually, retrieved heights. We shall first examine the effects of having errors in each of B, α and H *separately*, on the retrieved terrain profiles.

4.1.1 Baseline Uncertainty and Satellite's Height Uncertainty

Wong [8] has already investigated the effects of baseline length errors, *ceteris paribus*, on the retrieved heights. It was shown that such errors resulted in vertical and horizontal (due to foreshortening correction) shifts of the terrain profiles. In particular, his thesis illustrated an example where a 2% error in baseline length resulted in vertical and horizontal shifts of hundreds of meters when the terrain's absolute height is only ten meters.

Errors in the satellite's height may be factored into eq. 4.4 such that the retrieved heights become vertically displaced.

4.1.2 Baseline Elevation Angle Uncertainty

We shall now examine the effects on the retrieved terrain profile when *only* the baseline elevation angle, α, contains error.

Let the true angle corresponding to the interferogram in question be α. In that case, the satellite position errors will introduce a fix deviation, $\Delta\alpha$, from the actual value such that

$$\alpha' = \alpha + \Delta\alpha \tag{4.5}$$

Eq. 4.3 is then modified to account for the error so that

$$\begin{aligned} \theta' &= \alpha + \sin^{-1}\left(\frac{\delta}{B} + \frac{B}{2\rho} - \frac{\delta^2}{2B\rho}\right) + \Delta\alpha \\ &= \theta + \Delta\alpha \end{aligned} \tag{4.6}$$

Both eq. 4.5 and eq. 4.6 illustrates how the errors in α propagates into errors in the look angle. Eq. 4.4 relates cosine of the look angle to retrieved heights. This is represented in eq. 4.7.

$$\Delta z \propto \cos(\theta') \tag{4.7}$$

We shall also define the first and second derivatives of eq. 4.7 where

$$\frac{d(\Delta z)}{d\theta'} \propto -\sin(\theta') \tag{4.8}$$

$$\frac{d^2(\Delta z)}{d(\theta')^2} \propto -\cos(\theta') \tag{4.9}$$

Next, we define θ_A as the look angle corresponding to the ground range pixels nearest nadir while θ_B as the look angle corresponding to the ground range pixels furthermost from nadir. Figure 4-2 illustrates these angles.

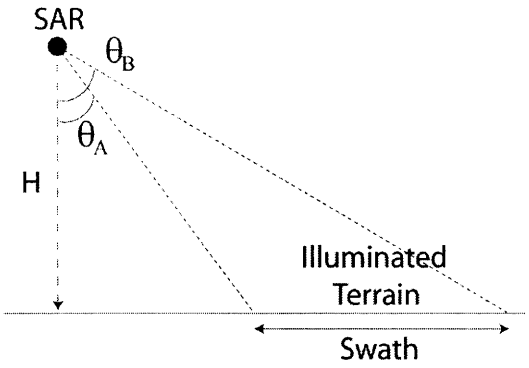

Figure 4-2: Satellite setup illustrating θ_A and θ_B.

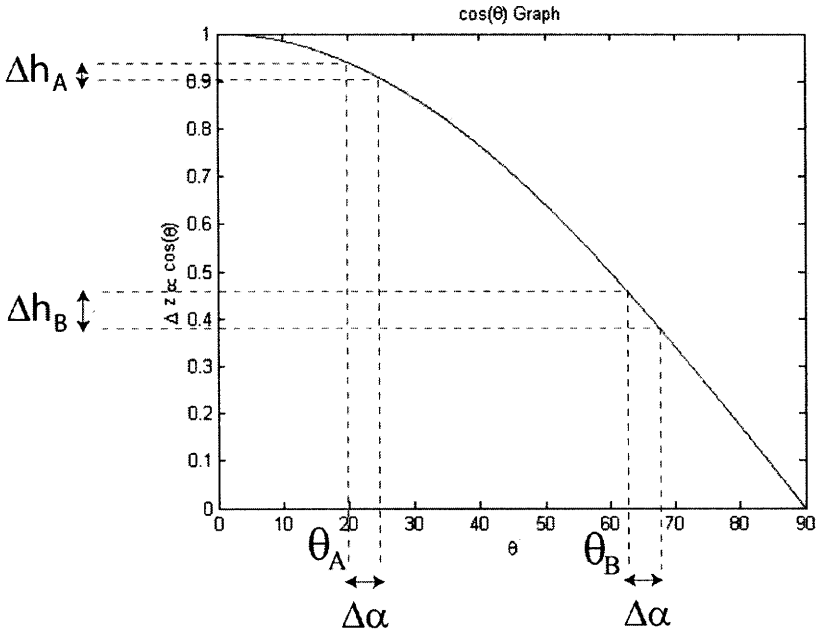

Figure 4-3: Plot of $\Delta z \propto \cos(\theta)$ together with amplified values of θ_A and θ_B.

Using the terrain model described in section 1.3.2, θ_A is $\sim$ 30.9638° and θ_B is $\sim$ 31.2996°. As a result, $|\theta_A - \theta_B| = 0.3358°$, which is small. Figure 4-3 shows the relationship of eq. 4.7. For illustration purpose, the values of θ_A and θ_B are exaggerated to bring out the distinction that $\theta_A < \theta_B$. Referring to figure 4-3, we now introduce an incremental error, $\Delta\alpha$, to the baseline elevation angle such that it becomes eq. 4.5, and then observe the corresponding change in the retrieved height at opposite ends (i.e. θ_A and θ_B) of the illuminated terrain. From the graph, it can

be deduced that for positive values of $\Delta\alpha$, h_A is decreased by Δh_A while h_B is decreased by Δh_B, with $\Delta h_A < \Delta h_B$. According to eq. 4.8, if we assumed $\Delta\alpha$ to be small, then, these changes in h_A and h_B are approximately linear with respect to $\Delta\alpha$. On the other hand, eq. 4.9 relates the magnitude of change in Δh_A and Δh_B to the difference in look angles, $|\theta_A - \theta_B|$. In particular, Δh changes linearly for small $|\theta_A - \theta_B| = 0.3358°$.

The actual retrieved heights, $\Delta z'$, affected by $\Delta\alpha$, and thus, Δh, may be represented as follows:

$$\Delta z' \propto \Delta z + \Delta h \tag{4.10}$$

Because the change in magnitude from Δh_A to Δh_B is approximately linear for small $|\theta_A - \theta_B|$, this leads to the conclusion that the retrieved heights, $\Delta z'$, becomes vertically displaced and *tilted* in the ground range direction. This finding agrees with simulation results where a flat terrain, upon introduction of errors in the baseline elevation angle, is observed to be vertically shifted and tilted, with a linear slope.

4.1.3 Satellite Positioning Uncertainty

Since errors in the satellite positions propagate into errors of the baseline length, elevation angle and satellite's height, we may deduced from earlier sections that, in general, such uncertainties combine to produce a retrieved terrain profile that is horizontally and vertically shifted, and linearly tilted. Simulation results verified this and showed that, in fact, large vertical shifts are the main contributor to the RMS errors in the retrieved heights. Hence, these errors may be greatly reduced by aligning the mean of the retrieved and displaced heights. However, we shall not make such an alignment correction in this chapter for the purpose of analyzing realistically the full impacts of the satellite position errors on retrieved topography.

In figure 4-4 and table 4.1, we analyze the effects of position errors in SAR 2 and SAR 3 with maximum magnitudes, r_{max}, ranging from $0cm$ to $10cm$ on the retrieved terrain. In this case, the mean of $N = 50$ simulation runs is considered and the mean RMS height error is computed as:

$$mean\ r.m.s\ error = \frac{1}{N}\sum_{k=1}^{N}\left(\sqrt{\frac{1}{ab}\sum_{i=1}^{a}\sum_{j=1}^{b}[(h_{ij}^{weighted\ averaging} - h_{ij}^{original})^2]}\right)_k \tag{4.11}$$

where $h_{ij}^{weighted\ averaging}$ is the retrieved heights susceptible to satellite positioning errors at the (i^{th}, j^{th}) pixel, after applying weighted height averaging, and $h_{ij}^{original}$ is the true terrain height at the (i^{th}, j^{th}) pixel.

The plot shows that the accuracy of the retrieved heights are very sensitive to the maximum magnitude of position errors, and that they are positively related. For instance, $2cm$ deviations in the positions of SAR 2 and SAR 3 results in mean height

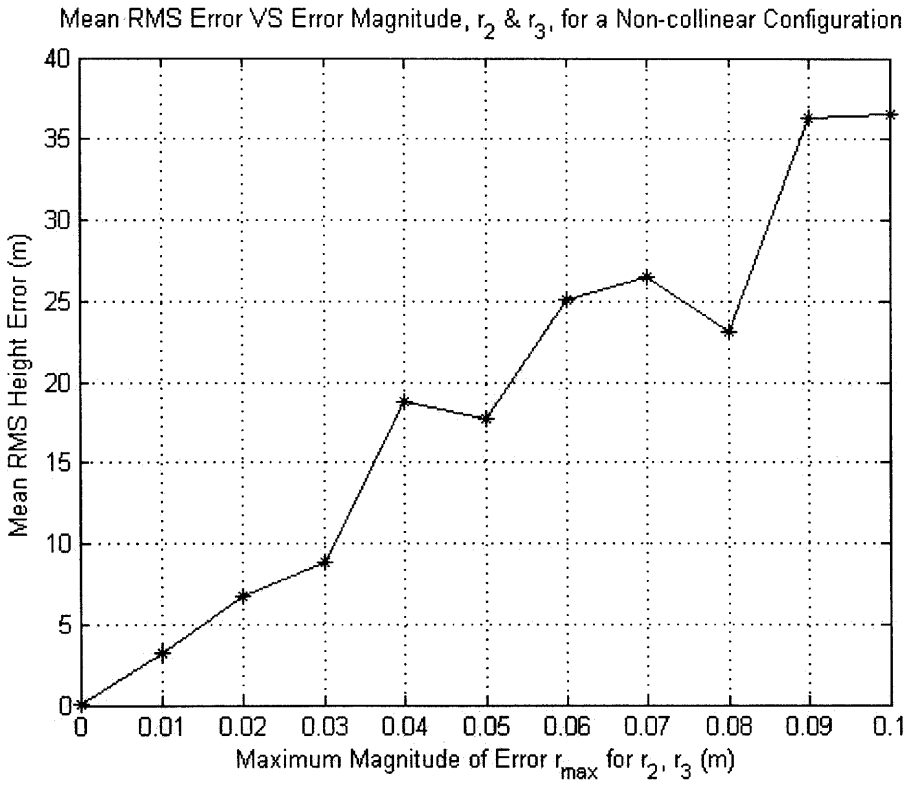

Figure 4-4: Mean RMS height error as a function of the maximum magnitude of error, r_{max}, applied on SAR 1 and SAR 2 (r_2 and r_3).

Maximum Magnitude of Satellite Position Error, r_2, r_3 (m)	**Mean RMS Coherence Error** (m)
0	7.756×10^{-8}
0.01	3.2579
0.02	6.7779
0.03	8.8438
0.04	18.720
0.05	17.665
0.06	25.089
0.07	26.527
0.08	23.092
0.09	36.275
0.10	36.516

Table 4.1: Mean RMS height error for varying maximum magnitudes of the satellite positions error, r_{max}, for r_2 and r_3.

errors of more than $5m$ while $10cm$ deviations propagate into mean height errors of $36m$. Such sensitivities in position errors implied that these errors must be accounted for in the height inversion process, which we will attempt in section 4.3.

4.2 Impacts of Positioning Error on CCD

In CCD, the phase data of satellites from each of the passes are combined using the multilook coherence estimator of eq. 1.21, repeated below for easy references:

$$|\rho| = \frac{\left|\sum_{m=1}^{M}\sum_{n=1}^{N} S_1(m,n)S_2^*(m,n)\right|}{\sqrt{\sum_{m=1}^{M}\sum_{n=1}^{N}|S_1(m,n)|^2 \sum_{m=1}^{M}\sum_{n=1}^{N}|S_2(m,n)|^2}} \tag{4.12}$$

It becomes obvious that multilook CCD is not affected by satellite positioning errors since satellite position data are not factored into the computations of the coherence map, as depicted in the above equations. Rather, only the co-registered phase data from each of the passes are required.

However, if we would like to compensate for the slope biasing effects inherent in the above method, then, the topography-corrected coherence estimator of eq. 2.26, repeated below for convenience, shall be utilized.

$$|\rho_{topo}| = \frac{\left|\sum_{m=1}^{M}\sum_{n=1}^{N} S_1(m,n)S_2^*(m,n)e^{-j\hat{\phi}_x(m,n)}\right|}{\sqrt{\sum_{m=1}^{M}\sum_{n=1}^{N}|S_1(m,n)|^2 \sum_{m=1}^{M}\sum_{n=1}^{N}|S_2(m,n)|^2}} \tag{4.13}$$

Applications of eq. 4.13 require the terrain profile ($\hat{\phi}_x$), which should be attained with a three-satellite configuration in order to avoid temporal decorrelation, as explained in section 1.5.2. However, the terrain profiles would have been distorted due to the presence of satellite position errors, discussed in the previous section. We shall next examine the effects of position errors on the topography-corrected coherence estimator.

The simulation model used is that shown in figure 2-14, where the same terrain, deformations and ideal coherence map are considered. The satellite setup is shown in figure 4-5, where positioning errors have been applied to SAR 2 and SAR 3. Unlike the errors introduced in figure 4-1, we will fix both θ_2 and θ_3 to be 180° for simplicity, such that their position errors are only dependent on the magnitude r_{test}, as shown in the figure. Moreover, r_{test} is now non-random and represents the *absolute* magnitude

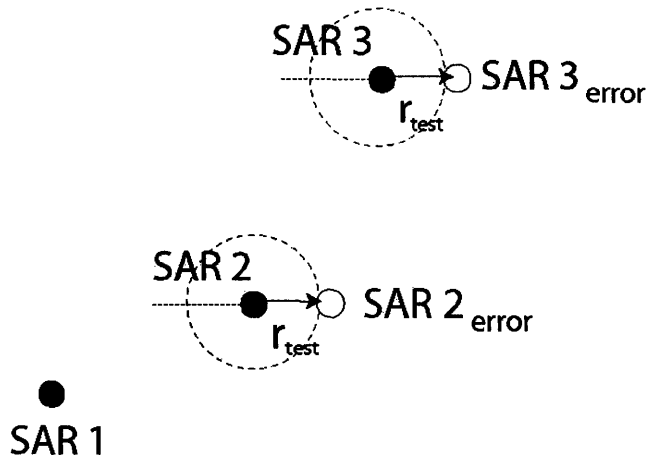

Figure 4-5: Errors in satellite positions, for a three-satellite configuration applied on the topography-corrected coherence estimator.

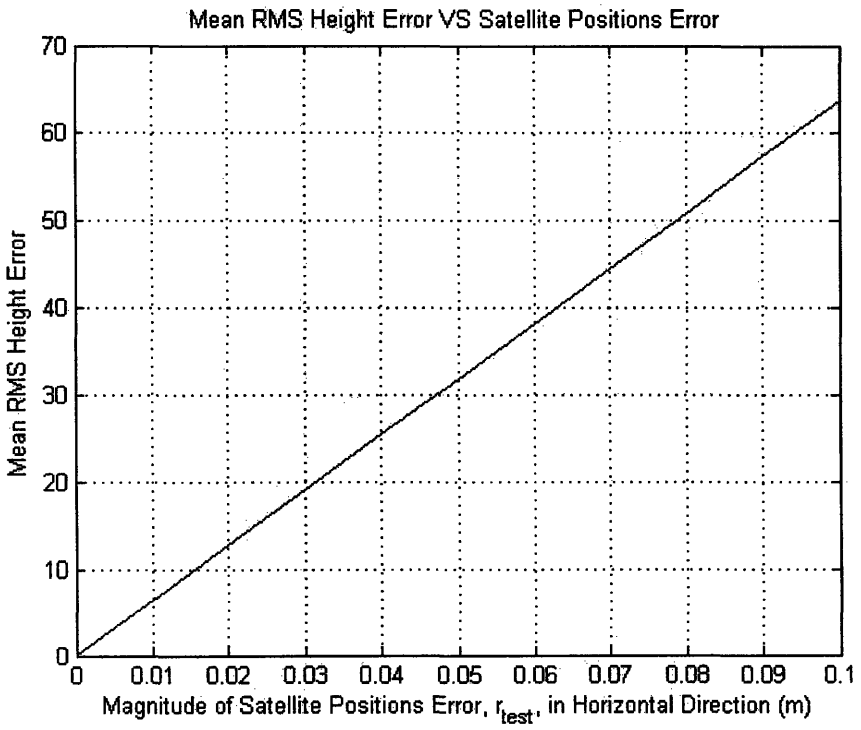

Figure 4-6: Mean RMS height error as a function of the magnitude of satellite positions error, r_{test}, in a noiseless environment.

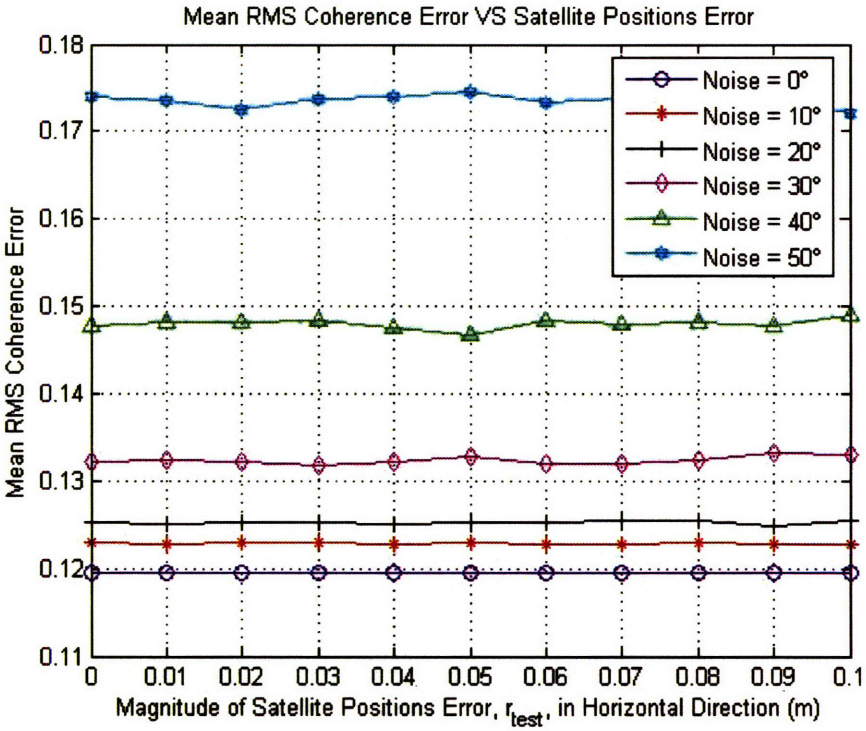

Figure 4-7: Mean RMS coherence error as a function of the magnitude of satellite positions error, r_{test}, for noise level = 0°, 10°, 20°, 30°, 40° and 50°.

	Mean RMS Coherence Error (m)					
Satellite Position Error, r_{test} (m)	**Noise Level** = 0°	10°	20°	30°	40°	50°
0	0.1194	0.1231	0.1252	0.1322	0.1477	0.1739
0.01	0.1194	0.1228	0.1251	0.1323	0.1482	0.1735
0.02	0.1194	0.1230	0.1252	0.1323	0.1481	0.1725
0.03	0.1194	0.1230	0.1253	0.1317	0.1483	0.1737
0.04	0.1194	0.1228	0.1251	0.1323	0.1476	0.1740
0.05	0.1194	0.1231	0.1253	0.1328	0.1467	0.1746
0.06	0.1194	0.1229	0.1253	0.1320	0.1483	0.1733
0.07	0.1194	0.1229	0.1254	0.1319	0.1481	0.1738
0.08	0.1194	0.1231	0.1255	0.1324	0.1482	0.1741
0.09	0.1194	0.1229	0.1249	0.1332	0.1478	0.1736
0.10	0.1194	0.1228	0.1255	0.1331	0.1491	0.1721

Table 4.2: Mean RMS coherence error as a function of noise levels for varying magnitudes of the satellite positions error, r_{test}.

of errors instead of the *maximum* magnitude of the positioning errors defined earlier.

A plot of the mean RMS coherence error as a function of the magnitude of satellite positions error, r_{test}, for varying noise levels is illustrated in figure 4-7. The data for the plot is tabulated in table 4.2. At each noise level from 0° to 50°, the mean coherence errors remain relatively unchanged as r_{test} vary from $0cm$ to $10cm$, even when the terrain profile, which is used to determine $\hat{\phi}_x$ in eq. 4.13, contains RMS height error of up to $60m$. The plot of mean RMS height error as a function of r_{test} is shown in figure 4-6. Note that both figure 4-4 and 4-6 exhibits the same general trend but the mean RMS height error of the latter is higher, ranging from $0m$ to $60m$ for position errors with magnitudes varying between $0cm$ and $10cm$, as compared to a height error range of $0m$ to $36m$ in the former. This is because the magnitudes of the satellite position errors on the horizontal axis represent the *absolute* deviations in the latter while those in the former represent only the *maximum* possible deviations, and may not necessarily take up these values.

The observations made in figures 4-6 and 4-7 may be explained by more closely examining the estimated topographic component, $\hat{\phi}_x$. Firstly, it should be pointed out that the retrieved heights which are susceptible to positioning errors, are distorted primarily due to huge vertical displacements, as pointed out in section 4.1.3. In other words, these terrain profiles, though slightly tilted, closely resembles that of the original terrain, except for some vertical shifts. As well, it was noted that $\hat{\phi}_x$ in eq. 4.13 contains only information of the local terrain variations rather than information about the absolute terrain profile since it represents a phase term wrapped around $[-\pi, \pi)$. Hence, in computing $\hat{\phi}_x$ from the vertically distorted retrieved terrain, minimal errors are introduced since the local terrain characteristics are still well preserved in these terrain profiles.

From the results obtained above, it became clear that satellite position errors does not affect CCD applications as much as they do to height retrieval.

4.3 Satellite Position Retrieval without Ground Truths

In this section, we shall discuss the methods adopted in attempting to retrieve the correct satellite positions, without prior knowledge of any ground truths. If ground truth are available, then retrieval of the positioning data will be trivial. For instance, Zebker *et al.* [15] states that the positioning errors may be rectified if two ground truths is known, i.e. the shifts and tilt of the topography described in section 4.3 may be undone. Nonetheless, in practice, multiple ground truth points may not be available and it is more realistic to assume the scenario of no ground truths.

4.3.1 Satellite Position Retrieval Methodology

Since no ground truth points are available, we seek to search for the correct satellite positions by minimization of some proposed cost functions. The following three cost functions have been implemented:

$$f(B_{12}, \alpha_{12}, B_{13}, \alpha_{13}) = \sqrt{\frac{1}{ab}\sum_{i=1}^{a}\sum_{j=1}^{b}[(h_{12} - h_{13})^2]} \tag{4.14}$$

$$f(x_2, z_2, x_3, z_3) = \sqrt{\frac{1}{ab}\sum_{i=1}^{a}\sum_{j=1}^{b}[(h_{12} - h_{13})^2 + (h_{12} - h_{23})^2 + (h_{13} - h_{23})^2]} \tag{4.15}$$

$$\begin{aligned} f(x_2, z_2, x_3, z_3) \;=\; & \sqrt{(\frac{1}{ab}\sum_{i=1}^{a}\sum_{j=1}^{b}[(h_{12} - h_{13})^2 + (h_{12} - h_{23})^2 + (h_{13} - h_{23})^2 + \\ & + (\Delta x_1 - \Delta x_2)^2 + (\Delta x_1 - \Delta x_3)^2 + (\Delta x_2 - \Delta x_3)^2])} \end{aligned} \tag{4.16}$$

where h_{pq} is the height retrieved from interferogram ϕ_{pq} of size $a \times b$, with $\{p, q\} = \{1, 2, 3\}, p \neq q$. Δx_s is the ground range corresponding to satellite s. All three equations made used of the fact that if no satellite positioning errors exist, then, the retrieved heights from the three interferograms must match, returning the correct terrain profile. In other words, the functions $f(.)$ are minimum (i.e. RMS of the heights differences equal zero), at least locally, when the true satellite positions are detected. Parameters inside the brackets, (.) of $f(.)$, are values we search for in minimizing the cost functions.

Eq. 4.14 only made use of h_{12} and h_{13} so that H in eq. 4.4 has no uncertainty. In this case, we can make use of eq. 4.3 and eq. 4.4 directly to search for B_{12}, α_{12}, B_{13} and α_{13} that minimizes the cost function. With SAR 1's position known, we would then be able to deduce the correct positions of SAR 2 and SAR 3.

In figure 4-8 and 4-9, the one dimensional cost function of eq. 4.14 is plotted against position errors of SAR 3 in the horizontal and vertical directions respectively, as part of the forward problem. A setup similar to that in figure 4-1 is considered. By introducing $[-10cm, 10cm]$ horizontal and vertical errors separately to SAR 3 only in both figures, it can be observed that a minimum height error point indeed exists when no errors in the satellite positions are introduced.

In eq. 4.15, all three available retrieved height profiles are made used in minimizing the cost function and the true satellites' positions, (x_2, z_2) of SAR 2 and (x_3, z_3) of SAR 3, are searched for directly in the two dimensional along-track plane. In

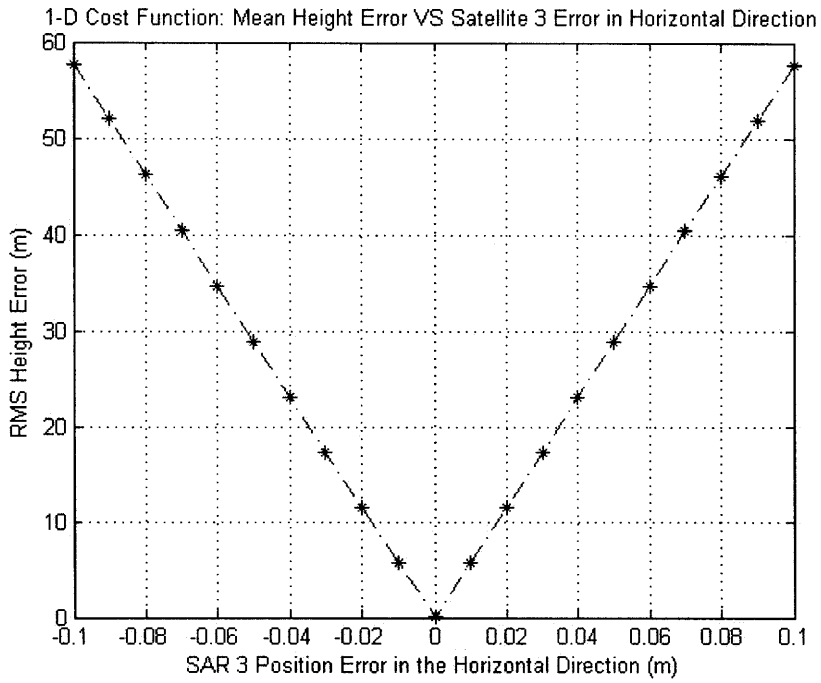

Figure 4-8: One dimensional cost function of the RMS height error plotted against position error of SAR 3 in the horizontal direction.

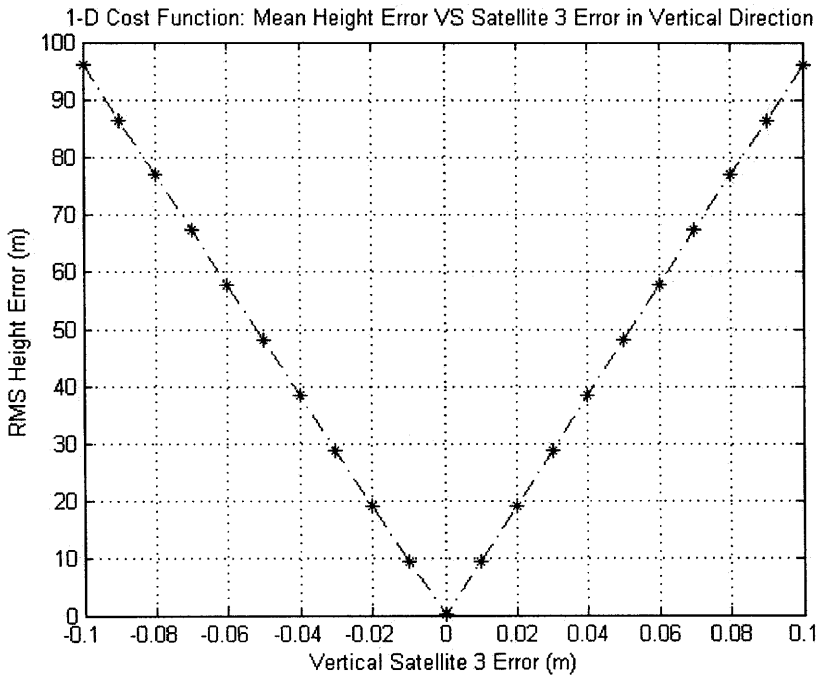

Figure 4-9: One dimensional cost function of the RMS height error plotted against position error of SAR 3 in the vertical direction.

implementation, the height retrieval equations 4.3 and 4.4 are modified such that

$$B_{12} = \sqrt{(x_2^{error} - x_1)^2 + (z_2^{error} - z_1)^2} \tag{4.17}$$

$$\alpha_{12} = \tan^{-1}\left(\frac{z_2^{error} - z_1}{x_2^{error} - x_1}\right) \tag{4.18}$$

so that $x^{error} = x$ and $z^{error} = z$ when the cost functions are eventually minimized. x^{error} and z^{error} are the original error-corrupted satellite positions.

Eq. 4.16 is an extension of eq. 4.15 such that the ground range positions of the retrieved heights, Δx, which is susceptible to foreshortening correction errors, are taken into account as well. In simulations, Δx is calculated as $\rho \sin(\theta)$. It was found that this cost function returns the most accurate satellite positions in a noiseless environment.

4.3.2 Simulation Results

We start off working in a noiseless environment with a flat test terrain, utilizing the setup illustrated in figure 4-1. Using eq. 4.16, the solutions that minimize the cost function are retrieved with Matlab's *fminsearch* function. The topography is then recalculated using these returned solutions of the *fminsearch* function (i.e. retrieved satellites' positions), in order to compare the improvement in accuracy attained upon conducting the positioning corrections. As well, the new errors of the corrected satellite positions are computed and compared directly with that of the original position errors. The results are plotted and tabulated in figure 4-10 and table 4.3

We can observe from figure 4-10 that by setting the *maximum* error magnitude, r_2 and r_3 of figure 4-1, to be $2.5cm$ or less, we ensured that the retrieved satellite positions of SAR 2 and SAR 3 deviate from the true positions by amounts less than the original errors introduced. For instance, with r_2 and r_3 set to $2cm$, the solutions returned by the *fminsearch* carried errors of about $1cm$ for both satellites. In fact, the topographies retrieved with these new positions were observed to follow closely the original flat terrain, with RMS height errors of the order $\sim 10^{-4}m$. This is a great reduction from having RMS height errors of up to $60m$ when no positioning corrections are applied.

If the errors introduced are such that $r > 2.5cm$, then, the searched satellite positions returned by Matlab are no longer closer to the true values than the initial deviations introduced. In that case, the cost functions minimization approach may seem to have failed to locate the true satellite positions. However, local observations of the cost functions about the true satellite positions, within $\pm 10cm$, showed that an absolute minimum point with value $\sim 10^{-7}$ indeed exist at the location of the true positions. In fact, locally around this minimum point, it was found that solutions with function values of the same order exist, making the minimum point less distinct. Despite reducing the termination tolerance criteria of the search process, Matlab's *fminsearch*

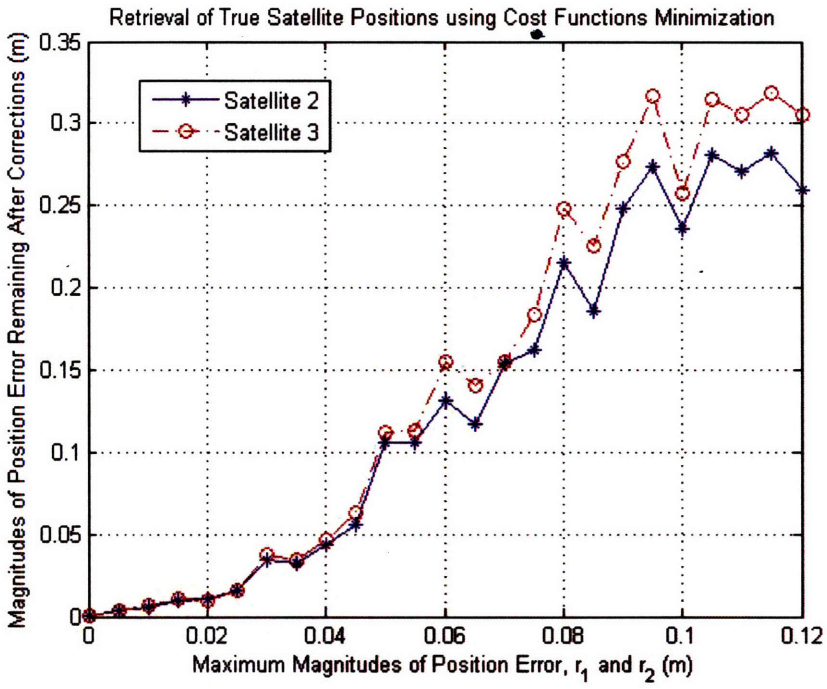

Figure 4-10: Maximum magnitudes of the original satellite position error, r_1 and r_2, compared against the new position errors after positioning corrections.

	Satellite Position Error after Corrections (m)	
Original Satellite Position Error, r_1, r_2 (m)	**Satellite 1**	**Satellite 2**
0	1.4761×10^7	1.8229×10^7
0.01	0.005565	0.006756
0.02	0.01064	0.009997
0.03	0.03447	0.03779
0.04	0.04400	0.04656
0.05	0.1061	0.1119
0.06	0.1318	0.1546
0.07	0.1543	0.1552
0.08	0.2157	0.2480
0.09	0.2485	0.2768
0.10	0.2360	0.2578
0.11	0.2710	0.3055
0.12	0.2597	0.3052

Table 4.3: Retrieval of true satellite positions using cost functions minimization techniques.

seems unable to detect this slight difference in function values, and hence, partly explaining the incompetence of the cost functions minimization approach in such a situation. For instance, introducing an error with maximum magnitude $6cm$ results in positioning errors of $\sim 14cm$ in the retrieved solution. Yet, the RMS height error using the worse-off satellite positions is still small, $\sim 10^{-3}$.

With the introduction of noise, the cost functions minimization approach return satellite positions that deviate greatly from the true values. Again, evaluation of the cost function in eq. 4.16 verified the existence of a local minimum at the true satellites' positions. However, *fminsearch* converges away from this minimum towards another local minimum further away.

4.3.3 Proposed Search Algorithms

Since the primary concern in this thesis is in analyzing the impacts of satellite positioning errors on the height retrieval and CCD processes, we shall not go into the details of compensating for the position errors in a noisy environment. Nonetheless, the following observations and suggestions are made.

In lieu of the observations made in simulations, it becomes obvious that an alternate search algorithm is critical in ensuring the success of the cost functions minimization approach described in section 4.3.1. In particular, the search algorithm must be sensitive to small differences in function values and should only do a local, rather than global, search for the desired solutions.

One suggested approach is as follows: Due to the *local* nature of such a search, it makes sense to divide the four-dimensional satellites' positions space, containing $(x_2^{error}, z_2^{error})$ and $(x_3^{error}, z_3^{error})$, into segments and manually search through each segment to find the one that returns the least value. After which, this newly identified segment is again divided up and a similar search for the next segment with the smallest value is applied. The process goes on till the segments become small enough to approximate satellites' positions. Such a search approach ensures that the solutions stay within the vicinity of the local minimum that corresponds to the true positions. As well, small differences of the cost function values, up to Matlab's precision of 10^{-16}, may be detected. Nonetheless, segmentation of a four dimensional space may prove to be a challenge.

In this chapter, we have analyzed how small errors in the satellite positions propagates into unacceptably large errors in the retrieved heights. In CCD applications, it was shown that the effects of satellite position errors is minimal since in this case, only the local terrain profile rather than the absolute terrain matters. As well, attempts are made to account for these errors without knowledge of any ground truths. More accurate satellite positions may be retrieved in a noise-free environment if the original position errors are less than $2.5cm$. Suggestions on how modifications to the current search algorithms may be made in order to enhance the satellite position retrieval

process to account for larger errors are also raised.

Chapter 5

Conclusion

In this thesis, we deal primarily with the multi-baseline SAR configuration utilizing three satellites. Two applications of InSAR, multi-baseline height retrieval and multi-baseline compensation of CCD's slope biasing effects, are first examined in details. The three-satellite setup is then related to a realistic cartwheel configuration, where the resultant errors introduced to the height retrieval and CCD process, due to the constant cartwheel rotation, are analyzed. As well, errors in satellites' positions are introduced and their impacts on height retrieval and CCD are studied. The thesis started off with the introduction of the simulation test model as well as the general height retrieval and CCD process.

In chapter 2, we first look at the multi-baseline height retrieval technique before directing our attention to CCD applications. Phase averaging technique, a novel contribution of the thesis, has been successfully applied to the three-satellite non-collinear configuration and is shown to perform better than data averaging, in terms of the mean RMS height error. Weighted phase averaging technique, though expected to outperform phase averaging using only two satellite data, break down in the non-collinear setup. As well, the single height method is shown to be more robust to varying noise levels than the single interferogram method. The ability to combine the multi-baseline data into one, such that it may be perceived as coming from only a pair of satellites, allows the application of the conventional two-satellite height inversion process without need for excessive modifications. At the same time, this approach returns more accurate results than just using data from each of the three possible satellite pairs.

Next, ways of compensating for coherence losses due to terrain slopes and inexact satellite repeat tracks are identified. These losses introduce ambiguities in the interpretations of low or medium coherence values: if they represent a scene change or simply an undulating terrain. Solutions to this issue include accounting for the topographic phase variations via prior knowledge of the DEM or a distinctive approach in the wavelet domain. While the latter is shown to produce a map with higher spatial resolutions, the former returns the best overall performance in CCD, in terms of mean RMS coherence error, and requires a multi-baseline satellite configuration for

accurate retrieval of the DEM.

In chapter 3, we examined the effects of a constantly rotating circular cartwheel applied in taking a snapshot of an interferogram. Baseline-weighted averaging is found to be a necessary step for the correct and automated retrieval of heights. The proposed averaging scheme was found to work equally well for all cartwheel's orientations, as long as $\Delta\theta_{final}$ is $< 0.1°$. Cartwheel's impact on CCD was investigated as well and was found to detect scene changes correctly in the realistic case when the cartwheel rotate an angle of $0.02°$ within a snapshot of an interferogram. Furthermore, without prior knowledge of the DEM, CCD's performance was concluded to be dependent on the cartwheel's starting position when taking the snapshot of the scene.

Lastly, satellite positioning errors due to instrumental noise effects are introduced in chapter 4 where the implications and significance of such errors on the retrieved heights and CCD are discussed. In CCD applications, it was shown that the effects of satellite position errors is minimal since in this case, only the local terrain profile rather than the absolute terrain matters. However, in height retrieval, small errors in the positions propagate into unacceptably large misalignments. Attempts are also made to account for these errors without knowledge of any ground truths, making use of some cost minimization functions.

Appendix A

Cartwheel's Orientation

The orientations of the cartwheel at 15° increments of the rotation angle, θ, from 0° to 360° are depicted in this appendix. Due to the cartwheel's symmetry, it turns out that satellite positions are repeated every 120°. Hence, in analysis, it suffices to only examine the rotation from $\theta_{initial} = 0°$ to 120°.

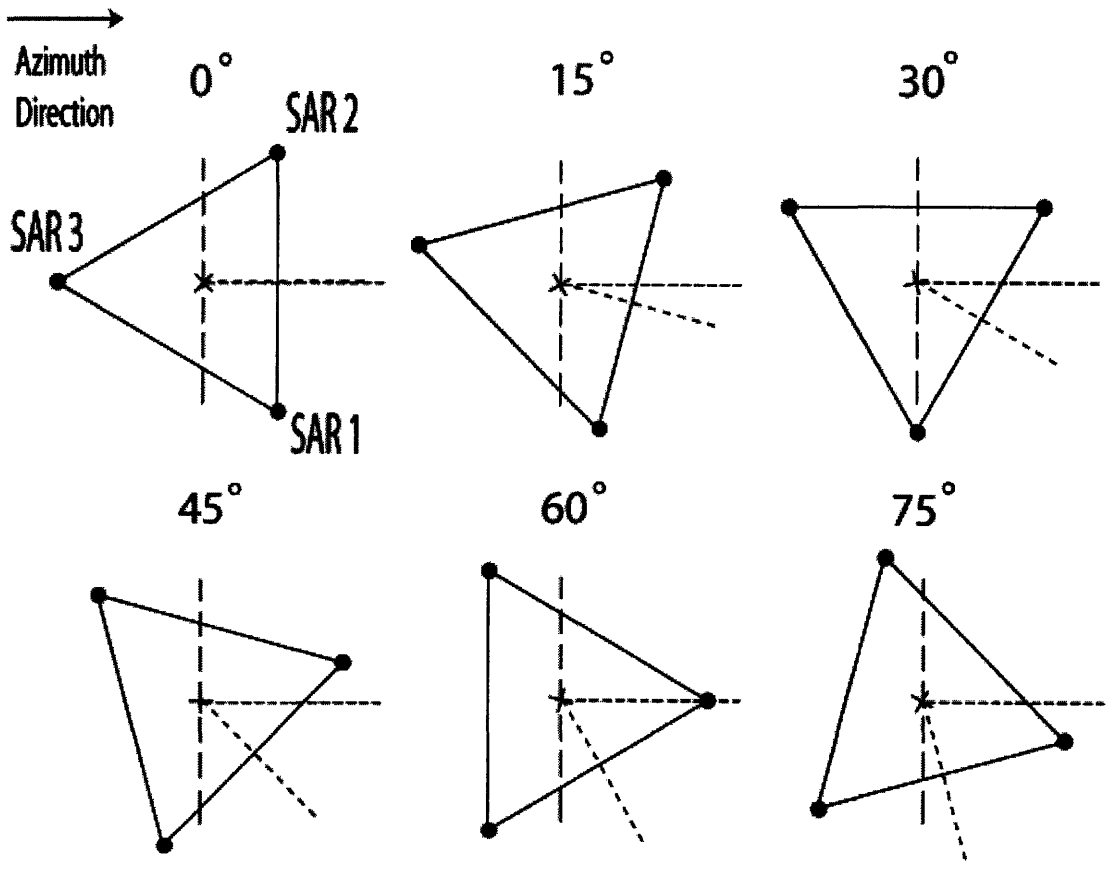

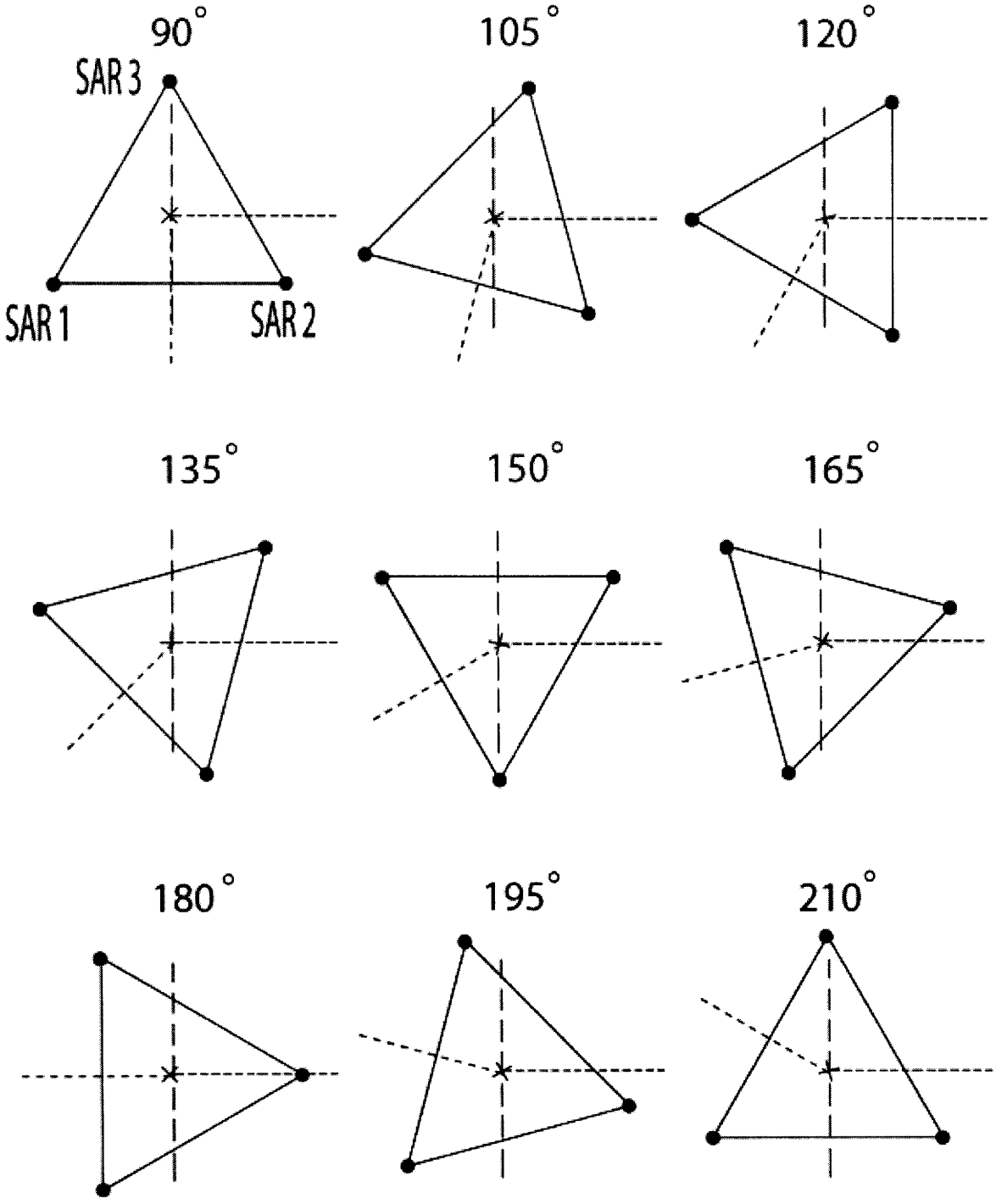
90°
SAR 3
SAR 1
SAR 2
105°
120°
135°
150°
165°
180°
195°
210°

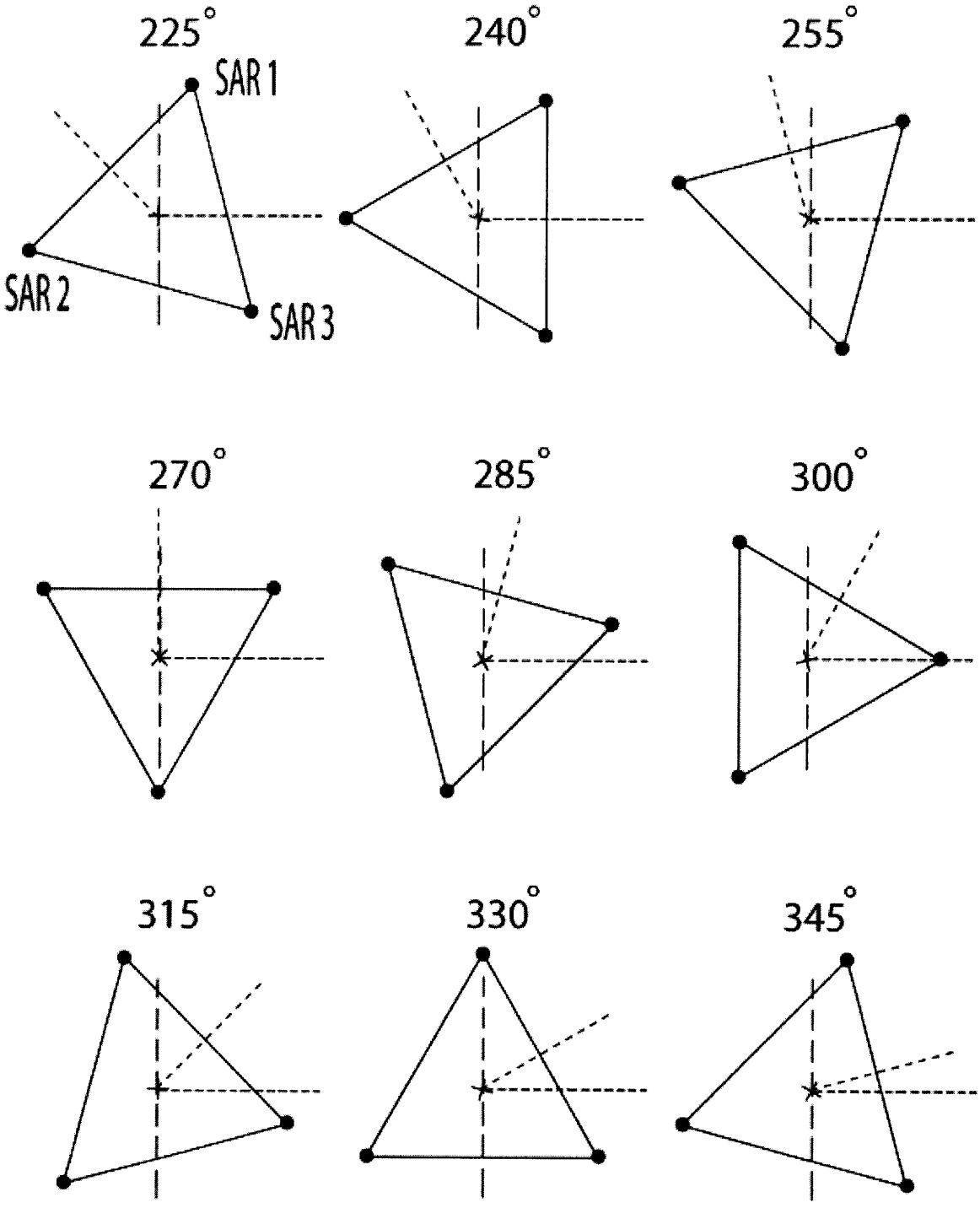
225°
SAR 1
SAR 2
SAR 3
240°
255°
270°
285°
300°
315°
330°
345°

Bibliography

[1] P. A. Rosen, S. Hensley. I. R. Joughin, F. K. Li, S. N. Madsen, E. Rodriguez, and R. M. Goldstein, "Synthetic aperture radar interferometry," *Proc. IEEE (Invited Paper)*, vol. 88, no. 3, pp. 333-382, Mar. 2000.

[2] L. C. Graham, "Synthetic inteferoemtric radar for topographic mapping," *Proc. IEEE*, vol. 62, pp. 763-768, Jun. 1974.

[3] C. Allen, "Interferometric synthetic aperture radar," *IEEE Geosci. Remote Sensing Soc. Newslett.*, pp. 6-13, Sept. 1995.

[4] C. L. Martinez, X. Fabregas, and E. Pottier, "Wavelet transform-based interferometric SAR coherence estimator," *IEEE Signal Proc. Letters*, vol. 12, no. 12, pp. 831-834, Dec. 2005.

[5] C. L. Martinez and X. Fabregas, "Modelling and reduction of SAR interferometric phase noise in the wavelet domain," *IEEE Tans. Geosci. Remote Sens.*, vol. 40, no. 12, pp. 2553-2566, Dec. 2002.

[6] F. Martinerie, S. Ramongassie, B. Deligny, E. Thouvenot, and D. Massonnet, "Interferometric cartwheel payload: deveolpment status and current issues," *Proc. of IGARSS'01*, pp. 390-392, 2001.

[7] D. Massonnet, "Capabilities and limitations of the interferometric cartwheel," *IEEE Tans. Geosci. Remote Sens.*, vol. 39, no. 3, pp. 506-520, Mar. 2001.

[8] W. D. Wong, "Synthetic aperture radar interferometry with 2 satellites," Thesis for Master of Science, MIT, Jun. 2005.

[9] M. C. Yeung, B. Wu, and J. A. Kong, "Advances in interferometric synthetic aperture radar (InSAR)," Final Report to Mitsubishi Electric Corp., CETA at RLE, MIT, Feb. 2006.

[10] E. Rignot and J. V. Zyl, "Change detection techniques for ERS-1 SAR data," *IEEE Tans. Geosci. Remote Sens.*, vol. 31, no. 4, pp. 896-906, Jul. 1993.

[11] J. O. Hagberg, M. H. Ulander, and J. Askne, "Repeat-pass SAR interferometry over forested terrain," *IEEE Tans. Geosci. Remote Sens.*, vol. 33, no. 2, pp. 331-340, Mar. 1995.

[12] D. G. Corr and S. W. Whitehouse, "Automatic change detection in spaceborne SAR imagery," *AGARD Conference Proc.*, 582, Toulouse, France, pp. 39-1 to 39-7, Oct. 1996.

[13] D. G. Corr and A. F. Rodrigues, "Change detection using interferometric SAR data," *EUROPTO Conference on SAR Image Analysis, Modeliing, and Techniques II*, SPIE vol. 3869, Toulouse, France, pp. 127 to 138, Sep. 1999.

[14] H. Zebker and J. Villasenor, "Decorrelation in intererometric radar echoes," *IEEE Tans. Geosci. Remote Sens.*, vol. 30, no. 2, pp. 950-959, Sep. 1992.

[15] E. Rodriquez and J. M. Martin, "Theory and design of interferometric synthetic aperture radar," *IEE Proceedings-F*, vol. 139, no. 2, pp. 147-159, Apr. 1992.

[16] F. K. Li and R. M. Goldstein, "Studies of multibaseline spaceborne interferometric synthetic aperture radars," *IEEE Tans. Geosci. Remote Sens.*, vol. 28, no. 1, pp. 88-97, Jan. 1990.

[17] A. Ferretti, C. Prati, and F. Rocca, "Multibaseline InSAR DEM reconstruction: the wavelet approach," *IEEE Tans. Geosci. Remote Sens.*, vol. 37, no. 2, pp. 705-715, Mar. 1999.

[18] F. Ulaby, R. K. Moore, and A. K. Fung, *Microwave Remote Sensing–Active and Passive.* Norwood, MA: Artech, 1982.

[19] H. Braunisch, B. Wu, and J. A. Kong, "Phase unwrapping of SAR interferograms after wavelet denoising," *Proc. of IGARSS'00*, Honolulu, vol. 2, pp. 752-754, Jul. 2000.

[20] D. L. Donoho, "De-noising by soft-thresholding," *IEEE Trans. Inform. Theory*, vol. 41, pp. 613-627, May 1995.

[21] G. W. Davidson and R. Bamler, "Multiresolution phase unwrapping for SAR interferometry," *IEEE Tans. Geosci. Remote Sens.*, vol. 37, no. 1, pp. 163-174, Jan. 1999.

[22] A. Sowter, M. A. Warren, and R. M. Bingley, "The absolute positioning of spaceborne InSAR data using the integer ambiguity method," *The Photogrammetric Record*, vol. 21, no. 113, pp. 61-75, Mar. 2006.

[23] M. D. Pritt, "Congruence in least-squares phase unwrapping," *Proc. of IGARSS'97*, Singapore, 1997.

[24] D. C. Ghiglia and L. A. Romero, "Robust two-dimensional weighted and unweighted phase unwrapping that uses fast transforms and iterative methods," *J. Opt. Soc. Amer. A*, vol. 11, no. 1, pp. 107-117, 1994.

[25] D. C. Ghiglia and M. D. Pritt, *Two-dimensional pahse unwrapping: theory, algorithms and softwawre*, Wiley, New York, 1998.

[26] R. M. Goldstein, H. A. Zebker, and C. L. Werner, "Satellite radar interferometry: two-dimensional phase unwrapping," *Radio Sci.*, vol. 23, pp. 713-720, 1998.

[27] H. Lim, W. Xu, and X. Huang, "Two new practical methods for phase unwrapping," *Proc. of IGARSS'94*, Firenze, Italy, pp. 196-198, 1994.

[28] W. Xu and I. Cumming, "A region growing algorithm for InSAR phase unwrapping," *Proc. of IGARSS'96*, Lincoln, Nebraska, pp. 2044-2046, 1996.

[29] W. Xu and I. Cumming, "A region growing algorithm for InSAR phase unwrapping," *IEEE Tans. Geosci. Remote Sens.*, vol. 37, no. 1, pp. 124-134, Jan. 1999.

[30] H. A. Zebker and Y. Lu, "Phase unwrapping algorithms for radar interferometry: residue-cut, least squares, and synthesis algorithms," *J. Opt. Soc. Amer. A*, vol. 15, no. 3, pp. 586-598, Mar. 1998.

[31] M. D. Pritt, "Comparison of path-following and least-squares phase unwrapping algorithms," *Proc. of IGARSS'97*, Singapore, pp. 872-874, 1997.

[32] A. Hein, *Processing of SAR data: fundamentals, signal processing, interferometry*, Germany: Springer-Verlag Berlin Heidelberg, 2004.

[33] J. J. Akerson, "Phase unwrapping of synthetic aperture radar (SAR) interferometry," CETA at RLE, MIT, Mar. 1998.

[34] J. P. How, L. Breger, and G. Inalhan, "Coordination and control of the mitsubishi electric company spacecraft formation flying mission using convex optimization techniques," Report to Mitsubishi Electric Corp., Aero. Controls Lab., MIT, Aug. 2005.

[35] Orbital Equations, `http://liftoff.msfc.nasa.gov/academy/rocket_sci/orbmech/formulas.html`, NASA Liftoff to Space Exploration, accessed on Dec. 10 2006.

[36] K. I. Ranney and M. Soumekh, "Signal subspace change detection in averaged multilook SAR imagery," *IEEE Tans. Geosci. Remote Sens.*, vol. 44, no. 1, pp. 201-213, Jan. 2006.

[37] M. Preiss, D. A. Gray, and, Nick J. S. Stacy, "Detecting scene changes using sythetic aperture radar interferomery," *IEEE Tans. Geosci. Remote Sens.*, vol. 44, no. 8, pp. 2041-2054, Aug. 2006.

[38] P. Gamba, F. D. Acqua, and G. Lisini, "Change detection of multitemporal SAR data in urban areas combining feature-based and pixel-based techniques," *IEEE Tans. Geosci. Remote Sens.*, vol. 44, no. 10, pp. 2820-2827, Oct. 2006.

[39] D. G. Corr and A. F. Rodrigues, "Coherent change detection of vehicle movements," *Proc. of IGARSS'98*, Seattle, Washington, pp. 2451-2453, 1998.

[40] J. O. Hagberg, Lars M. H. Ulander, and, J. Askne, "Repeat-pass SAR interferometry over forested terrain," *IEEE Tans. Geosci. Remote Sens.*, vol. 33, no. 2, pp. 331-340, Mar. 1995.

[41] Timothy M. Payne, "The effect of scene elevation on the coherence of wide-angle crossing-node SAR pairs," *IEEE Tans. Geosci. Remote Sens.*, vol. 40, no. 12, pp. 2553-2566, Dec. 2002.

[42] S. Mallet, *A Wavelet Tour of Signal Processing*, 2nd ed., San Diego, CA: Academic, 1998.

[43] A. Cohen and J. Kovacevic Jr., "Wavelets: The mathematical background," *Proc. IEEE*, vol. 84, pp. 514-522, Apr. 1996.

[44] N. Hess-Nielsen and M. V. Wickerhauser, "Wavelets and time frequency analysis," *Proc. IEEE*, vol. 84, pp. 523-540, Apr. 1996.

[45] D. Massonnet and C. Elachi, "High-resolution land topography," *C. R. Geoscience*, 338, Jul. 2006.

[46] J. A. Kong, *Electromagnetic Wave Theory*, EMW Publishing, Cambridge, MA, 2005.

[47] B. R. Mahafza, *Radar Systems Analysis and Design Using MATLAB®*, 2nd ed., Chapman & Hall/CRC, Taylor & Francis Group, 2005.

[48] I. G. Cumming and F. H. Wong, *Digital Processing of Synthetic Aperture Radar, Algorithms and Implementation*, Artech House, 2005.